3D Probe for Magnetic Imaging and Non-destructive Testing

Fawaz Hadadeh

université PARIS-SACLAY

NNT : 2018SACLS421

Thèse de doctorat

3D probes based on magnetoresistive sensors for magnetic micro-imaging and NDT

Thèse de doctorat de l'Université Paris-Saclay préparée au Service de Physique de l'Etat Condensé, et au Département imagerie simulation pour le contrôle, CEA

École doctorale n°564 Physique de l'Ile de France
Spécialité de doctorat : Physique

Thèse présentée et soutenue à Gif-sur-Yvette, le 14 Novembre 2018, par

Fawaz HADADEH

Composition du Jury :

M. Philippe Lecoeur, Laboratoire C2N, Marcoussis	Président
Mme Claire Baraduc CEA-Spintec, Grenoble	Rapporteur
M. Jerome Gattacceca, Technopole Environnement Arbois-Méditerranée, Aix en PROVENCE	Rapporteur
M. Hervé Tretout Dassault Aviation, Argenteuil	Examinateur
M. Nicolas Poulakis Technological Educational Institution of West Macedonia	Examinateur
M.Claude Fermon CEA-SPEC, Gif-sur-yvette	Directeur de thèse
Natalia Sergeeva-Chollet CEA- LIST, Gif-sur-yvette	Encadrante

Table of Contents

I. Related Publications

1. ***Article:***

- F. Hadadeh, A.Solignac, N. Sergeeva-Chollet, M. Pannetier-Lecoeur et C. Fermon "3D magnetic imaging with GMR sensors". (submitted).

2. ***Conferences:***

- F. Hadadeh, N. Sergeeva-Chollet, E. Paul, M.Pannetier-Lecoeur et C. Fermon " GMR probes for Magnetic Micro-Imaging and Non-Destructive Evaluation ", **Joint European Magnetic Symposium**, August 2016, Scottish Exhibition and Conference Centre (SECC), Glasgow, UK
- F. Hadadeh, N. Sergeeva-Chollet, E. Paul, M. Pannetier-Lecoeur et C. Fermon "Développement de la sonde CF à base des capteurs GMR, pour la détection des trois composantes du champ", **COFREND**, Mai 2017, Strasbourg France
- F. Hadadeh, N. Sergeeva-Chollet, E. Paul, M. Pannetier-Lecoeur et C. Fermon "Probe based on magnetoresistive Sensors for magnetic micro-imaging and NDT", **Workshop on Electromagnetic Non Destructive Evaluation**, Septembre 2017, Saclay France
- F. Hadadeh, N. Sergeeva-Chollet, E. Paul, M. Pannetier-Lecoeur et C. Fermon "La détection des trois composantes du champ par une sonde CF à base des capteurs GMR", **Colloque Louis Néel**, Septembre 2017, Paris France
- F. Hadadeh, B. Esteves, N. Sergeeva-Chollet, A. Skarlatos, A. Solignac, M. Pannetier-Lecoeur et C. Fermon "Local magnetic microscopy of ferromagnetic steels based on magnetoresistive sensors", 12th **European Magnetic Sensors and Actuator**, July 2018, Athens Greece

3. ***Patent***

- A. Solignac, N. Sergeeva-Chollet, F. Hadadeh, M. Pannetier-Lecoeur, C. Fermon "Dispositif et methode de cartographie de la susceptibilité magnétique de surface de matériaux. " (In preparation)

II. List of Figures

III. List of abbreviations

ACFM	Alternating current field measurement
AMR	Anisotropic magnetoresistance
AFM	Atomic Force Microscopy
GMI	Giant magnetoimpedance
GMR	Giant magnetoresistance
EC NDT	Eddy current non-destructive testing
ECT	Eddy current testing
EC	Eddy current
FM	Ferromagnetic materials
HNDT	Holographic nondestructive testing
LPF	Low-pass filter
MI	Magneto Impedance
MPI	Magnetic particle inspection
MFM	Magnetic Force Microscopy
MO	Magneto-optical
MR	Magnetoresistance
NDT	Non-destructive testing
NM	Non-magnetic
NMR	Nuclear Magnetic Resonance
PT	Penetrant Testing
PEC NDT	Pulsed eddy current non-destructive testing
RTN	Random telegraph noise
SQUID	Superconducting Quantum Interference Device
SMRM	Scanning magnetoresistance microscope
SNOM	Scanning Near-Field Optical Microscope
SNR	Signal-to-noise ratio
STM	Scanning Tunneling Microscope
TEM	Transmission Electron Microscope
TMR	Tunnel MagnetoResistance

UT	Ultrasonic testing

IV. Introduction

The work presented in this thesis focuses on the design of probe allowing simultaneously reconstruction of three components of magnetic field at the same measurement point (3D probe), for non-destructive testing (NDT) and magnetic imaging applications.

NDT is used in order to evaluate the properties of a wide variety of materials without causing damage. Some of the common non-destructive techniques are eddy current, ultrasonic, optics, radiography and liquid penetrant testing. In NDT applications, the eddy current technique (ECT) is a widely technique used to detect and identify surface and sub-surface defects in conductive materials such as aluminum, inconel or steel. The principle of the eddy current technique is based on the interaction between magnetic field emitter to induce eddy currents in a controlled piece and sensors to detect the magnetic field created by these eddy currents. The sensors can detect the presence of defects in the controlled piece by monitoring changes in the emitted field.

Magnetic imaging consists on measuring the magnetic stray field emitted by a magnetic object. At micron scales, it allows to reconstruct the magnetic inhomogeneitites of the object, which can be related to structural shape, material inhomogeneities or domain formation. Magnetic imaging is also used to determine current flows on a material surface. DC measurement gives the static configuration while AC measurement allows the determination of either AC current flow, either local susceptibilities. Above a large use in condensed matter physics, magnetic imaging is used in microelectronics for circuit failure determination, in magnetic industry (storage and magnetic sensors) and in geophysics to determine properties of rocks for example.

The probes developed in my PhD work are based on spin electronics sensors, which are based on the use of the spin of electrons in conductive layer to manipulate their transport properties. The giant magnetoresistance effect (GMR) discovered in 1988 allowed the fabrication of high sensitivity and micron size magnetic sensors. The resistance of the GMR changes with the application of external magnetic field. GMR with spin valves shape are a particular case of multilayered structure where the resistance is varying as the angle of the applied external field and an internal reference direction. GMR sensors have been first implemented in read heads for hard disk drives and more recently in a wide variety of products for automotive, energy

monitoring or health applications. For NDT applications, GMR sensors overcome the limits related to the fabrication of very small coils, while bringing a very good detectivity. The size of GMRs allows also the realization of 3D probes.

Achievement of the Work

The main achievements of the research work can be summarized as follows:

- ✓ Literature survey that brought understanding and familiarity with magnetic sensors, NDT techniques, and different types of microscopes for magnetic imaging.
- ✓ Design and construction of 3D probes based on four GMR sensors allowing simultaneously reconstruction of three components of magnetic field at the same measurement point, which includes hardware (mechanical support, electronic circuit, emitter part for NDT application…) and software (code to reconstruct the three components of magnetic field by the signals received from the four GMR sensors, noise elimination…).
- ✓ Different types of GMR sensors have been developed for different types of applications compromising detectivity and magnetic field range. Magnetic imaging of model systems: current line, one-dollar bill, structured metallic object.
- ✓ Implementation of a magnetic imaging of susceptibility.
- ✓ Probe configuration and emitter dimensions for NDT have been optimized by simulations in CIVA software.
- ✓ Detection of µm-sized and mm-sized defects in Aluminum, Inconel and Titanium samples and the reconstruction of three magnetic components have been achieved.

Thesis Layout

Chapter 1 presents a non-exhaustive bibliographic collection of magnetic sensors, usable for magnetic imaging and for NDT. This chapter highlights a summary of the main properties of magnetic sensors, and details principle of the GMR (chosen for the development of the 3D probe).

Chapter 2 reports a state of the art of different NDT methods : their application and their performance. Review on the use of Eddy current testing and the key features of this method for surface and sub-surface flaws inspection are also reported.

Chapter 3 describes non-exhaustive state of the art concerning microscopes using for magnetic imaging. We will look at the advantages of the 3D probe based on GMR sensors for micro-imaging application and compare them to other magnetic imaging microscopes.

Chapter 4 reports the design of the new 3D probe based on GMR sensors, which is comprised of electronics and hardware. Two kinds of GMR used for the developing of the 3D probe have been described: The type 1 GMR sensor has sensitivity of 19 V/V/T and has a maximal working field up to ±15 Oe. The second type of GMR sensor has a larger working field (±200 Oe) than the type one sensor at the detriment of its sensitivity (3.5 V/V/T.) The characteristics of these GMR sensors (stack, sensitivity, noise measurement and detectivity) are also discussed.

Chapter 5 introduces the experiments on the performance of the 3D probe for magnetic imaging. Detection of three components of the field generated by a current line and one-dollar bill are presented. Magnetic imaging of magnetic objects with arbitrary shapes in soft steel object are discussed. Also we will show the performance of 3D probes for spacing between close magnetic features and for susceptibility measurement.

Chapter 6 introduces the experiments on the performance of the 3D probe for NDT. Probe configuration and emitter dimensions optimized by simulations have been discussed. Detection of three components of magnetic field response caused by sub-surface and surface defects (μm-sized) in Aluminum, Inconel and Titanium mock-ups are presented. Comparison of the experimental results and simulation results are also presented.

Conclusions drawn from the research work and sets out recommendations for further work are given at the end.

Part 1: Literature Review

Chapter 1. Magnetic sensors

1.1 Introduction

The sensor in general is a device that transforms a physical quantity into a usable quantity like current or voltage. Magnetic sensors described in this chapter are measuring a magnetic field or a magnetic flux and produce a voltage output proportional to that measured quantity. There are different types of magnetic sensors, like inductive magnetic sensors (coils) [1], fluxgates [2], Hall devices [3], Giant Magnetoimpedance (GMI) [4], anisotropic magnetoresistance (AMR) [5], giant magnetoresistance (GMR) [6], tunnel magnetoresistance (TMR) [7], each one useful for specific applications. This chapter presents first a non-exhaustive bibliographic collection of these magnetic sensors, usable for magnetic imaging and for non-destructive testing. There are other magnetic sensors with good performances in terms of minimum detectable field and spatial resolution, such as SQUID (Superconducting Quantum Interference Device) sensors [8] not presented here due to their conditions of use with cryogenic cooling and their expensive cost which make them difficult to operate in Non-destructive testing context. We will detail GMR sensors and their characteristics more than the other sensors, because they are the base of developed probes.

1.2 Magnetic sensors

A magnetic sensor is in general a part of measurement chain that transforms the magnetic field detected into a usable quantity typically a voltage (Figure 1.1) [9]. The main interest of the magnetic field is to freely propagate in space which allows non-contact detection. For that reason, magnetic sensors are used in a wide range of applications like distance, speed, current measurements, metal characterization or non-destructive testing (NDT).

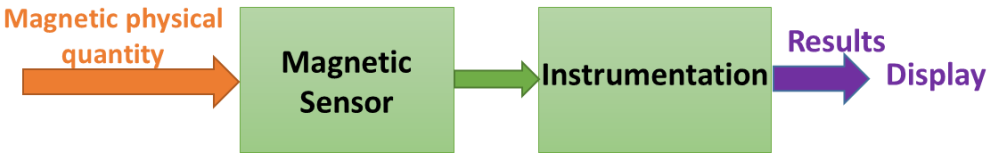

Figure 1.1- Measurement diagram of magnetic field

1.3 Sensitivity, detectivity and noise.

Here, we introduce some definitions extensively used in the document.

1.3.1 Sensitivity

The first one is sensitivity. Sensitivity is the output voltage obtained for a given field applied on a sensor. That sensitivity is given in Volt(V)/Tesla(T) but depending of the sensor technology other quantities can be used.

For example, magnetoresistances or Hall effect sensors where a resistance is varying with the field, the output voltage is proportional to the bias voltage applied to the sensor. Then the sensitivity is given in V/V/T.

As we will see later, inductive sensors have a sensitivity, given in V/T and it depends on the frequency. Hence, sensitivity will be given at a specific frequency.

1.3.2 Noise.

The noise of sensors is as important as the sensitivity as performances will be given by the signal to noise available. Noise is nearly always given in $V/\sqrt{Hz}$ at a given frequency. Sources of noise will be described later.

1.3.3 Detectivity.

The detectivity or field equivalent noise is the most suitable quantity to compare different magnetic sensors. It is the field for which the signal to noise ratio is one. Hence, it is equal to the noise in $V/\sqrt{Hz}$ divided by the sensitivity. It is given in $T/\sqrt{Hz}$. Detectivity is usually dependent on the frequency but also on the voltage biasing, size etc... of each sensor.

1.4 Noise in magnetic sensors

The noise of magnetic sensors can be classified into two categories: white noise independent of frequency (thermal noise and shot noise), and noise dependent of the frequency such as: 1/f noise or random telegraphic noise (RTN). Also electronic and instrumental noises influence on the level of magnetic sensors detection. The entire measurement chain (including amplification and electronics circuit), gives noise signal at their output, which limits the level value of useful signal measured. We introduce noise directly related to magnetic sensors described in this chapter.

White noise

The first form of white noise is the thermal noise or Nyquist noise. Any resistance in non-zero temperature is a source of electrical noise. The velocity of electrons is zero in the absence of electromotive force. However, the resistance fluctuations is non-zero due to Brownian motion. At a fixed temperature T, the voltage spectral density of thermal noise $S_{V,th}^{1/2}$ is given by the Nyquist formula (equation (1-1)), where k_B is Boltzmann constant, R is the magnetic sensor resistance, and T is the temperature [10]:

$$S_{V,th}^{1/2} = \sqrt{4.k_B.T.R.} \tag{1-1}$$

The second form of white noise is the shot noise. It is an electric noise that can be modeled by Poisson law. Shot noise reflects the discreet nature of carriers charge (fluctuation of some number of carriers). Under the action of electric field, an electric current is generated by the individual transport of charge carriers. This noise, unlike the thermal noise, is directly related to electric current I and to the charge of carriers. Its spectral noise density $S_{V,Shot}^{1/2}$ is given in Volt, and can be calculated by the following equation:

$$S_{V,Shot}^{1/2} = \sqrt{2.e.\bar{I}.R} \tag{1-2}$$

where e is the charge of the electron and the coefficient 2 is coming from the fact that we reason only in positive frequencies. This noise is present only in tunnel junctions, and thus in TMR magnetic sensors which will be described later in this chapter.

1/f noise

The origin of 1/f noise is still a subject of discussion. This noise appears at low frequencies and decreases roughly as 1/f. 1/f noise is observed in nearly all existing phenomena ranging from earth quakes to brain activity but also in a simple resistance wire. In metallic conductors this noise is related to a resistance noise and hence it is revealed when a current is sent through the conductor. For that reason, it is particularly important for magnetoresistances where the resistance is varying with magnetic field Thus the 1/f noise could have an electrical and/or a magnetic origin in GMR sensors.

The spectral density of 1/f noise observed in various components is inversely proportional to frequency ($1/\mathrm{f}^{\gamma}$) with γ is about one. In 1969, F. N. Hooge proposed phenomenological relationship through the collection of large number of experimental results on semiconductors and homogeneous metals [11]:

$$S_{V,1/f}(f) = \frac{\alpha_H}{N_c}.\frac{V^2}{f^{\gamma}} \tag{1-3}$$

where V is a potential difference that across the conductor, N_c is the total number of charge carriers in the material. The Hooge constant α_H is non-dimensional parameter that depends on the purity and on the number of defects present in the material [12]. The Hooge constant α_H/N_c allows comparison of noise level between sensors. The 1/f noise dominates the white noise (typically in GMR and TMR) below cut-off or overlap frequency f_c. The noise due to magnetic domain is very high in small magnetic GMR sensors and is strongly related to structural properties and magnetic configuration of the GMR. As this noise is inversely proportional to the number of carriers, to increase the volume of the sensor reduces the 1/f noise. This can be done by lengthening the yoke (will be presented in paragraph 4.5) or connecting several GMR in series or in parallel.

Random Telegraphic Noise (RTN):

Random telegraph noise (RTN) is one of important dynamic variation sources in digital circuits. RTN occurs due to the random trapping/detrapping fluctuations, it is important to study the RTN, since it is often due to random fluctuations between the metastable states of the magnetic domains of the free layer. This phenomenon inducing undesirable variations in resistance is strongly dependent on working

conditions of the device, and on polarization current. The spectral density of RTN is given in Eq 1-5

$$S_{V,RTN}(f) = \frac{S_{V,RTN}(0)}{\cosh(\frac{\Delta E}{k_B T})\left[cosh^2\left(\frac{\Delta E}{k_B T}\right) + (2\pi f\tau)^2\right]} \quad (1\text{-}4)$$

Where $\tau^{-1} = \sum_{i=1}^{2} {\tau_i}^{-1}$ with $\tau_i = \tau_{i,0} \exp\left(\frac{E_i}{k_B T}\right)$, E_i corresponds to energy level of state 'i'.

In magnetoresistive sensors like GMR and TMRs, RTN noise is mainly due to magnetic domain fluctuations. It has been demonstrated that by a shape of the sensor or by magnetic stabilization of the magnetic layers, it can be reduced or even eliminated [13].

Example:

In Figure 1.2 results obtained by Trauchessec et al. [14] on a GMR sensor are shown. The square root of the noise power spectral density (right part) exhibits two components: thermal noise and the low-frequency noise; the thermal noise becomes dominant above 1 kHz. The detectivity in the thermal noise regime of this sensor is 0.1 $nT/\sqrt{Hz}$.

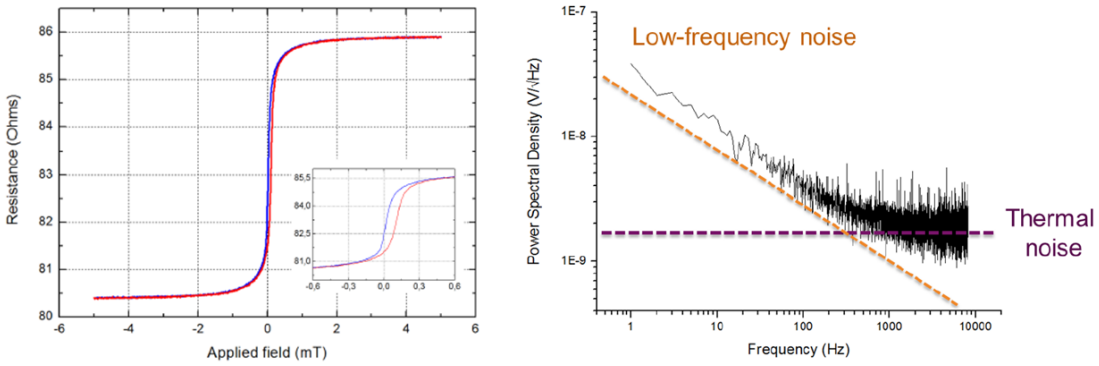

*Figure 1.2-GMR characteristics as a function of the magnetic induction **(left part)**, noise in a yoke-type GMR **(right part)** of 5µm width*

1.5 Inductive magnetic sensors

Inductive sensors are one of the oldest and most well-known type of magnetic sensors [15]. Inductive sensors are coils with different geometries, flat or solenoid. Generally, conventional coils are fabricated by winding a copper wire around a core.

Thanks to Lenz-Faraday induction phenomenon (Equation (1-5)), the magnetic field variation into the inductive sensor creates a voltage. The transfer function of induced voltage measured across the coil is given by V = f (B). This transfer function results from the fundamental Faraday's law of induction:

$$V = -n.\frac{d\Phi}{dt} = -n.A.\frac{dB}{dt} = -\mu_0.n.A.\frac{dH}{dt} \quad (1\text{-}5)$$

where Φ is magnetic flux passing through a coil with an area A and a number of turns n. The output signal of a coil, *V*, depends on the rate of change of flux density dB/dt. The sensitivity S of the coil is the ratio of amplitude V to the magnetic field B, according to the Lenz-Faraday law, at the frequency f. It could be written as:

$$S = \left|\frac{V}{B}\right| = n.2.\pi.f.A \quad (1\text{-}6)$$

This equation shows that the sensitivity of inductive magnetic sensor increases when frequency, dimensions or number of turns increases. However, the sensitivity is limited by the resonance frequency f_0 (equation (1-7)). If the working frequency f is higher than the resonance frequency of the inductive sensor ($f > f_0$), the sensitivity starts to decrease. The equivalent circuit of inductive magnetic sensor is described in Figure 1.3.

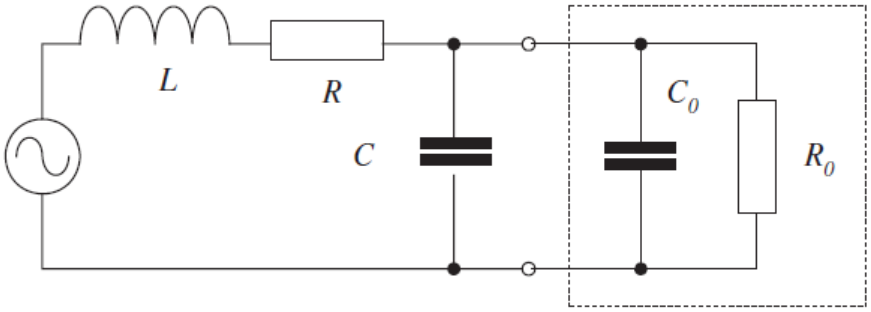

Figure 1.3-Equivalent circuit of induction sensor with load capacity C_0 and load resistance R_0.

This resonance frequency depends on the internal resistance *R*, inductance *L* and self-capacitance *C* of coil sensor:

$$f_0 = \frac{1}{2.\pi.\sqrt{L.C}} \quad (1\text{-}7)$$

At frequency above the resonance frequency, the operation of inductive magnetic sensor is dominated by the parasitic capacitance, and it becomes equivalent to a capacitor. Thus, the inductive magnetic sensor will become unusable for NDT and magnetic imaging applications. Above the resonance frequency, with $\alpha = R/R_0, \beta = R.\sqrt{C/L}, and\ \gamma = f/f_0 = 2.\pi.f.\sqrt{L.C}$ the sensitivity of inductive coil can be also expressed by the following expression [16]:

$$S = \frac{n.2.\pi.A}{\sqrt{(1+\alpha)^2 + \left(\beta^2 + \frac{\alpha^2}{\beta^2} - 2\right) \times \gamma^2 + \gamma^4}} \tag{1-8}$$

The inductive sensors could contain a ferromagnetic core in order to concentrate the magnetic field and to increase the sensitivity [17].

According to equation (1-6) the sensitivity can be increased by increasing the coil surface, but the counter part for NDT is the decrease of the spatial resolution. The minimum magnetic field detectable by the coil is also limited by the intrinsic noise of coil and by the noise of associated electronics. In addition, the intrinsic thermal noise of the coil increases with its resistance, thus, the intrinsic thermal noise increases with its dimensions and number of turns.

The performance of inductive sensors can be calculated analytically in case of coils without ferrite core. Korepanov details it in [18].

Here we will take two examples, which will allow us to compare GMR/TMR sensors and inductive coils performances for non-destructive evaluation.

The first example is a square coil that has the following characteristics: resistance of 3.5 Ohms, 8 layers, each layer has 9 mm^2 of effective surface, and one turn (Figure 1.4).

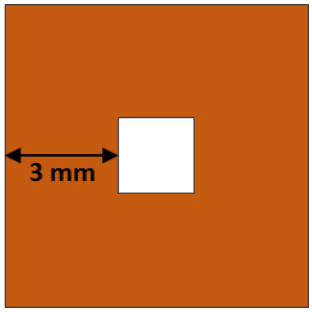

Figure 1.4-Square Coil

According to the Nyquist formula, its spectral density of white noise $S_{V,th}^{1/2}$ is 0.24 $nV/\sqrt{Hz}$. Equation (1-6) allows to calculate a sensitivity S of 5.4 V/T at 12 kHz. Its detectivity is equal to $S_{V,th}^{1/2}/S = 44\ pT/\sqrt{Hz}$ at 12 kHz, if the noise is limited by the coil. If we consider a preamplifier with a typical voltage noise of 1 $nV/\sqrt{Hz}$ this gives a detectivity of 176 $pT/\sqrt{Hz}$.

The second example is a micro coil that wound using 0.7 mm radius wire, 460 turns and has a resistance of 32 Ohms.

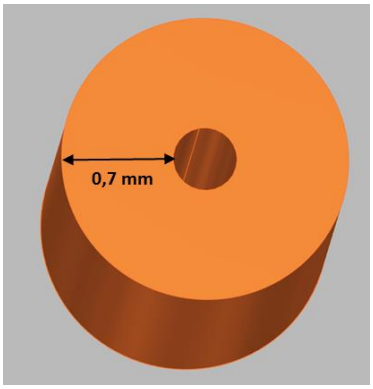

Figure 1.5- Cylindrical Coil

The cylindrical coil has white noise spectral density $S_{V,th}^{1/2}$ of 0.73 $nV/\sqrt{Hz}$. Equation (1-6) allows to calculate its sensitivity S = 53 V/T at f = 12 kHz. Its magnetic noise is equal to 13 $pT/\sqrt{Hz}$ at f= 12 kHz. Mook presents in [19] the limit of miniaturized coil dimension using a copper wire of 30 µm diameter: it has a width of 0.5 mm, length of 3 mm, 1000 turns.

Another type of coils is etched coils made on standard PCB or on flexible film of Kapton type. Kapton is a thin film of polyimide, from ten to several hundreds of micrometers, which has a very good flexibility. These flexible sensors allow to inspect complex shapes objects. For example, an eddy current probe for NDT developed in our laboratory is composed of 96 patterns of 2 micro-coils etched on a soft Kapton film of 50 µm of thickness Woytasik presents in [20] an example of coils that have 13 turns in a volume of 30x18x100 μm^3. The micro-coils allow to innovate in biomedical instrumentation such as Nuclear Magnetic Resonance (NMR) using for imaging or for spectroscopy [21, 22]. Khelifa describes in [23] the manufacturing processes of

flexible rectangular micro-coil ($500 \times 1000\ \mu m^2$) made on kapton substrate for NMR. Micro-coils have a limited spatial resolution and a limited sensitivity at low frequencies but are very efficient at high frequencies.

1.6 Fluxgates

Fluxgates sensors are composed of a ferromagnetic core and at least two coils. There are several configurations of fluxgate sensor, which are described in [24, 25]. Figure 1.6 shows one of these configurations: an exciter winding surrounding the nucleus, traversed by alternative current, creates an alternating magnetic field in the core, locally parallel to the winding axis. The corresponding induction undergoes saturation, symmetrical to zero. Another winding is arranged around the core, its axis being rectilinear. The first coil is called the excitation coil, while the second one is called the measurement coil or pick-up coil. These sensors exploit the saturation of ferromagnetic material of core.

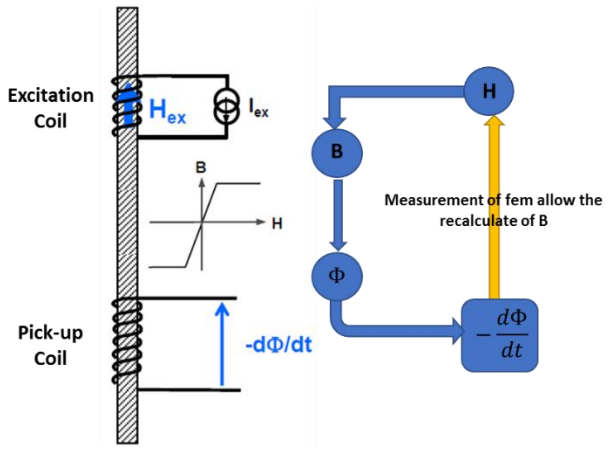

Figure 1.6-Principle diagram of fluxgate

The voltage at the output of the pick-up coil has a form of pulses. In the absence of external magnetic field, the voltage is symmetric in time. In presence of external magnetic field, the saturation of core is more rapid for one semi-period than another. This asymmetry induces a time shift in the voltage at the output of pick-up coil. The measurement of this time shift allows to estimate the value of the external magnetic field. Figure 1.7 shows the principle of phase shift measurement at the output of pick-up coil using to detect the presence of external magnetic field. We deduce external magnetic field H_{ex} by the measurement of interval between the pulses.

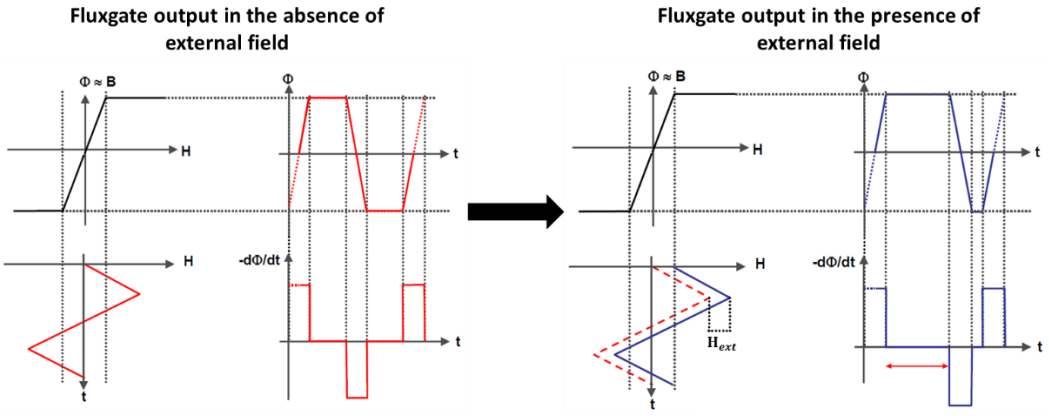

Figure 1.7- Principle of pulse shift method

The excitation coil frequency for fluxgate is in general between 50 Hz and 10 kHz. Fluxgates have a high sensitivity, especially for continuous magnetic fields. They are developed initially for compasses, because they are able to detect the Earth's magnetic field. They are able to measure the components of constant or varying magnetic field vector in the range from 0.1 mT to 8 mT at frequencies up to several kHz. Pavel Ripka describes in [26] a summary of fluxgates performances. Recently, printed circuit board (PCB) technology has been used in the development of planar fluxgates for NDT application [25]. Kejík has developed a 2D planar fluxgate composed of two orthogonal plan coils and an amorphous ferromagnetic core in the shape of PCB ring [27]. The authors report that the sensor is linear in a range of ±60 µT, and shows a sensitivity of 55 V/mT. Also in biology application, a fluxgate sensors have been used in order to determine the binding between Streptavidin proteins with Biotin [28] and to study the release properties of hydrogel cylinders and microsphere [29].

Reducing of fluxgate dimensions decreases its performance. To prove this, we consider two following examples: first, a sensor made by the Bartington Instrument Company with a volume of 8 × 8 × 30 mm^3 has white noise about 2 $pT/\sqrt{Hz}$ and can work up to 4 kHz; second, a micro-fluxgate designed by CEA LETI in 2005 with dimensions 1mm × 400µm × few µm etched on Silicon has white noise about 1 $nT/\sqrt{Hz}$ [30, 31]. By simple comparison between the thermal noise of these two examples, we can conclude that the reducing of fluxgate dimensions undergoes a loss in fluxgate performances manifested by increasing of noise. The main problem of miniaturized fluxgates stems from the volume of their coils. The fluxgates show

important restrictions due to their weight, power consumption and high temperature fluctuations (no thermal stability).

1.7 Giant magneto-impedances

Magneto Impedance (MI) has been discovered in 1930 by Harisson et al in a nickel wire [32]. Later, in the early 1990s, Panina et al. studied the phenomenon in amorphous wires and films, and discovered Giant Magneto-Impedance (GMI) [33]. Giant magneto-impedance (GMI) is due to a significant modification of the impedance of soft ferromagnetic materials (amorphous or nanocrystalline wires or ribbons) when they are subjected to external magnetic field. The excitation frequency of GMI is in the MHz range.

Figure 1.8 shows GMI sensor configuration formed by a simple ferromagnetic wire crossed by an alternating current:

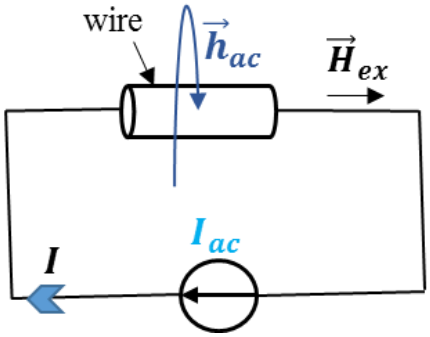

Figure 1.8- GMI sensor made of ferromagnetic wire crossed by alternating current and subjected to an external field H_{ex}

The impedance of conducting wire depends on skin effect δ (equation (2-7)), to geometrical dimensions of the wire a, and to the wire resistance at low frequency R. j is the complex number according to the relation:

$$Z = (1 + j) \, . R . \frac{a}{\delta} \tag{1-9}$$

The impedance given here is only defined if there is linear relation between current and voltage. This relation is valid if δ<<a. However, ferromagnetic material is non-linear. The impedance Z is therefore valid only around the operating point [34, 35]. δ depends on permeability μ, so the GMI impedance depends on permeability μ. However, in ferromagnetic materials, the permeability μ depends on external magnetic

field H_{ext}. Thus, when an external field H_{ex} is applied, the permeability is changed and this change produces an impedance variation.

GMI has relative impedance variations greater than 600% and relative impedance variation of 1440 % / mT [36]. GMI sensors fabricated by AICHI Micro Intelligent company [37] are unitary assemblies that are composed of amorphous wire of 20 μm at diameter. These sensors are marketed with amplification electronics with total dimensions of 31 × 11 mm^2 (Figure 1.9), and have linearity range of 0.6 mT. Tannous et al. summarized the different physical parameters that maximize the GMI impedance variation [38].

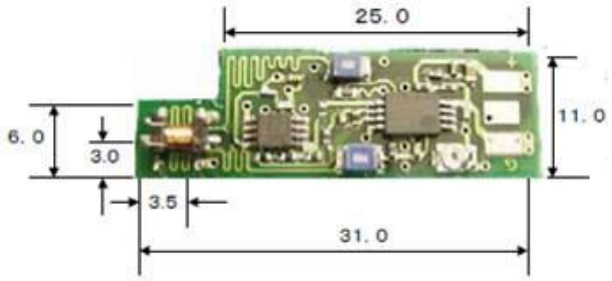

Figure 1.9- GMI sensor marketed by AICHI Company [37]

Boukhenoufa and Dolabdjian have developed a GMI with a length of 10 mm and white noise of 100 $pT/sqrt(Hz)$ at 10Hz [39]. This noise range allows GMI sensor to compete with fluxgates. Traore has fabricated a GMI sensor that has 400 turns of external coil, 2.5 mm of length, and 20 μm of diameter [40]. This GMI sensor has a white noise about 1.8 $pT/\sqrt{Hz}$ at 1 Hz.

Large impedance variations allow to GMI sensors to detect very weak magnetic fields. GMI sensors have been evaluated by Vacher [41] and by Peng [42] for detection of small magnetic fields for non-destructive testing application. These sensors show good performance in detection of buried defects [43]. However, excitation circuit of GMI sensors should operate at high frequencies (more than 20MHz) that makes difficult their integration into probes for non-destructive testing. Because of their high sensitivity at low frequencies, GMI sensors are used for development of magnetic biosensors. Magnetic biosensors based on GMI sensors are used for detection of magnetic field variation caused by magnetic microparticles [44]. Chen and al. use GMI sensors to identify gastric cancer cells [45].

The weak point of GMI sensor compared to fluxgate is the remanent field effect after subjecting to strong magnetic fields, because the ferromagnetic core is usually not demagnetized during sensor operation [26]. Despite the high sensitivity of GMI sensors, it is shown that the performance of these sensors is limited by the noise level of electronics, especially in the white noise zone by comparing with GMR and TMR sensors.

1.8 Hall Effect Sensor

The Hall effect is part of a set of phenomena called galvanometric effect. The galvanometric effects are observed in solid which undergoes simultaneously the action of electric field and magnetic induction. Hall effect occurs when a material crossed by electric current I, is subjected to magnetic induction field B perpendicular to the current direction (Figure 1.10).

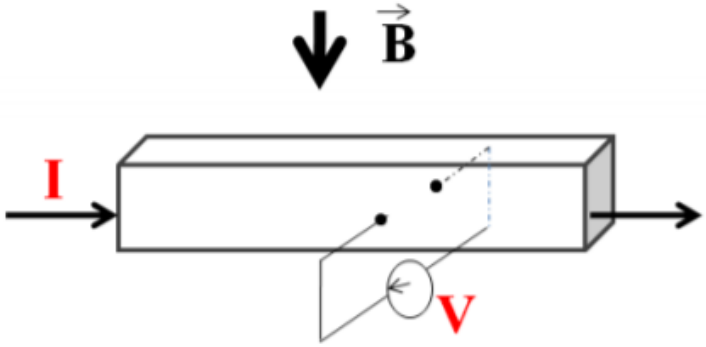

Figure 1.10- Principle of Hall effect

In the presence of magnetic field, the charge carriers undergo the Lorentz force and are deflected during the transient regime. The appearance of surface charges at the top and at the base of the sample creates an electric field and generates a force, opposite to Lorentz force. The potential difference, called Hall voltage V appears between the faces of the sample. It is proportional to the injected current and to the magnetic field. The sensitivity of Hall effect sensor can be increased [46] by ferromagnetic concentrators. It increases from 10 mV / T to 1.4 V / T. The highest reported detectivity limit of a combination of Hall sensor with magnetic concentrators is as low as 10 pT [47]. Hall-effect sensors offer an advantage over a coil for depth penetration structure that requires working at low frequencies and for spatial resolution. They are cheap and easy to integrate. They are particularly interesting in terms of linearity and

they offer a wide range of magnetic field measurement (since there is no saturation). Kejik describes in [48] an integrated micro-Hall plate sensor with an active area of 2.4 ×2.4 μm^2 supplied by the spinning current and has a white noise of 300 $nT/\sqrt{Hz}$.

The Hall effect sensor has been employed for applications of non-contact switching, memory readout and current measurements. Ejsing has used this sensor for the detection of magnetic induction generated by magnetic nanoparticles [49]. Also, Oota has used a scanning Hall-sensor microscope with an active area 25×25 μm^2 for non-destructive testing of structural materials [50]. Lee has used these sensors with 0.52 mm spatial resolution for NDT and crack evaluation of ferromagnetic materials [51] .

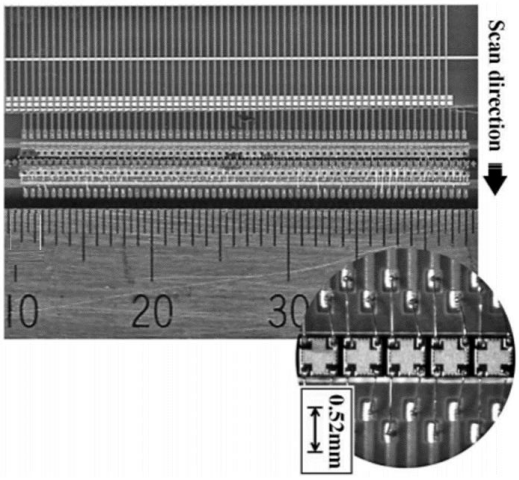

Figure 1.11- Photograph of the linearly integrated Hall sensors (LIHaS): 64 InSb Hall sensors [51] .

1.9 Magnetoresistive sensors

Magnetoresistance effect (MR) has been discovered by William Thomson in 1856 [52]. Under the effect of external magnetic field (H_{ex}), the resistance of MR sensors will be changed to a new resistance value (R). This magnetoresistance effect (MR ratio) is a performance index that can be defined. The MR sensors will have a minimum resistance (R_{min}) and a maximum resistance (R_{max}). The magnitude of the magnetoresistance effect (MR) can defined as follows with ($R_0 = R_{mean}$ in the case of AMR and GMR, and $R_0 = R_{min}$ in the case of TMR):

$$MR = \frac{\Delta R}{R_0} = \frac{R_{max} - R_0}{R_0} \quad (1\text{-}10)$$

There are different types of magnetic sensors like Anisotropic Magneto-Resistive (AMR), Giant Magneto-Resistive (GMR) and Tunnel Magneto-Resistive (TMR) sensors. At the beginning, the AMR sensors has been developed to replace coils in hard disks read heads, with the aim of reducing the bit size on the writing media. After the development of GMR, AMR sensors have been replaced by GMR sensors, and now GMR sensors are partly replaced by TMRs. Magnetoresistive sensors have many other applications, such as current measurement, velocity measurement, non-destructive testing and magnetic imaging.

1.9.1 Anisotropic Magnetoresistance (AMR)

Anisotropic magnetoresistance (AMR) is a generic magnetotransport property of ferromagnetic metals materials (and their alloys). The anisotropic magnetoresistance effect, occurs when the electrical resistivity depends on the relative angle θ between the direction of electrical current (direction of easy axis) and orientation of the magnetic field [53] (Figure 1.12). When the external magnetic field is parallel to AMR easy axis, the resistance R of AMR does not vary, and is still equal to (R_0). The AMR effect reaches its maximum when θ equal to 90° angle.

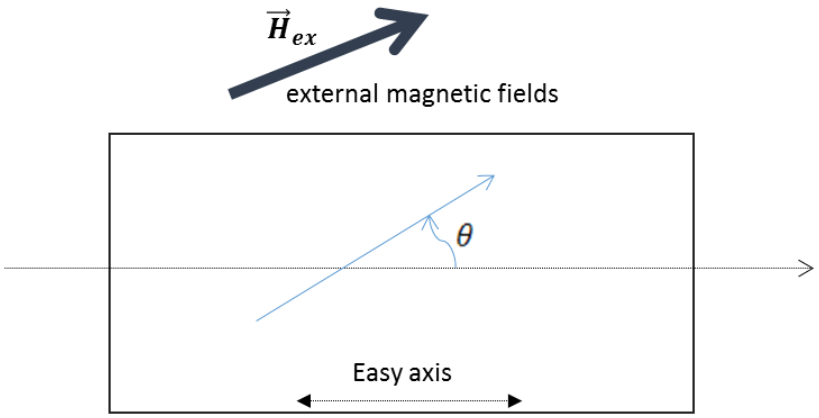

Figure 1.12-Principe diagram of AMR sensor

The resistance R varies as $\cos^2(\theta)$ [54].

$$R = R_0 + \Delta R.\cos^2(\theta) \quad (1\text{-}11)$$

AMR sensors are more sensitive than Hall sensors. The AMR ratio ranging between 1% and 5 % for permalloy at room temperature [55].This effect can be used to measure the components of magnetic field vector in the range of 1 nT to 1 mT. Sensitec Company developed an AMR Fix Pitch sensors for angle and length measurement with accuracy of 3 to 25 µm [56]. It is difficult to achieve pT noise values, Zimmermann has presented AMR sensors that have a white noise of 200 $pT/\sqrt{Hz}$ [57].

Unlike coils, fluxgates, Hall effect and GMI sensors, AMR sensors can be easily miniaturized and have dimensions smaller than 100µm. For example, micro-sensor arrays based on anisotropic magnetoresistances with size of 16 x 5 μm^2 are designed for medical applications [58]. AMR sensors of 50 x 20 μm^2at size are used for NDT application [59]. Also AMR has been used in pulsed eddy current non-destructive testing (PEC NDT) [60]. We can also note that AMR sensors are used in the development of magnetometers that have recently become a built-in feature in most tablets and smartphones around the globe [61], and for vehicle speed and length estimation [62].

The response of AMR sensors has the disadvantage of not being linear but a specific configuration called barber pole where the angle is fixed around 45° is currently used to linearize AMR sensors. They present a saturation point in mT range and are not absolute sensors. Also, a very strong magnetic field (~200 mT) [26] can cause a permanent change in magnetization direction of AMR material, which makes the AMR sensor unusable.

1.9.2 Giant magnetoresistances (GMR)

Giant magnetoresistance sensors (GMR) have replaced the AMR sensors, as they allow high storage density due to their high sensitivity and their smaller size. In terms of resistance variation, the GMR is four to five times higher than the AMR. A giant magnetoresistance is a multilayer sensor formed by a series of thin ferromagnetic and non-magnetic layers. The thickness of individual ultra-thin layer can be few nanometers. The resistance of the GMR reacts with the application of external magnetic field. The phenomenon of GMR has been discovered by two European Nobel Prize winners [63, 64] in 1988: Albert Fert and Peter Grünberg (Figure 1.13).

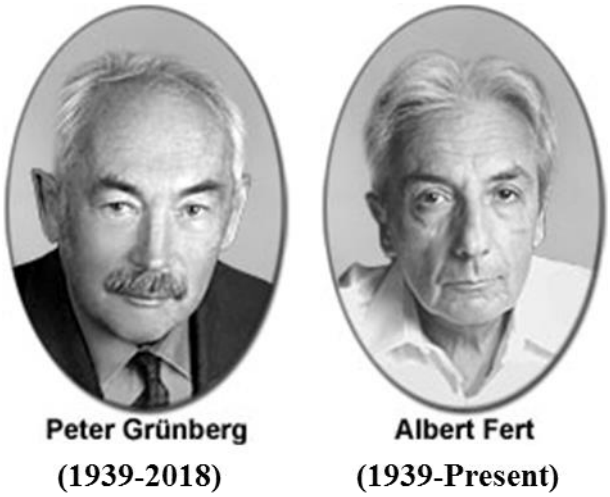

Figure 1.13- The two discoverers of GMR

The magnetoresistance ratio of GMR may reach up to 50 % [65], typically the sensitivity of GMR sensors are between 15 and 40 V/V/T when they are biased with 1 V. The white noise of GMR sensors is less than 0.5 nT/√Hz at room temperature [66]. Specific technologies integrate GMR sensors with micron-size and are able to achieve $fT/\sqrt{Hz}$ detectivities in the white noise leading the possibility to detect weak biomagnetic signals [67].

For example, GMR sensors have been used for detection of "Influenza A Virus" [68]. GMR sensors of 75 ×40 μm^2 size with white noise level at $nT/\sqrt{Hz}$ and sensitivity of 8.5 V/V/T, are used to estimate the magnetic properties of diluted ferrofluid for biomedicine application [69].They are widely used in hard disk read heads where they detect the magnetic coding of the bits. GMR sensors based spin torque oscillators (STO) with lateral size of 70nm are integrated to CMOS circuit [70]. Figure 1.14 shows an example of static field mapping realized in CEA SPEC laboratory for Earth Science application, in particular micrometeorite magnetization mapping. The discovery of gradient-field GMR sensors makes them interesting for pulsed eddy current testing method, as the gradient-field measurements give better sensitivity and accuracy in detection and sizing of hidden corrosion in layered conductive structures [71].

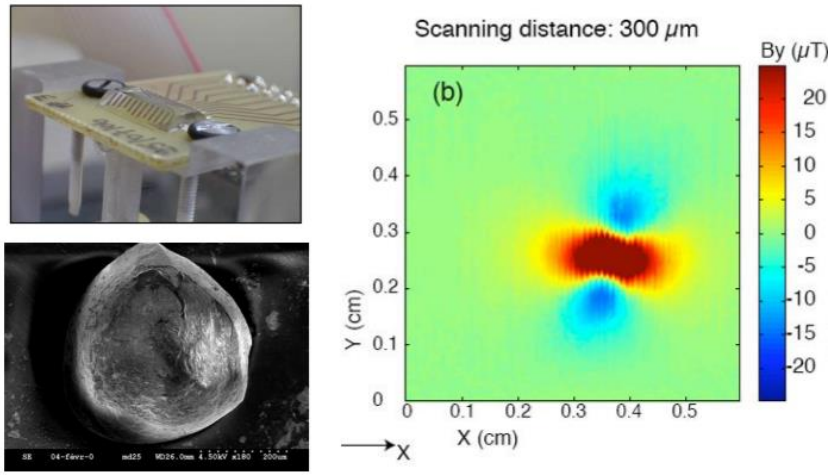

*Figure 1.14- **Left**: GMR scanning element for magnetic field mapping. SEM picture of a 450µm meteorite collected in Antarctica, **Right**: Magnetic mapping of the meteorite magnetic dipole. Coll. Cerege – Jérôme Gattacceca* [66].

GMR sensors are not absolute sensors and have also a saturation that may limit their operating range.

We will describe in the following part GMR technology in more details.

1.9.2.1 GMR with spin valve structure

Spin valves are a particular case of multilayered structure [72] composed of a hard layer, a spacer and a free layer. The nanometric layers are stacked according to the Figure 1.15.

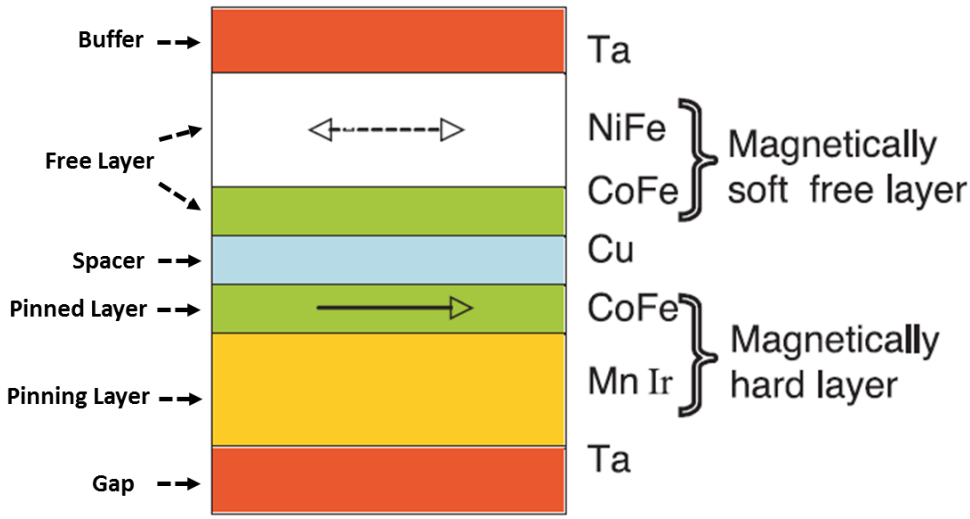

Figure 1.15- Example of spin valve GMR [73]

The hard layer has high coercivity. This layer is usually composed of a pinned ferromagnetic layer and an antiferromagnetic (AF) layer (pinning layer). The small external magnetic field to detect has no impact on the AF layer. This AF layer is used to fix the magnetization orientation of the pinned ferromagnetic layer due to exchange bias direct pinning. Thus, magnetization orientation of hard layer is fixed. The magnetization of free layer is easy to orient with external magnetic field. The free layer is separated from the hard layer by a conductive layer (spacer) that is sufficiently thick (2-5nm), so that the magnetic coupling between free and hard layers is weak and their magnetizations are independent. Paragraph 4.5 gives a detailed example of GMR of spin valve used in our work.

1.9.2.2 GMR effect

To illustrate the principle of the GMR sensors, we consider a configuration composed by a stack of ferromagnetic layers with parallel magnetization and anti-parallel magnetization (Figure 1.16). A nonmagnetic conductive layer is placed between the two ferromagnetic layers in the two cases.

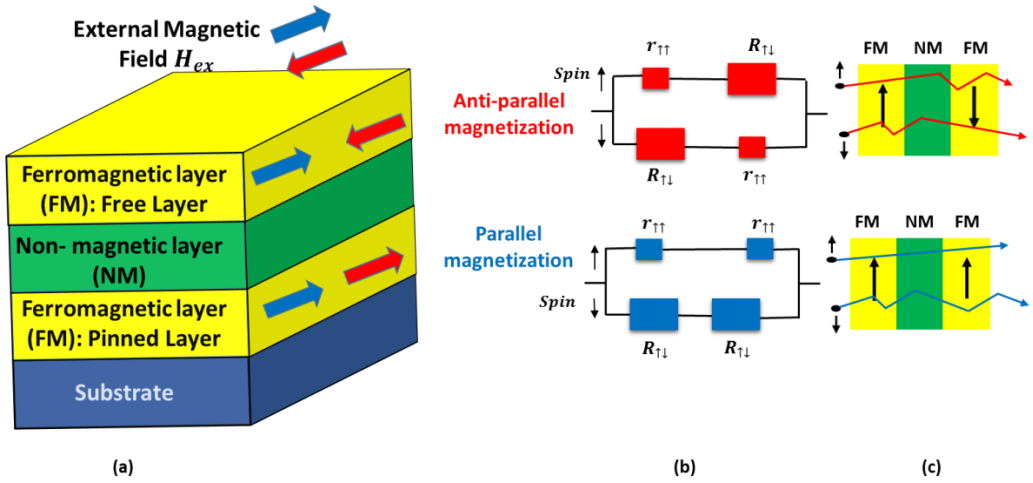

Figure 1.16- GMR structure: ***(a)*** *Free layer, spacer and pinned layer. The spacer is non-magnetic (NM);* ***(b)*** *The equivalent electrical circuit with two conducting channels is shown for anti-parallel magnetizations (red) and for parallel magnetizations (blue);* ***(c)*** *The figures at the top illustrate the trajectory of the electrons in antiparallel configuration and illustrate at the bottom the parallel configuration .*

Electrons have only two possible directions: upwards or downwards. In anti-parallel configuration (Figure 1.16), electrons are diffused and hence the resistivity of the structure is high (red case). The spin up and spin down currents pass through each

ferromagnetic magnetization layer opposite to their spin. The equivalent resistance $R_{\perp}$ is:

$$R_{\perp} = \frac{R_{\uparrow\downarrow} + r_{\uparrow\uparrow}}{2} \cong R/2 \tag{1-12}$$

In the configuration with parallel magnetization of layers (Figure 1.16), the spin up electrons pass through structure nearly without diffusion, while the spin down electrons are strongly scattered (blue case). The spin electron current anti-parallel to the magnetization vector encounters two resistances $R_{\uparrow\downarrow}$ while the inverse spin current encounters two resistances $r_{\uparrow\uparrow}$ (Figure 1.16.c). The equivalent resistance $R_{||}$ of the structure is:

$$R_{||} = 2\,\frac{R_{\uparrow\downarrow}\, r_{\uparrow\uparrow}}{R_{\uparrow\downarrow} + r_{\uparrow\uparrow}} \cong 2r, if\ R_{\uparrow\downarrow} \gg r_{\uparrow\uparrow} \tag{1-13}$$

Thus the resistance in the antiparallel state is higher than the resistance in the parallel state.

1.9.2.3 GMR sensitivity

The GMR sensitivity can be calculated using the sensitivity curve obtained by measurement of sensor response in homogenous magnetic field. To obtain sensitivity curve, we put the GMR in the center of the Helmholtz coil (Figure 1.17). Typical GMR response of a linearized sensor is shown in Figure 1.18.

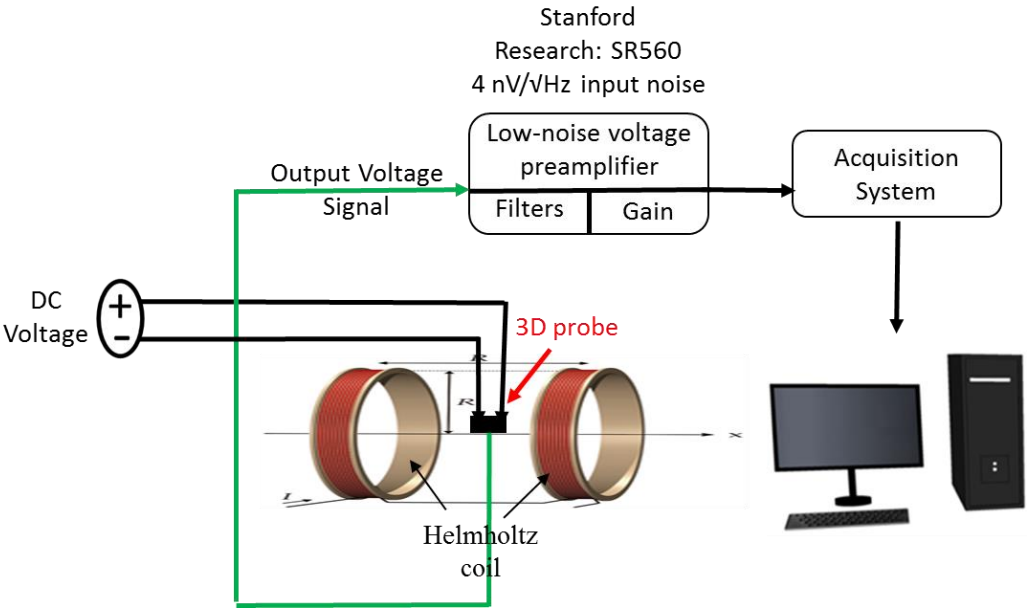

Figure 1.17- Measurement scheme of GMR sensitivity.

The Helmholtz coil is excited by a sinusoidal signal from the wave generator. The relative variation of magnetoresistance (MR) is calculated according to equation (1-10) with $R_0 = \frac{R_{||}+R_{\perp}}{2}$.Thus, the MR ratio could be defined as follow :

$$MR = \frac{R_{\perp} - R_{||}}{2R_0} \tag{1-14}$$

The sensitivity S_{GMR} (V/T) is the variation of output voltage on the applied field given by the following equations.

$$S_{GMR}\,(V/T) = \frac{\Delta V}{\Delta H} = \frac{\Delta R.\,i}{\Delta H} \tag{1-15}$$

The sensitivity in (%/mT) is:

$$S_{GMR}\,(\%/mT) = \frac{\Delta R}{\Delta H}\,\frac{1}{R_0} \times 100 \tag{1-16}$$

An example of MR calculation is presented: a DC current of 3 mA is applied to the GMR sensor. This GMR sensor of spin valve type has a resistance of 79.6 Ohms. The resistance variation of GMR as a function of magnetic field (H) is linear in the range [-2 mT ; +2 mT] (Figure 1.18). In this case, $R_{\perp}$ = 81.7 Ohms and $R_{||}$ = 77.5 Ohms. These sensors have MR ratio of 5.2 %. The S_{GMR} is 6.2 V/V/T.

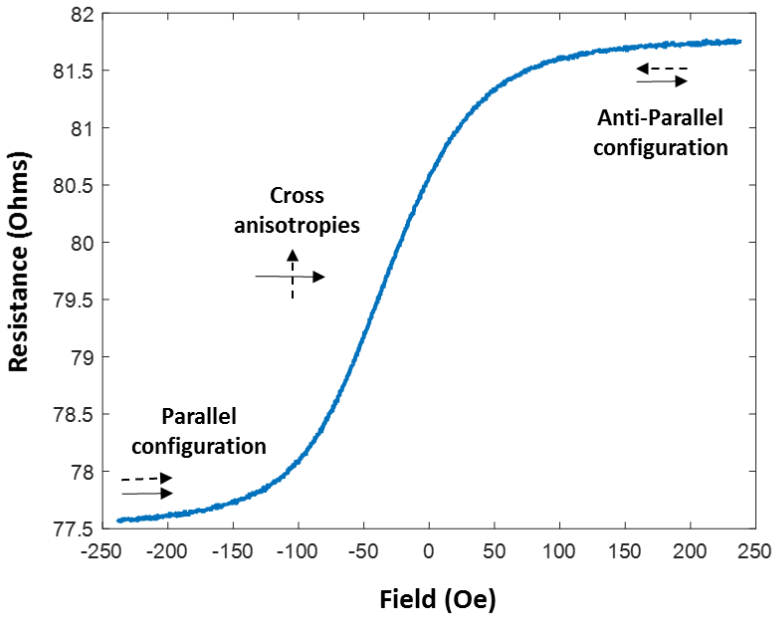

Figure 1.18- Example of GMR response as function of magnetic field applied along its sensitivity axis

1.9.3 Tunnel magnetoresistance (TMR)

Another type of multilayer system with resistivity variation as a function of relative orientation of layers magnetizations is the Tunnel Magnetoresistance (TMR) sensor. Tunnel Magnetoresistance effect has been proposed in 1975 by Michel Jullière [74], and has been observed in room temperature in 1995 [75, 76]. Contrary to GMR systems, the spacer is composed of an insulator layer. TMR is a quantum mechanical effect, which occurs when two ferromagnetic layers are separated by a few atomic layers of insulator. The transfer of electrons from one ferromagnetic layer to another is done by tunnel effect. Transmission of electron is possible only if there is a free state with the same energy and same spin on the other side of the insulator. Yuan [77] and Lee [78] describe a method of tunneling magnetoresistance (TMR) fabrication. Figure 1.19 shows a typical stack of tunnel junction.

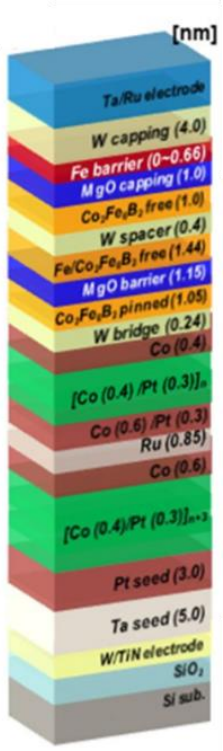

Figure 1.19-Typical stack of TMR sensor on thickness of Fe diffusion barrier for double MgO-based p-MTJ spin-valves with top $Co_2Fe_6B_2$ free layer [79].

The high magnetoresistance ratio of TMR sensors with MgO barrier (spacer) makes them very attractive. Tantalum (Ta) layer is an interface layer. The quality of the interfaces is essential for performance of TMR sensor. MR exhibits a higher

sensitivity and higher signal-to-noise ratio (SNR) compared to Hall sensors and other magnetoresistive sensors, including GMR [80]. TMR sensor has greater magnetoresistance ratio than GMR, especially TMR with MgO junction that can reach MR ratio up to 1000% [81]. Janeiro describes in [82] a TMR of size 5x20 μm^2that has white noise of 13.8 $nT/\sqrt{Hz}$. Besides high spatial resolution and high field sensitivity, the TMR sensors have low energy consumption.

TMR sensors are used in non-destructive testing and biomedical applications. Pelkner describes in [83] the benefits of GMR and TMR sensors in terms of high spatial resolution testing for different NDT applications. We find the TMR in MRAM (magnetoresistive random access memory) memory and in read head [79]. Lei presents in [84] a contactless scanning prototype device based on TMR sensors used in biomedical application for quantification of Magnetic nanoparticles (MNP) in lateral flow strips (LFS). Also, TMR sensors are used for nanosatellites space application, with white noise of 150 $pT/\sqrt{Hz}$ and volume about ($25 \times 25 \times 10\ mm^3$) [85].

However, the injected voltage in TMR sensors is limited and the magnetoresistance ratio of TMR decreases if the injected voltage increases. Despite its higher sensitivity compared with AMR and GMR sensors, the 1/f noise limits its detectivity and thus its performance. Also the high coercivity and low linearity of TMR sensors remain a serious problem [86].

1.10 Conclusion

This chapter presented an introduction of magnetic sensors principles. Table 1 presents a summary of the main properties of these magnetic sensors.

	Measuring range	Detectivity ($pT/\sqrt{Hz}$)*	Dimensions	Continuously operating	Frequency (Hz)	Measured quantity	Material type
Coil	0.1fT<B<100T	1 at 1kHz for 1cm²	> 30x18x100 μm^3	No	$10^{-3} - 10^9$	Derivative of the flux	Massive
Fluxgate	0.1nT<B<0.01T	3 at 1 kHz	>1×1×1 mm^3	yes	$DC - 10^3$	flux	Massive
Hall Effect	1μT<B<1T	10^5 white noise	<4×3×1.5 mm^3	Yes	$DC - 10^5$	field	Thin film
GMI	0.1nT<B<1mT	100 at 1 kHz	<5mm×30 μm	Yes	$DC - 10^4$	Flux	Massive
AMR	1μT<B<5mT	1000 white noise	μm size	Yes	$DC - 10^7$	Field	Thin film
GMR	1nT<B<5mT	50 white noise	μm size	Yes	$DC - 10^8$	Field	Thin film
TMR	1nT<B<5mT	10 white noise	μm size	Yes	$DC - 10^8$	Field	Thin film

Table 1: Comparisons of characteristics of different magnetic sensors [34, 54, 87]

We can compare the magnetic sensors based on two parameters: size and detectivity of these sensors. The limits related to the fabrication of very small coils, GMI and fluxgate sensors limit their use in application that need high spatial resolution. For example, we need high spatial resolution to detect very small defects in NDT and to distinguish between small magnetic objects for magnetic imaging.

Figure 1.20 shows experimental comparison of detectivity between different magnetic sensors [34, 88, 89].

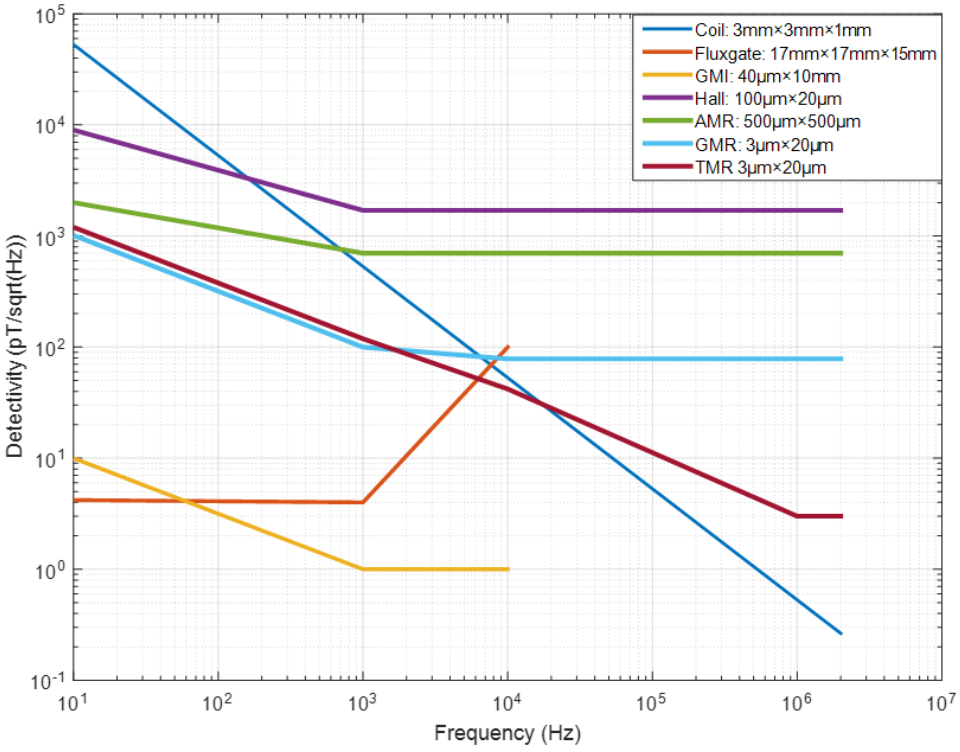

Figure 1.20- Comparison of the detectivity of magnetic sensors : coil, fluxgate, Hall, GMI, AMR, GMR and TMR sensors

We can observe in Figure 1.20 that the fluxgate and the GMI sensors have a lower noise level, but have higher size than MR sensors. The micro-Hall sensor is smaller in size and has linearity response, but is characterized by high noise level. The magnetoresistive sensors have micron size, and high detectivity independent of frequency in the white noise, that make them more effective at small scale.

For applications in NDT and micromagnetic imaging, we need a micron-size spatial resolution with high detectivity, so the best tradeoffs between magnetic sensors are MR sensors. With simple comparison between AMR and GMR sensors, we can conclude that GMR sensors are the best for our application in terms of thermal noise and operating frequency range. The high 1/f noise of TMR sensors at low frequencies limits their interest compared to GMR and they are more difficult to process. The tradeoff between spatial resolution and the noise level justifies the choice of GMR technology for the development of probe using in NDT and magnetic imaging (micromagnetic scanning).

Chapter 2. Non-destructive testing

2.1 Introduction

We will describe in this chapter some NDT methods and their application limits. We will consider the performances of eddy current method. One of the objectives of this work is to develop eddy current probe based on magnetoresistive sensors for detection of surface and subsurface small defects in conductive materials. Finally, we will present in the conclusion of this chapter a study, that show more specifically the choice of the GMR sensors between the MR sensors to replace coils for eddy current non-destructive testing (EC NDT).

2.2 Non-destructive testing

NDT (non-destructive testing) methods are based on different technologies enabling to guarantee structure and product reliability. They are essential in many industrial sectors, including transportation, automotive, petrochemical, nuclear and aircraft industries [90, 91]. NDT is used in industry from the beginning of the 20th century.

Figure 2.1- Non-destructive testing in the aerospace industry [92]

In general, NDT methods have the same principle which can be described down into four steps:

- An excitation energy emits signal in the controlled part: electromagnetic or acoustic waves;
- An interaction is created between the controlled part and emitted signals

- Receiver that receive the signals resulting from these interactions.
- Acquisition system in order to interpret the received signals and to deduce the properties and the state of the part under test.

In the following, we present a general review of some techniques used in NDT, and we will detail eddy current method.

2.3 Optical methods

Visual inspection is widely used in NDT. To control surfaces that are inaccessible to direct vision of operator, many optical instruments like endoscope and stroboscope are developed to increase the performance of the eye or more generally to give the possibility of surface control. However, the non-automatic optical methods have limits related in particular to the tiredness of operator. Thus, fully automatic optical control equipment has been developed.

Another optical method shown in Figure 2.2 is Optical Holographic technique developed for testing of materials (HNDT). The method could used to detect small displacement of material surface. A surface or near-subsurface defects could be detected due to surface displacement changes. Holography creates a three-dimensional image of an object having arbitrary shape. HNDT allows to detect and to measure deviation and dimension of the target [93, 94].

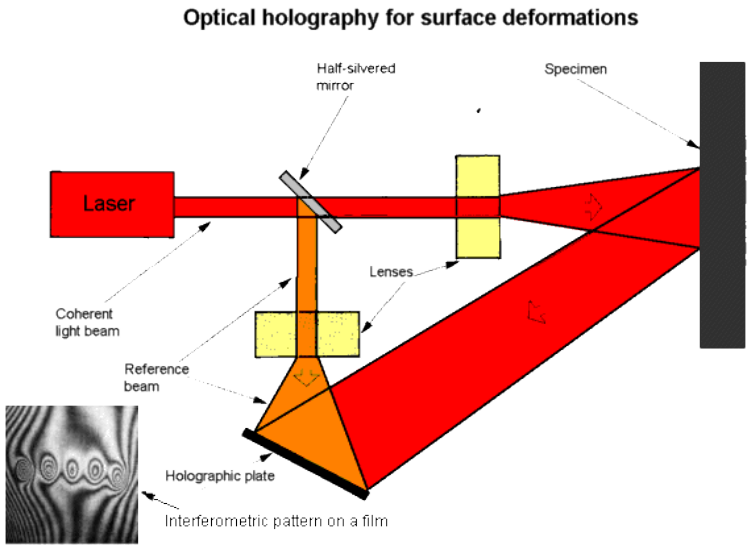

Figure 2.2- Optical instrument for surface deformations [94]

2.4 Penetrant Testing

Non-destructive testing by Penetrant Testing (PT) is the oldest NDT method as its first application would date to the end of the 19th century. PT is a low-cost inspection method and it is widely used to localize surface-breaking defects in all non-porous materials (metals, plastics or ceramics). The piece is subjected to the action of a penetrating liquid (or gaz). The physico-chemical characteristics of this liquid allow it to penetrate inside the cracks of specimen. Its application is done either by immersion or by spraying. PT method allows the detection of the discontinuities on the surface of controlled piece in the form of colored or fluorescent indications, observed on a white background or on a black background. The control of PT method is performed under artificial white light or daylight (colored bleeding) or under ultraviolet radiation (UV-A). The drying time, "dwell time", is the time to soak into cracks (generally 5 to 30 minutes). The dwell time mainly depends on used penetrant, material under test and the size of cracks sought [95]. Figure 2.3 presents an example of penetrating testing steps. PT is widely used for inspection ensuring surface flaws detection in large areas and structures with complex shapes. However, this method is highly polluting and is highly dependent on human interpretation of results.

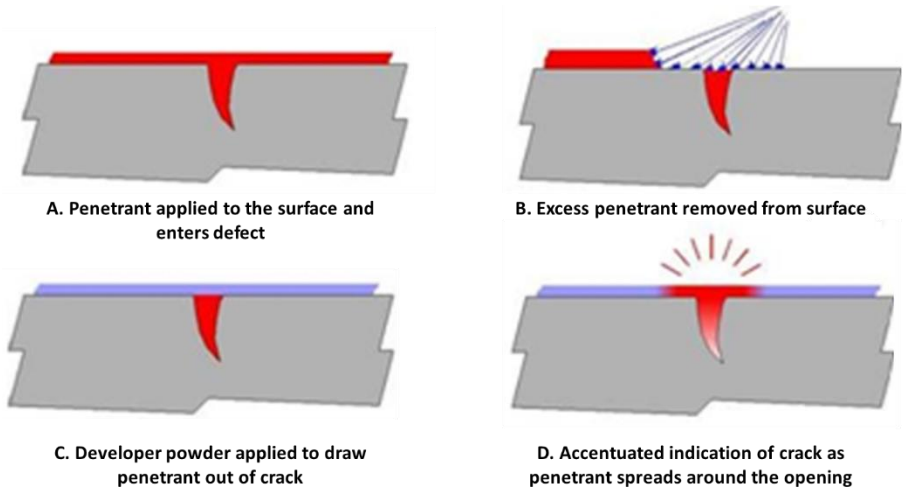

Figure 2.3- The four steps of PT technique

2.5 Magnetic particle inspection (MPI)

Magnetic particle inspection is method of detection of surface defects in ferromagnetic materials. Magnetic flux is created in the material and in the presence of defect the

flux leakage will be created. To detect this flux leakage ferrous particles are applied to the part under test (like in penetrant testing). If there is no flux leakage thus there is no defects in tested part, particles distribution is homogeneous. In the presence of flux leakage, ferrous particles are attracted to this zone and form an indication of the defect. MPI is very attractive for surface defects detection however it has the same limitations as penetrating testing in terms of detection and pollution factors.

2.6 Ultrasonic testing

Ultrasonic testing (UT) exploits the propagation properties of ultrasonic waves (transmission, reflection and absorption). It consists of emission of acoustic waves in controlled piece and analyzing the echo returning from this piece. The sensors are composed of one or more transducers acting as transmitter or receiver (Figure 2.4).

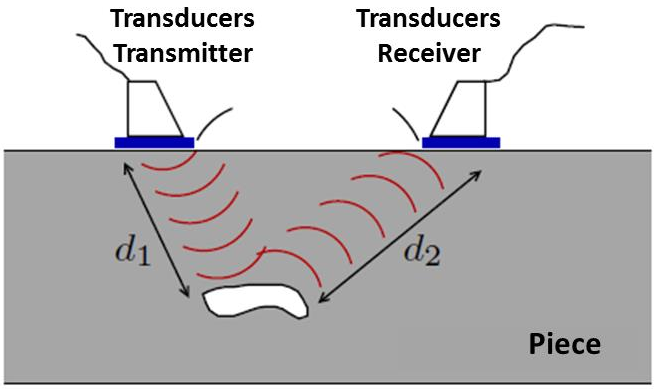

Figure 2.4- Shema of Ultrasound Principe [35]

Three types of transmitters are used to generate ultrasound signal: piezoelectric generators, magnetostrictive transmitters and electrostrictive emitters. Receiver transducer is located in generally on the same side as transmitter. The emitted acoustic wave encounters various elements on its path like background of the piece and defects. This reflected wave is received by the receiver transducer with some delay due to the propagation of wave across the piece. If the velocity v of wave propagation in the material is known, it allows to distinguish between the echo from the bottom of the piece and the echo from a defect located inside the piece. The propagation time δt of the reflected wave from the defect depends on the distance between emitter and target 'd_1' and on the distance between receiver and the target 'd_2'. δt is expressed by the following equation:

$$\delta t = \frac{d_1 + d_2}{v} \quad (2\text{-}1)$$

UT technique allows to locate or to characterize the defect. Also thickness measurement could be realized. There are other techniques in ultrasound to improve the detection and characterization of objects like for example phased array [96] or laser ultrasound. Binder layer (water, oil) is needed to be applied between transducers and controlled piece [97].

2.7 Radiography

Radiography method could be applied to all solid materials, which thicknesses vary from few micrometers to several hundred millimeters, taking into account the nature of controlled medium and nature of radiation. Radiography could be defined as a cross-sectional 2D imaging technique that aims to create the image of a solid object from the set of its projections [98]. The interest of this method is the identification of internal defects. Radiography method consists of emitting electromagnetic radiation of short wave length like X-ray or γ-rays in the piece. Photons energy will be partially or completely absorbed inside the piece. The receiver on the other side of controlled piece will detect the photons. Sensitive films, fluorescent screens or CCD detectors could be used as receiver. Obtained images can be directly interpretable, have good spatial resolution. For X-ray imaging (Figure 2.5), we can get the projections by directing an X-ray beam to the object from different orientations and measuring its intensity attenuation during the traversing of X-ray in the object. Images with good resolution could be obtained, however important safety requirements should be applied.

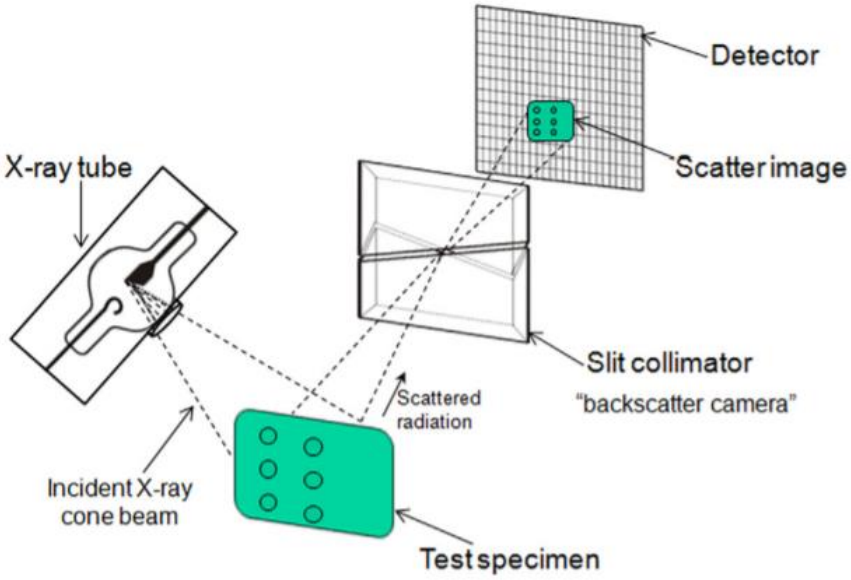

Figure 2.5-Example of uses of Radiography method [99]

2.8 Magnetic flux leakage

Magnetic flux leakage method is a technique used for corrosion and pitting detection in steel structures. A magnet is used to magnetize steel. Magnetic flux is created in material under test. If there is no defect, flux lines will pass through material. In the presence of a defect or corrosion, magnetic leakage field will be created in the area of a defect. This magnetic leakage field is detected by magnetic sensitive sensors (Hall sensors, GMR sensors) placed between the poles of magnet.

2.9 Eddy current testing

Eddy current technique has been discovered by the French scientist Jean Bernard Leon Foucault in 1855. This method is used since 1926. Eddy current testing (ECT) is a magnetic method used to detect surface and sub-surface flaws in conductive materials [100]. ECT is based on the interaction between magnetic field source (emitter coil), the test material (piece) and receiver (magnetic sensor) [101]. The induced current density depends on applied current, on geometry and dimensions of excitation coil [102]. Eddy currents are created in conductive material by emitter. The emitter is in general a coil traversed by excitation current I_{ex}, which produces a magnetic field variable in time determined by Maxwell equations:

$$\overrightarrow{rot}\vec{H} = \vec{J} + \frac{\partial \vec{D}}{\partial t} \quad (2\text{-}2)$$

$$div\vec{B} = 0 \quad (2\text{-}3)$$

$$\overrightarrow{rot}\vec{E} = -\frac{\partial \vec{B}}{\partial t} \quad (2\text{-}4)$$

$$div\vec{D} = \rho \quad (2\text{-}5)$$

$\vec{E}$ and $\vec{H}$ are respectively the electric and the magnetic fields, $\vec{D}$ and $\vec{B}$ - the electric and magnetic inductions, $\vec{J}$ - the surface density of electric current and ρ - the density of electrical charges.

The variable magnetic field will create eddy currents in conductive material. According to equation (2-4), these eddy currents have same frequency as the excitation current. The induced currents circulate locally in the material (Figure 2.6) and have spatial distribution that depends on excitation magnetic field, electrical conductivity σ, magnetic permeability μ of the examined piece. In the presence of inhomogeneity like defect or inclusion, physical properties (conductivity and permeability) are changed, eddy current lines are deviated and reflected magnetic field will be changed.

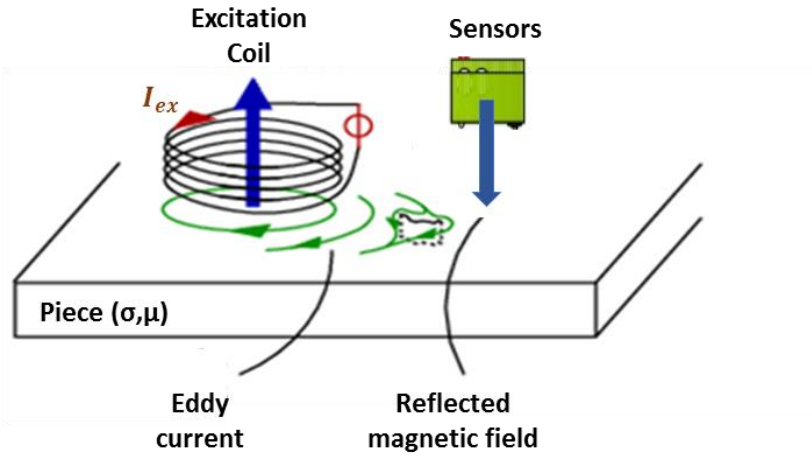

Figure 2.6- Principle of eddy current generation [35]

Receiver detects this reaction magnetic field resulting from the interaction between the induced currents and the excited material (piece).

Eddy current distribution

The distribution of eddy current is not homogeneous at different depth and is governed by the Maxwell equations. The intensity of eddy current in conductive material characterized by electrical conductivity $\sigma\ (S/m)$ and magnetic permeability $\mu(H/m\ )$, decreases with the depth $z\ (m)$. In the case of infinitely thick piece with a flat surface, the current density along z-axis $J_z(A/m^2)$ excited at frequency $f(Hz)$is expressed by [103]:

$$\mathrm{J_z(z,t)} = \mathrm{J_0} e^{-z\sqrt{\pi f \mu \sigma}} \cos\left(wt - z\sqrt{\pi f \mu \sigma}\right), \tag{2-6}$$

where $J_0\ and\ w$ are respectively the maximum of current density at piece surface, and the pulsation of induced currents. According to equation (2-6), if the depth z increases, the current density decreases. This decreasing of current density as function of depth is shown in Figure 2.7.

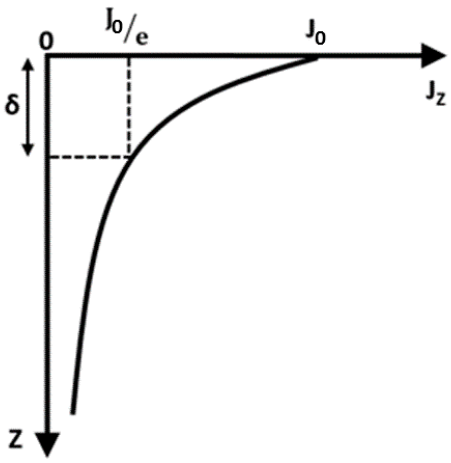

Figure 2.7- Evolution of current density as function of piece depth (z) in the case in the case of plane wave excitation [104].

The penetration depth $\delta\ (m)$, also called skin depth is the depth at which eddy current density decreases to the level of 37% of its surface value J_0 [105]. This skin depth is defined as:

$$\delta = \sqrt{\frac{1}{\pi\ f\ \sigma\ \mu}} \tag{2-7}$$

The magnitude δ allows the estimation of appropriate excitation frequency according to material electromagnetic parameters.

Figure 2.8 shows the evaluation of skin depth against frequency for different materials. At low frequencies the penetration depth is more important, thus for buried flaws detection low frequencies should be used, whereas for surface cracks with low penetration depth high frequencies should be used. Working frequencies of EC technique are from 10 Hz to 10 MHz. At low frequencies, the amplitudes of eddy currents are low, at high frequencies capacitive effects of inductive part will influence the measurement.

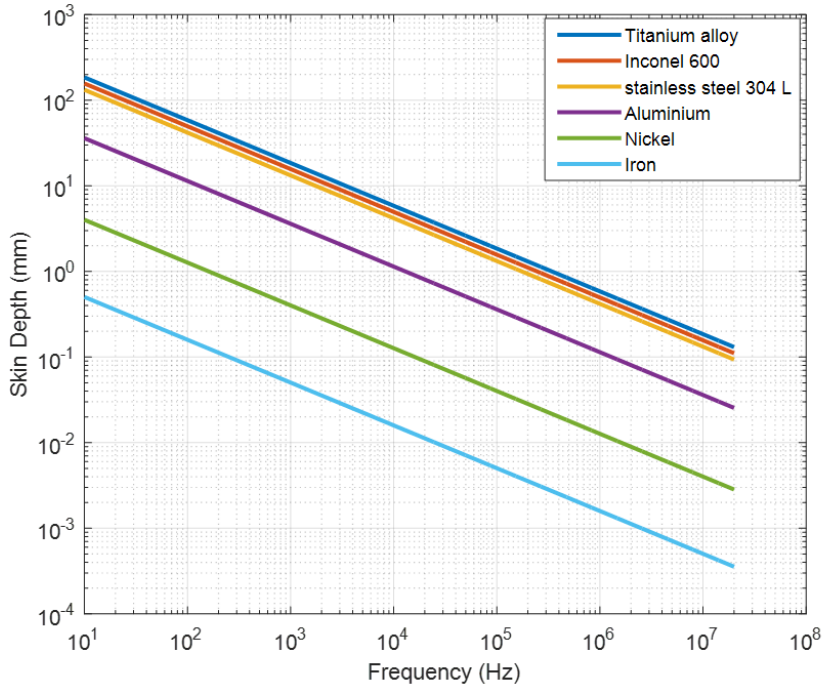

Figure 2.8- Evolution of skin depth against frequency for different materials

Receiver in eddy current

EC probe is composed of an emitter consisted of a coil and a receiver consisted of magnetic sensors. Inductive sensor (coils) could operate in emission-reception mode and in emission-reception separated mode. Other magnetic sensors could be used as receivers to increase the performances of EC probes.

Magnetic sensors and their performances for ECT have been reviewed in the Chapter 1. Figure 2.9 presents an example of MR array sensor based probe developed during IMAGIC project [106]. This project has been focused on the development of the probes with MR sensors as receivers with miniaturized electronics for detection of buried defects and small surface defects. Double coil has been chosen as emitter for

buried flaws detection, receiver array is formed of 32 GMR sensors. For surface cracks detection GMR and TMR array sensors of 32 and more elements have been fabricated. One wire emitter has been used for this application. Higher performances of GMR and TMR sensors in comparison with inductive sensors for detection of small surface defects have been shown.

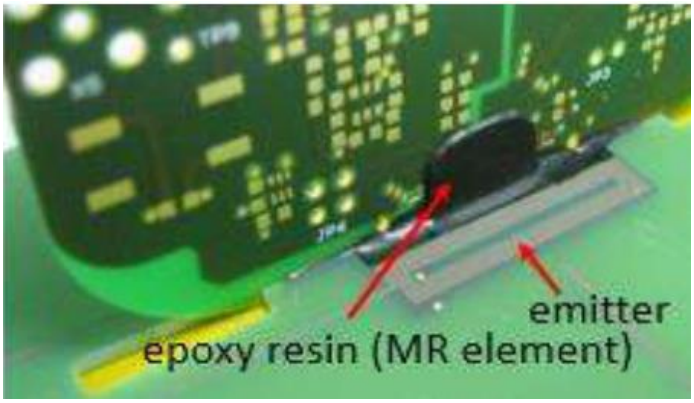

Figure 2.9- Photo of the IMAGIC MR probe for buried flaws detection [107]

2.10 Conclusion

This chapter introduces different NDT methods. In particular, we present in details the eddy current method. Table 2 presents a comparison of the main NDT techniques:

	Physics principle	Type of detected defect	controlled material	Strong point	Weakness
Optical method	Forming an image	surface	all	rapid	Fine defects detection
Penetrant Testing	Capillarity effect	surface defects	all except porous	global method, simplicity	Productivity, Little quantitative
Ultrasound	Disturbance of ultrasound wave	Surface/buried flaws	all	defect sizing	Coupling
Radiography	Flow attenuation	surface/buried	all	defect sizing	safety requirement
Eddy currents	Current perturbation	Surface and subsurface defects	Conductive material	defect sizing	Interpretation, sensitive to defect orientation

Table 2: Comparison of the main NDT techniques [96, 99, 100, 101, 108]

EC technique is a method that is widely used for defects detection in conductive materials. It also could be used in order to partially replace the polluting methods like penetrating testing and X-ray inspection. Nowadays EC testing is undergoing the change in order to answer to industrial specifications in terms of product quality. The aim is to detect very small (<100µm) surface cracks and deep buried flaws (under

several mm). In order to overcome the limits of conventional winding coils classically used in ECT in terms of detectivity at low frequencies and micro-coils fabrication limits, magnetic sensors have been investigated since several years as receivers for EC probes. Moreover, several components of magnetic field are needed to be measured for defects characterization. Oka et al. introduced EC probe using 3-axis measurement coil to characterize the shape of detected defect [109]. This probe has limitation due to its large size. During this PhD thesis 3D GMR based EC probe has been developed for detection and sizing of small surface cracks. This probe will be detailed in Chapter 4.

Chapter 3. Magnetic Imaging

3.1 Introduction

The second application of our probe is in micro-imaging application. This chapter will explore state of the art of local and non-local microscopes for magnetic imaging as well as weighing up their advantages and limitations. We will present more in detail the optical magnetic microscopy, because its spatial resolution is comparable to the 3D probe.

3.2 Microscope for magnetic imaging

By definition a microscope is an instrument allowing the visualization of small objects that are difficult to see by the naked eye. Microscopy probes allow surface mapping and the extraction of properties like topography, electronic density, interaction force, tunnel current etc. The major types of microscopy (optical, electronic, near-field ...) are similar in their basic principle, it is a result obtained by an interaction between an object and an energetic radiation. On the other hand, these different techniques are distinguished by their spatial resolution level (some Angstroms for near-field microscopy, 250 nm for optical microscopy) and by their magnification capacity (about 1000 for optical microscopy, about 100,000 for electron microscopy).

Microscopes can be classified as follow: microscope that takes directly an image of sample (wide field optical microscopes and transmission electron microscopes) or not directly by scanning the sample to be analyzed via a scanning point (confocal optical microscopes, scanning electron microscopes and scanning probe microscopes).

Scanning magnetic microscopy [110], scanning Hall probe microscopy [111, 112], scanning superconducting quantum interference device microscopy [113], Lorentz transmission electron microscopy [114], Kerr microscopy [115], and others are used to study magnetic structure and small magnetic elements in many domains [116, 117, 118] Scanning techniques offer a good spatial resolution (nanometric) and good magnetic resolution (for example up to femtoTesla for SQUID [119] and about microTesla resolutions for Hall probes [120]). But, these techniques don’t allow the

rapid acquisition of entire sample surface images. Microscope that takes directly an image (global microscope) has fairly poor spatial resolution compared to a scanning microscope. This resolution of microscope depends on the size of sensors used and also of the distance sensor-sample. For example, Magneto-optical (MO) imaging have spatial resolution at micrometer range, and magnetic resolution in the order of 0.1mT.

Table 3 shows a comparison of microscopy:

	Measured technique	Lateral resolution (nm)	Physical Quantity
Lorentz microscope	Electron	10nm	stray field
Spin-polarized scanning tunneling microscopy (SP-STM)	Transport	atomic resolution	Spin polarization of sample
MFM (Magnetic Force Microscopy)	Magnetic Force	10	stray field
SMRM (Scanning magnetoresistance microscopy)	Transport	micrometers	stray field
Garnets films, Kerr	Optical	Sub-micrometers	Stray field / magnetization
Nitrogen Vacancy (NV) centers	Optical	~50	stray field

Table 3- Comparison between different types of Microscopy [121, 122]

Finally, the efficiency of different microscopes techniques depends on application domain and their limits in terms of spatial resolution and field sensitivity. In the following, we detailed some microscopy cited in Table 3.

3.3 Transmission electron microscopes (TEM)

The transmission electron microscopes (TEM) has series of electromagnetic and electrostatic lenses to focus a high energy beam of electrons on a sample. In the TEM microscope, to produce an image, the electrons pass through the sample, analogous to basic optical microscopy [123]. This microscope can attend a resolution of 0.1 nm. It is very efficient to help researcher in cancer research, virology, materials science as well as pollution, nanotechnology and semiconductor research. For example, it allows to obtain three-dimensional views of the virus (20-300 nm) and the DNA (2 nm in width) samples [124]. The Lorentz microscopy based on TEM is a useful tool to get information of both physical structure and micromagnetic structure of the thin samples at nanoscale. It allows exploring the magnetic properties of the specimen. There are two modes in Lorentz microscopy: the Fresnel mode, and the Foucault mode [125].

The specimen should be less than 100 nm thick, so the electrons can pass through it. This thickness limitation is the main drawback of TEM microscope.

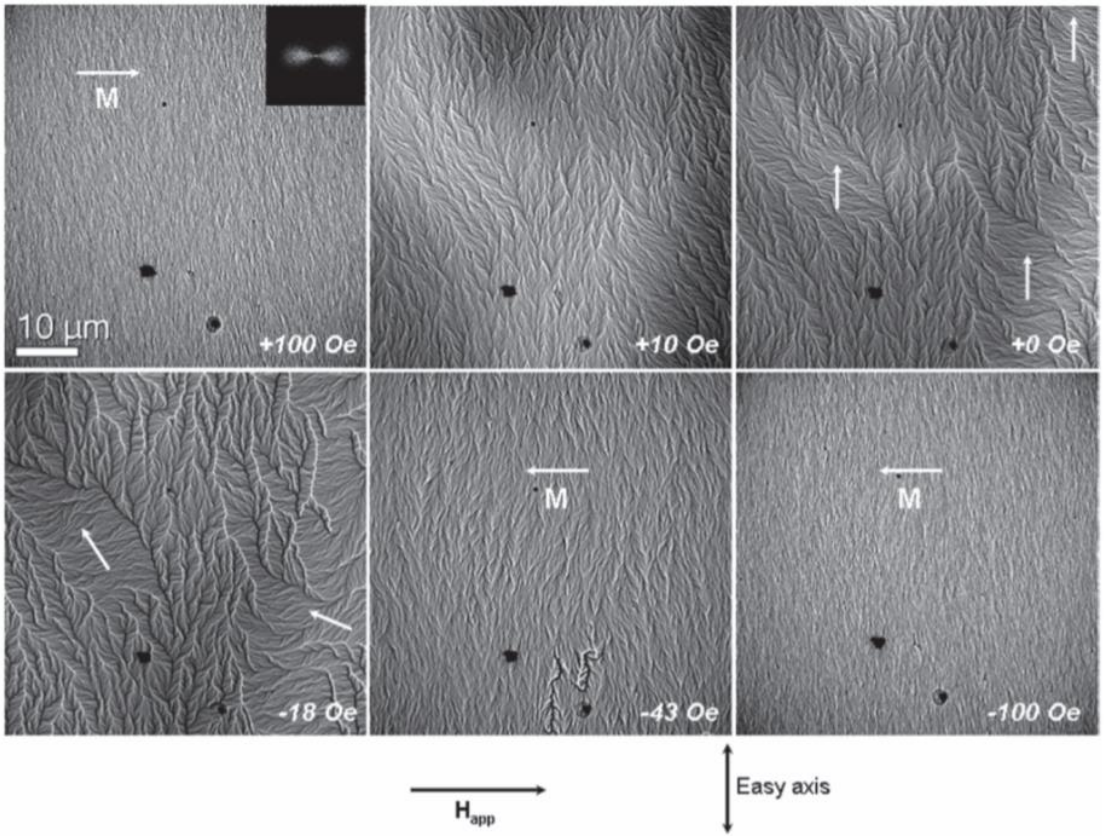

Figure 3.1- In situ TEM study of magnetization reversal in Co80Ir20 film: Fresnel images in a hysteresis sequence on the hard axis in plane of the film [126].

3.4 Local probe microscopy

Local probe microscopy has become an essential research tool in the last few decades, particularly in the development of nanotechnology and semiconductor. Local probe microscopy has started with the invention of tunneling microscopy (Binnig, 1982 - Nobel Prize in 1986), and the atomic force microscopy (Binnig, 1986). The principle function of this microscopic technique consists of scanning the surface using a probe (tip) placed to the proximity of the surface and measuring the interaction between the probe and the surface of the specimen. It exists currently a variety of scanning probe microscope able to detect diverse properties as the stray field emitted by a magnetic sample (MFM), ferroelectric properties (PFM)…

The atomic size of the tip (the tip is ideally a cone ending by single atom) allows to obtain atomic size resolution images, which not possible with traditional microscopy.

One difference between atomic force microscopy and competing technologies such as optical microscopy and electron microscopy is that AFM does not use lenses or beam irradiation. Therefore, it does not suffer from a limitation in spatial resolution due to diffraction and aberration. The local microscope allows obtaining indirectly the image thanks to the interaction between the tip and the surface. Image obtained by the local microscopy is put together by slowly scanning sample surface. Scan areas range from a few to 200 micrometers. In local microscopy, piezoelectric scanning moves the sample in an x, y and z directions, wich allow to precise sensor-to-sample distance.

3.4.1 Scanning Tunneling Microscopy (STM)

Scanning Tunneling Microscopy (STM) discovered by Binning measures surface electronic states using a tunneling current between the probe tip and a sample surface. The tip is formed by one single atom at its extremity. The distance between point and sample is few Angstroms (Figure 3.2). The electrons are forced to pass from the tip to the conductive sample through the insulating layer composed by air or vacuum and are measured by an "ammeter". The electric current is therefore a tunnel current that decreases exponentially with the distance between the tip and the specimen. STM allows determining the morphology and the density of electronic states of conductive or semi-conductive surfaces with atomic spatial resolution. Among STM microscopy, the spin-polarized scanning tunneling microscopy (SP-STM) can provide information on magnetic domain and electronic structure with extremely high spatial resolution. SP-STM is sensitive to magnetic local density of states of the sample surface, the spin polarization of the magnetic surface.

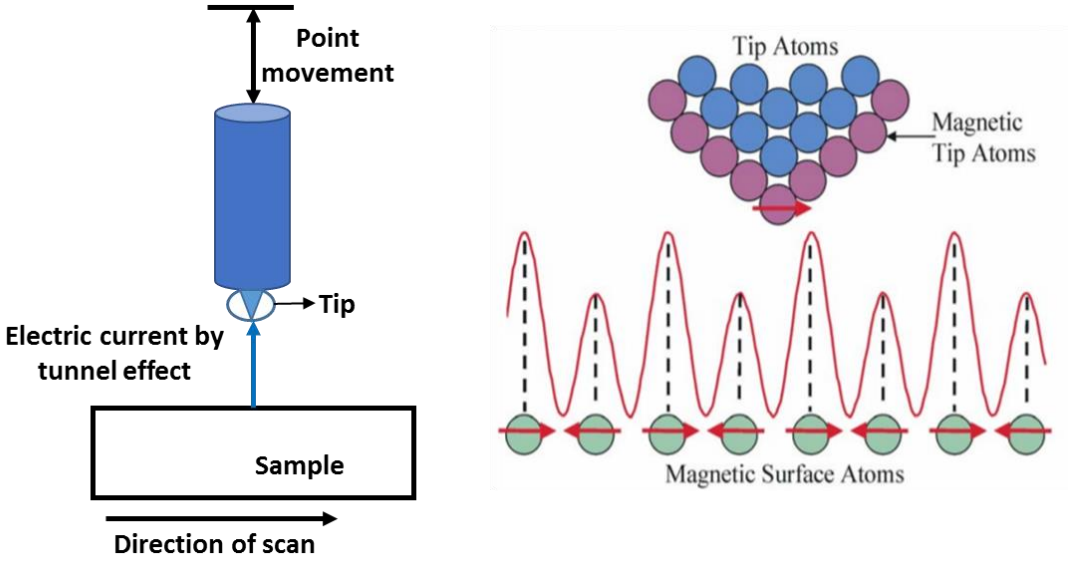

*Figure 3.2- Schematic view of an STM **(left part)** Schematic illustration of the SP-STM method* [127] ***(right part)***

We show in Figure 3.2 (right part) that the tunneling current depends on the relative magnetization orientations between tip and sample spins.

The major limitation of STM is that the technique is only efficient for conductive samples, in particular for applications in semiconductor physics and microelectronics [128, 129]. Historically, this technique served as the groundwork for the subsequent advancement to Magnetic Force Microscopy (MFM).

3.4.2 Magnetic force microscopy (MFM)

Binnig has continued innovations of local probe instruments in 1986 by demonstrating the ability to scan the surface of the sample, whether it is conductive or not. A new microscope named Atomic Force Microscopy (AFM) allows the measurement of forces between the surface of the sample and the tip [130, 131, 132]. AFM allows the analysis of all types of surface of materials in air, in liquid medium or in controlled atmosphere. Depending on the forces in presence, the AFM can take images of different physical or chemical surface information such as: mechanical, magnetic, electrostatic properties, etc. Atomic force microscopy provides the topography of a surface of about: $50 \times 50\ \mu m^2$, with vertical resolution less than one nanometer and lateral resolution of the order of nm [131].

The tip is placed in the end of a flexible cantilever, which acts as a spring (Figure 3.3.a). The deflection and torsion measurement by optical or tuned fork technics of the cantilever allows the measurement of forces between the tip and the sample (Figure 3.3.c).

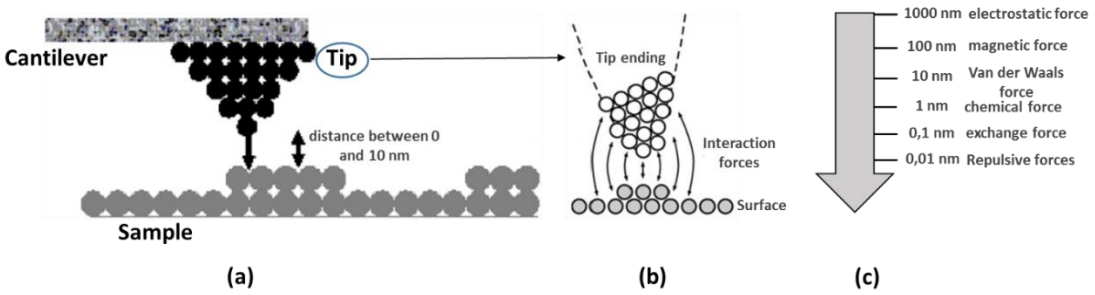

Figure 3.3- Atomic force microscopy principle (a) Tip form (b) Long- and short-range (interatomic) forces dependent of various distance *(c)* [131, 133]

The choice between atomic microscopy types depend on the nature of controlled samples and the predominant forces between the tip and the sample.

The Magnetic Force Microscope (MFM) is a variation of the AFM. MFM has the same form of AFM microscopy, but the tip is coated with ferromagnetic deposit (FeNdB, CoPtCr, CoZrNb, Co or Ni). Magnetic force microscopy (MFM) has been widely discussed in literature [134, 135, 136] as it is one of the most used techniques for magnetic field mapping to measure weak forces. MFM leads to magnetic interactions between the tip and the stray filed emitted by the analyzed sample. MFM is used to study magnetic domains smaller than 100nm [137].

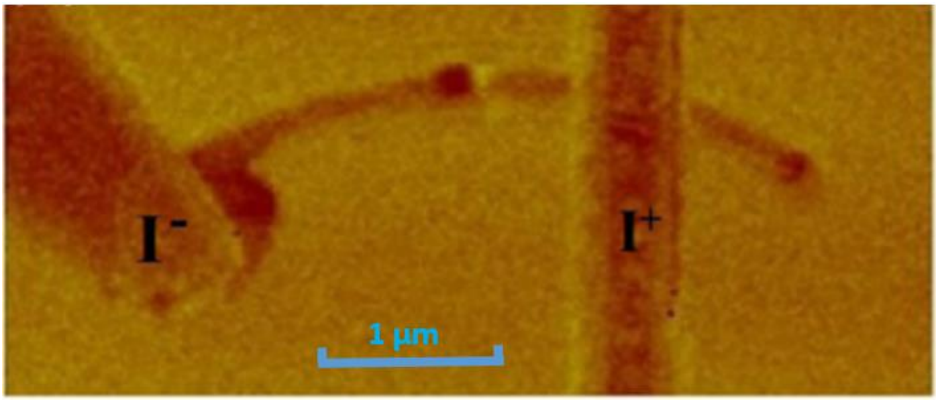

Figure 3.4- MFM images of Co sample with wire width 150 nm with gold electrodes on top, with I− and I+ indicating the direction of current flow [138]

One of MFM's disadvantage is the difficulty of extracting direct quantitative information from images as the signal is proportional to emitted field gradients and is strongly dependent on the magnetic tip properties. In addition, forces of the sample topology can interfere with magnetic force signals. In addition, the response frequency in MFM microscopy is limited by the mechanical resonant frequency of the force sensor [136, 139, 140].

3.4.3 Scanning magnetoresistance microscopy (SMRM)

MFM does not deduce the magnetic field value because it is difficult to analyze quantitatively the field detected by traditional MFM. The integration of self-sensing cantilevers based on Hall effect sensor, SQUID or magnetoresistive sensor (MR) in atomic force microscopes propose a solution to overcome these issues [141, 142, 143, 144]. Scanning magnetoresistance microscopy (SMRM) [145, 146] provides quantitative measurement with high spatial resolution of the magnetic fields emanating from sample surfaces. SMRM have been achieved micrometer and sub-micrometer resolutions on magnetic nanomaterials by attaching a commercial read and write head of conventional hard disk drives on a raster scanning setup [147].

Relatively, the local microscopy has short lateral scanning range (order of hundreds micrometers). The mechanical motors used in scanning magnetoresistance probe microscopy allows users to perform a fast, high resolution mapping of magnetic field. The magnetoresistance probe microscopy allows to overcome the limitations of short lateral scanning range of local microscopy. The scanning volume of this type of microscopy is more than ten centimeters to the detriment of sensor-to-sample distance controlled, so it is not able to precise exactly the sensor-to-sample distance [148].

3.4.4 Nitrogen Vacancy (NV) centers

Scanning probe microscopy using an artificial atom Nitrogen Vacancy (NV) situated in a diamond (Figure 3.5) is suitable for physics, chemistry, life sciences, earth and planetary sciences. The NV center has proved that it can be integrated in a local probe microscope for magnetic field imaging [149, 150]. Some of its key advantages are its high spatial resolution and high sensitivity to magnetic field. NV is a nitrogen-gap pair in a monocrystalline carbon. The photoluminescence emitted by the NV exhibits a

strong variation when it is excited by a resonant radio-frequency field. In the presence of magnetic field along the NV axis, the resonant frequency varies about 100 MHz per 10 Gauss (10 Oe). This variation is linear for fields up to 100 Gauss. These properties are known and are already used in several ways, but a true magnetic microscope using them did not exist yet [151]. This type of microscope is based on AFM microscope. A single diamond with a size of 20 nm is glued to AFM tips. The spatial resolution by this microscope is about 100 nm [151]. It allows quantitative and non-invasive measurements of a magnetic field at ambient conditions, by the calculation of shifted resonant frequency. The disadvantage of this microscope is that the calculation is non-direct. Furthermore, it is less efficient than the microscope based on magnetic sensors when dynamic pressure is applied.

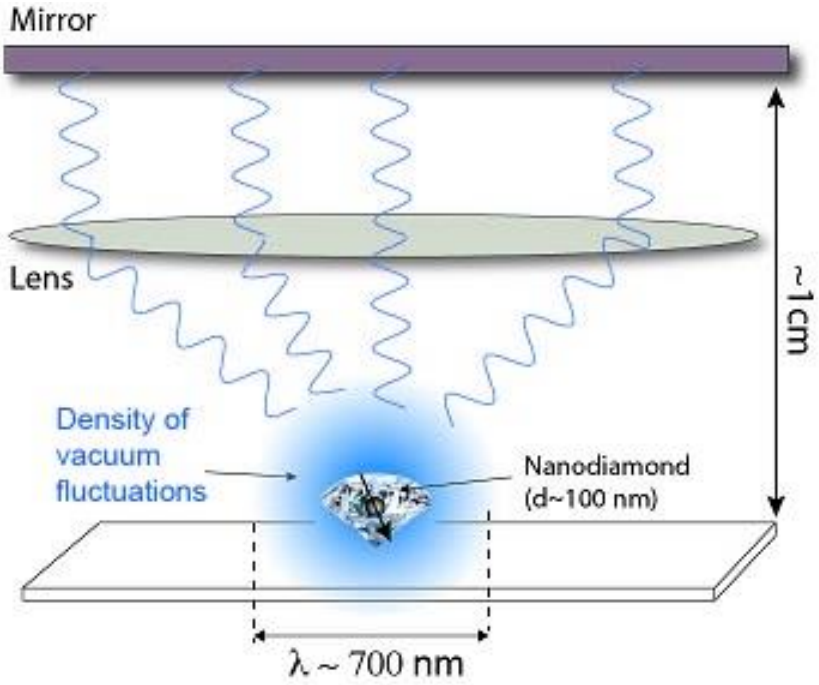

Figure 3.5- Example of NV-center Nanodiamond used for thermos dynamic application [152]

3.5 Optical Microscope

The first and most common microscope invented is the optical microscope, which uses light to pass through a sample to produce an image. The optical microscope is an optical instrument containing a system of lenses producing an enlarged image of a

sample placed in the focal plane. Optical microscopes have refractive glass (occasionally plastic or quartz), to focus light on the eye or onto another light detector. The spatial resolution limit of optical microscope is 250 nm [123]. Recently, CMOS or charge-coupled device (CCD) technology sensors similar to those used in a digital camera, are integrated to optical microscope to view directly the object through the eyepiece to obtain digital images. We present some types of optical microscopes for magnetic imaging like Magneto-optical devices based on Garnets films.

3.5.1 Magneto-optical devices based on garnets films

Past research has been devoted to exploiting magneto-optical properties of ferromagnetic material. Magneto Optical Imaging film (MO) determines locally and in real time the distribution of magnetic field. Magneto-optical (MO) effects result from the interaction of light with magnetic material. This interaction is undertaken to modify the polarization state of light. Magneto-optical devices have been conceived from garnet films due to their excellent MO properties (large Faraday effect), and used in a range of applications in nanophotonics, integrated optics, communications and imaging [153].

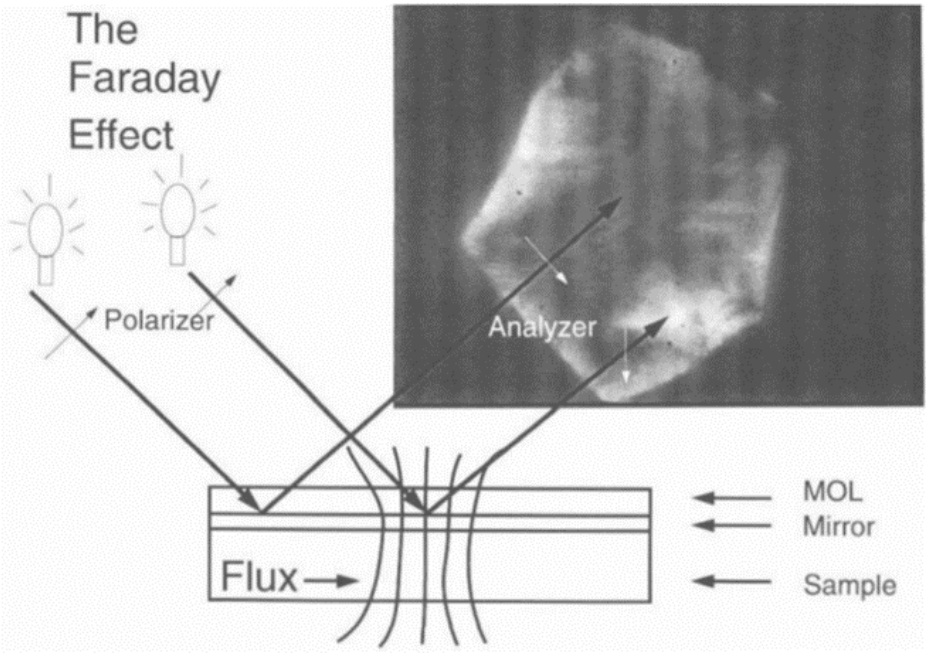

Figure 3.6- Schematic drawing of the Faraday effect. The sample is illuminated by linearly polarized light. Polarizer and analyzer are set in crossed position. The light enters the magneto-optically active layer (MOL) and is reflected at the mirror layer. In areas where no flux is present in the sample, no Faraday rotation takes place hence these regions stay dark in the image. In all areas where flux is present, the Faraday rotation changes the polarization plane so that this light is able to pass through the analyzer thus leading to bright

areas. In the drawing, a reflection angle is shown for clarity whereas in the experiment we have perpendicular incident light. [154]

The Kerr magneto-optic effect has been used to extract information of materials magnetization [155, 156]. The magneto- optic Kerr effect has been used to develop several scanning Kerr microscopies that have submicron spatial resolution [157]. Garnets are magnetic materials which present a strong Kerr effect more than scanning Kerr microscopies , and this why they are used (Figure 3.6). When crossing an optically active medium, the plane of polarization of light rotates under the action of external magnetic field (Figure 3.6). During a double crossing of the optical active medium (garnets) by the light, the magneto-optical effects are added. This property is exploited in MO imaging, which proceeds by the analyses of the light reflected by the garnet put in contact with the magnetic layer to be analyzed [158, 159]. If UV or blue range visible light sources are used, sub-micron spatial resolutions can be attained [160]. Figure 3.7 shows two examples of MO images.

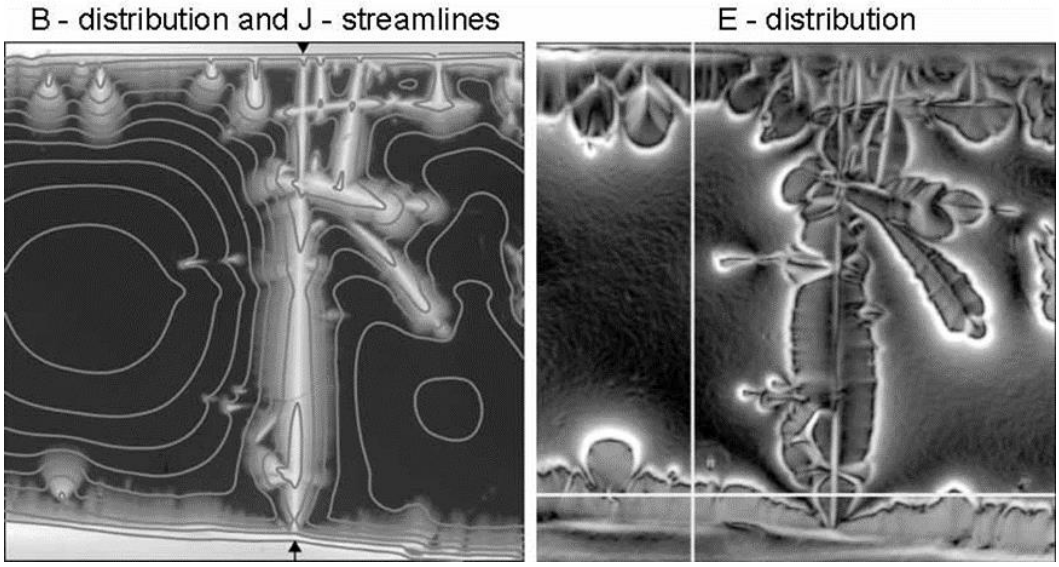

Figure 3.7- Magneto-optical images used to calculate distribution of electric field at 4.2 K in the superconductor. The image shows such distributions for a YBCO film with a grain boundary [161]

There are two main types of Faraday effect garnets used for MO imaging:

- Europium, EuS and EuSe garnets are used at low temperature ($T \leq 20K$) [162], and have a measuring range of several Teslas.
- YIG (Yttrium Iron Garnet) garnets have a strong Faraday rotation (3.8°/cm/kOe) and can be used at temperatures from 4 K to 300 K. On the other hand, the measuring range is only a few thousands Gauss.

Typical detectivity of a Garnet film is few µT.

3.6 Conclusion

Magnetic microscopies like MFM (Magnetic Force Microscopy), EFM (Electric Force Microscopy), and CFM (Chemical Force Microscopy) are local microscopies [163]. They have high spatial resolution (into nanometer range) and field sensitivity. In general, MFM does not deduce the magnetic field value because it is difficult to analyze quantitatively the field detected by traditional MFM. The integration of self-sensing cantilevers based on Hall effect sensor, SQUID or magnetoresistive sensor (MR) in atomic force microscopes propose a solution to overcome these issues.

The local microscopes mentioned above are used to scan small surface. The ability to detect and map the magnetic field at nanometer scale is essential in many areas of science. The disadvantage of MFM is the unsuitability of measuring samples for high magnetic fields with micrometric and millimeter surfaces. Many probes are developed to evaluate magnetic properties in large area of samples [164]. For example, the magnetic field microscopy of rock samples using giant magnetoresistance [73]. The 3D probes developed during the PhD (will be described in Chapter 4) aim to evaluate magnetic properties in large area of samples. The use of high sensitive sensors such as GMR sensors can improve the magnetic field sensitivity with high spatial resolution (into the micrometric range). The GMR sensor has a high field sensitivity for DC field detection without the need of any external bias magnetic fields, and ensures quantitative magnetic field measurements. GMR sensors can also be used in detecting of AC signals in wide frequency ranges up to a few GHz. The limitation is given by the ferromagnetic resonance of the free layer. 3D probes developed in this thesis has a spatial resolution compared to that of optical microscopy. In addition, this probe has more important measured magnetic range than the MO microscopes described above.

PART 2: 3D PROBE AND APPLICATIONS FIELDS

Chapter 4. 3D PROBE

4.1 Introduction

Many studies have already used the characteristics of magnetic sensors to improve the performance of scanning magnetic probes [34, 41, 165]. The majority of oldest probes are sensitive to two components of magnetic field at maximum. Oka et al. has introduced a 3D EC probe using 3-axis measurement with coils allowing to detect simultaneously three field components, however detection cannot be realized at the same measurement point [109]. The probes developed during this thesis allow to complete and to improve the results obtained through these previous works. In this chapter, we will demonstrate the viability of using four orientations of GMR sensors to develop a 3D probe allowing simultaneously reconstruction of three components of magnetic field at the same measurement point. Different types of GMR sensors have been used for the 3D probe developing. The first GMR sensor has sensitivity of 19 V/V/T and has a maximal working field up to ±15 Oe. The second type of GMR sensor has a larger magnetic range than the first one to the detriment of its sensitivity. This sensor has sensitivity of 3.5 V/V/T and it has a maximal working field of ±200 Oe (± 20 mT). These 3D probes are interesting for magnetic imaging of magnetic objects with arbitrary shapes, for evaluating of magnetic properties with micrometric spatial resolution and they are interesting to detect small variations of magnetic field caused by imperfections in the wires or magnetic materials. Also, eddy current excitation combined with our 3D receiver probe offers new advantages to characterize and detect the defects.

In this chapter, we will give the description of 3D probes. The reconstruction method of three components of magnetic field at the same measurement point will be also described in this chapter. We report in detail the characteristics of the GMR sensors used in developing of the 3D probes: stack, sensitivity, noise measurement and detectivity. We will start by the description of electronic circuit associated to the 3D probes for signals amplification.

4.2 Electronic Circuit

We have developed an electronic circuit composed of three parts described in Figure 4.1. This electronic circuit is based on a very low noise instrumentation preamplifier adapted to the resistance range of our GMR sensors, typically about 80 and 200 Ohms. The electronic circuit is used for each GMR sensor, thus we use four electronic circuits for each probe.

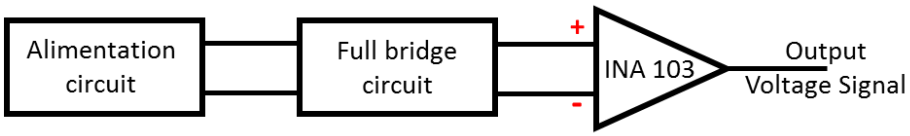

Figure 4.1-Electronic circuit

The first part is used to feed the circuit (Figure 4.2). To avoid electrostatic discharge, the power supply is not connected directly to the GMR. With 'V+' is DC voltage, the Regulator "1" fix the input voltage "V_{in}" to 9V. The Regulator "2" fix the input voltage to -9V.

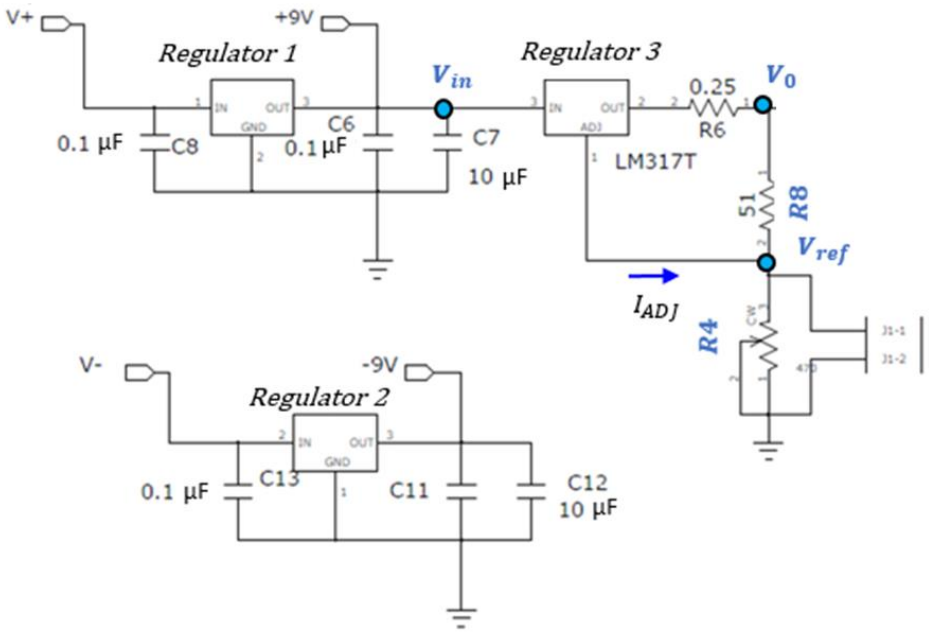

Figure 4.2 Alimentation part of electronic circuit. Regulators 1 and 2 ±9V are used for preamplifier INA103, regulator 3 is used for Wheatstone bridge

The output voltage V_0 at "Regulator 3" in Figure 4.2 is equal to:

$$V_0 = V_{ref}\left(1 + {}^{R4}/_{8}\right) + R4.I_{ADJ} \quad (4\text{-}1)$$

The Wheatstone bridge configuration in which the GMR sensor is inserted (Figure 4.3) is used to remove the DC component. The diodes are used for circuit protection, by diverting the discharge current into circuit supply circuit [166]. We relied two diodes in parallel to GMR (each one has inversed orientation of the other). Thus, the lower resistance of diode allows better power dissipation. We choose the value of R2 = R3 ≥ 10 × R_{GMR}, to ensure that the current is the same in both branches of the bridge. The voltage at GMR sensor V_{GMR} is equal to:

$$V_{GMR} = \frac{V_0.R_{GMR}}{R_{GMR}+R3} \quad (4\text{-}2)$$

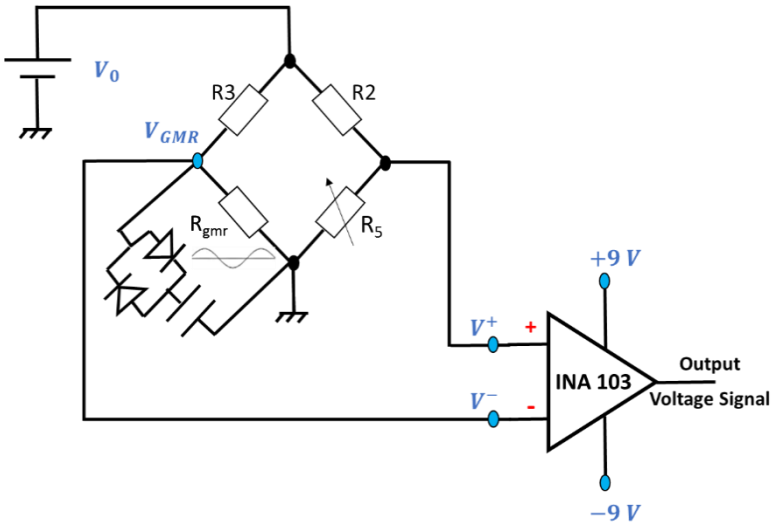

Figure 4.3- Full Wheatstone bridge circuit relied to INA103

The full bridge is associated with low noise preamplifier "INA 103" to increase the gain of useful signal. The INA 103 is fed by the out of regulators "1 and 2" (± 9 V). The noise of "INA 103" is of 1.2 $nT/\sqrt{Hz}$ for a gain of 500. The output voltage signal V_{out} is equal to :

$$V_{GMR} = G_{INA103}.(V^+ - V^-) \quad (4\text{-}3)$$

With G_{INA103} is the INA103 gain.

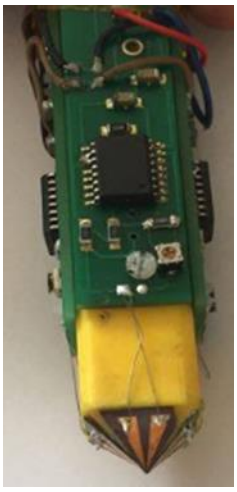

Figure 4.4- 3D probe with electronic circuits

4.3 Experimental set-up

4.3.1 Experimental set-up for DC signal

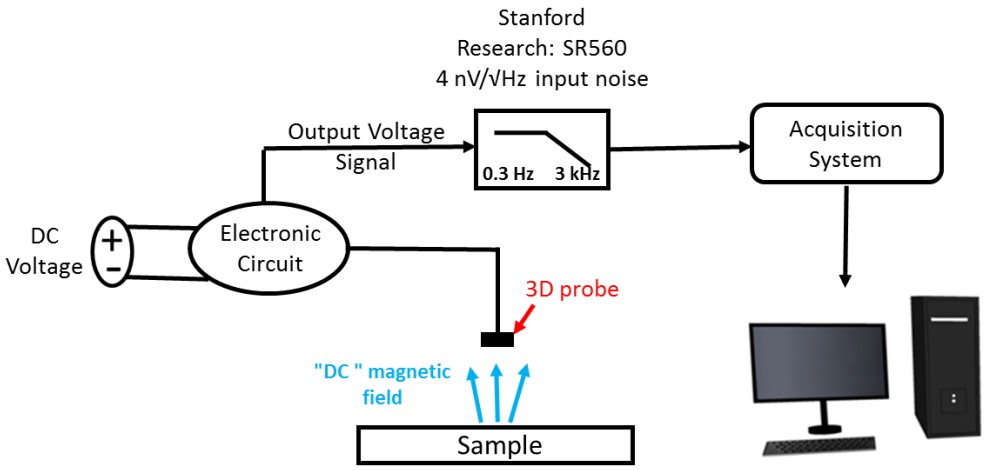

Figure 4.5- Experimental set-up for DC signal.

Experimental set-up consists of test desk, where the sample can be moved horizontally along the X and Y directions. The distance between sensor and sample is set by moving the sensor vertically down until contact. The output voltage of the preamplifier is connected to a commercial voltage amplifier. This low noise amplifier has 4 nV/√Hz input noise, 1 MHz bandwidth and variable gain from 1 to 50,000 with filters used to reduce the noise intensity. For DC signal measurement, we use low-pass filter (LPF) at 30 Hz to avoid 50 Hz electrical network perturbations. We use a typical additional gain of 20, resulting in a total chain gain of 10000. The results are displayed

on a PC using an acquisition system (Figure 4.5). Noise measurements have been realized with full experimental set-up, no parasitic noise has been identified.

4.3.2 Experimental set-up for AC signal

The experimental set-up used for AC signal measurement (Figure 4.6), is comparable to the experimental chain used for DC signal measurement. We add a frequency generator to excite the emitter and the output signal is demodulated by a SR830 DSP Lock-In Amplifier that simultaneously displays the magnitude and phase of a signal. A Mux (multiplexer) is used to select the signals received by the sensors. SR830 uses digital signal processing (DSP) to replace the demodulators, output filters and amplifiers found in conventional lock-in and has a noise about 6 nV/√Hz.

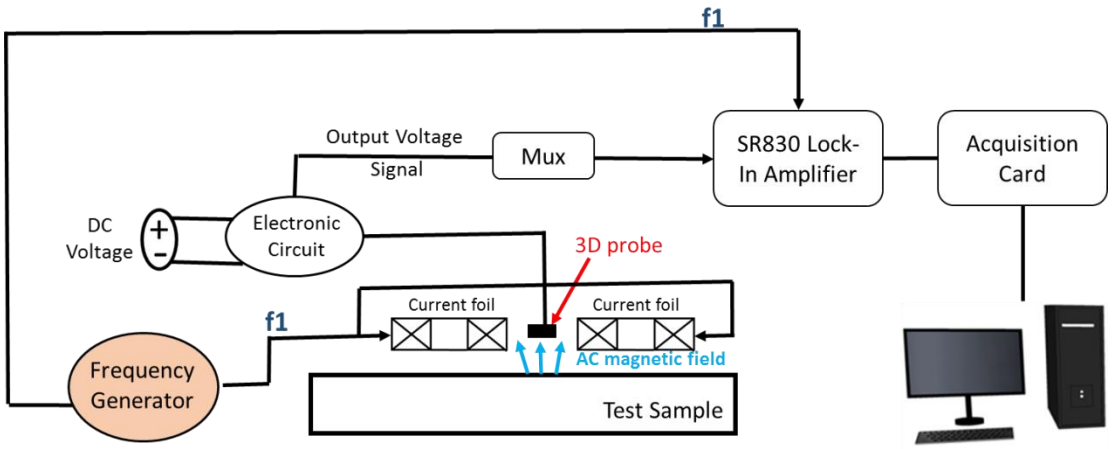

Figure 4.6- Experimental set-up for AC signal.

4.4 Description of 3D probe formed by four GMR

Figure 4.7 shows the details of three axis probe based on GMR sensors. Four GMR sensors are fixed on mechanical support in order to reconstruct the three components of magnetic field. Each of these sensors is oriented at 45° one in front of another. The support has been fabricated by 3D printer by Gerald Le Goff.

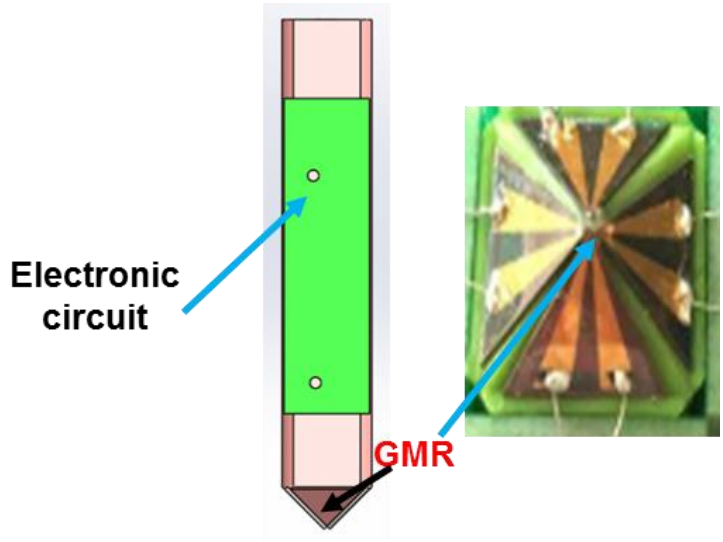

*Figure 4.7- Description of the probe **(left part)**, Right: GMR sensors **(right part)***

Exploiting the signals received from each sensor of the probe and the sensitivity matrix of these sensors, we can reconstruct the three components of the field.

GMR sensors C1 and C2 are mainly sensitive in 'x-z' plan, and the sensors C3 and C4 are mainly sensitive in 'y-z' plan (Figure 4.8). This sensors conception will be used to reconstruct the three components of magnetic field.

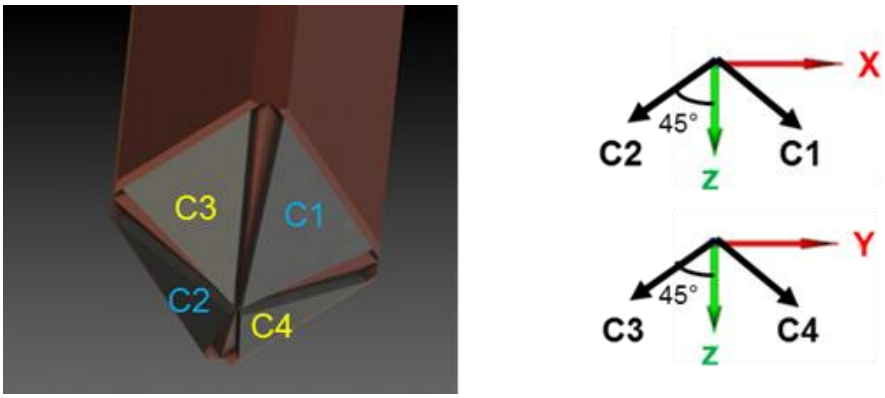

Figure 4.8- GMR sensors position in three axis

First step is to calculate the sensitivity of each sensor in three axis in order to create the sensitivity matrix (S_{ij} is the absolute value of sensitivity of 'i'sensor according to direction 'j'). For applied voltage V=1V to each GMR sensor, sensitivity matrix S (V/V/T) is:

$$S = \begin{pmatrix} S_{1x} & S_{1y} & S_{1z} \\ S_{2x} & S_{1y} & S_{2z} \\ S_{3x} & S_{3y} & S_{3z} \\ S_{4x} & S_{4y} & S_{4z} \end{pmatrix} \quad (4\text{-}4)$$

Each sensor has a sensitivity in two axis, with sensitivity theoretically equal to zero in third axis (Figure 4.8). So S becomes

$$S = \begin{pmatrix} S_{1x} & 0 & S_{1z} \\ S_{2x} & 0 & S_{2z} \\ 0 & S_{3y} & S_{3z} \\ 0 & S_{4y} & S_{4z} \end{pmatrix} \quad (4\text{-}5)$$

Figure 4.9 shows the distribution design of GMR sensors according to x-z plane and to y-z plane.

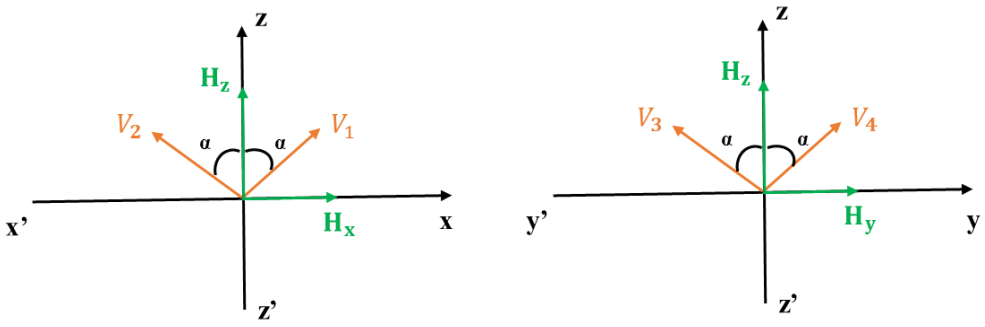

*Figure 4.9- Distribution design of GMR sensors according to x-z plane **(left part)** and to y-z plane **(right part)***

V_i represents the output signal amplitude acquired by the sensor 'i'. H_j is the magnetic field component according to the direction 'j' and $\alpha = 45°$.

As $V_i = S_{ij}.H$, we conclude the following numerical formulas:

$$V_1 = S_{1x}\,.\,H_X.sin(\alpha) + S_{1z}.\,H_Z\,.\cos(\alpha) \quad (4\text{-}6)$$

$$V_2 = -S_{2x}\,.\,H_X.sin(\alpha) + S_{2z}.\,H_Z\,.\cos(\alpha) \quad (4\text{-}7)$$

$$V_3 = -S_{3y}\,.\,H_y.sin(\alpha) + S_{3z}.\,H_Z\,.\cos(\alpha) \quad (4\text{-}8)$$

$$V_4 = S_{4y}\,.\,H_y.sin(\alpha) + S_{4z}.\,H_Z\,.\cos(\alpha) \quad (4\text{-}9)$$

With $\alpha = 45°$, $\cos(45°) = sin(45°) = \frac{1}{\sqrt{2}}$, the equations presented above allow to obtain the following matrix representation:

$$\begin{pmatrix} V_1 \\ V_2 \\ V_3 \\ V_4 \end{pmatrix} = \frac{1}{\sqrt{2}} \begin{pmatrix} S_{1x} & 0 & S_{1z} \\ -S_{2x} & 0 & S_{2z} \\ 0 & -S_{3y} & S_{3z} \\ 0 & S_{4y} & S_{4z} \end{pmatrix} \begin{pmatrix} H_X \\ H_Y \\ H_Z \end{pmatrix} \quad (4\text{-}10)$$

$$V = Se \,.\, H \quad (4\text{-}11)$$

So the matrix 'H' that contains the three components of magnetic field is equal to:

$$H = \; Se^{-1}.V \quad (4\text{-}12)$$

4.5 GMR sensors used for 3D probe development

Developed probe is based on giant magnetoresistance (GMR) sensor operating at room temperature. The GMR sensors used in this work are spin valves with length of 30 µm and width of 3 µm. The GMR of spin valve type is formed of three layers: free layer, spacer, pinned layer (hard layer). The three layers are deposited according to the scheme of Figure 4.12 and Figure 4.19. It has high sensitivity and is effective for small object detection due to its micron size.

GMR sensors used in PhD thesis have yoke shape (Figure 4.10). This form is interesting for magnetic noise suppression and domain walls elimination [6]. Magnetic domains are generally responsible of 1/f noise increasing and of the presence of RTN; also, they affect high-frequency noise near the resonance frequency.

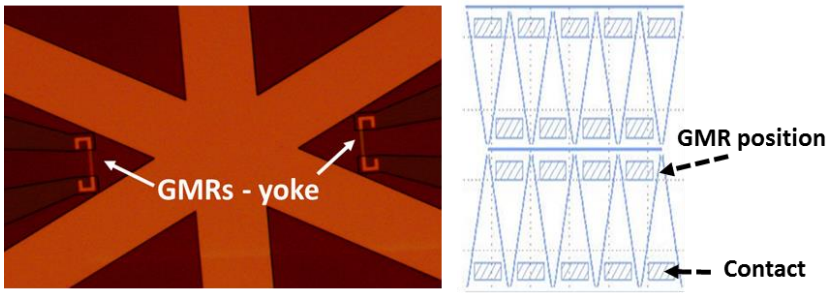

Figure 4.10- GMR sensor in a yoke-shape before cutting

Magnetic instabilities are moved to the corners of yoke shape, thus, the magnetization field is aligned without instability at the long part of free layer. Simulation of magnetic moment distributions is shown in Figure 4.11 [13].

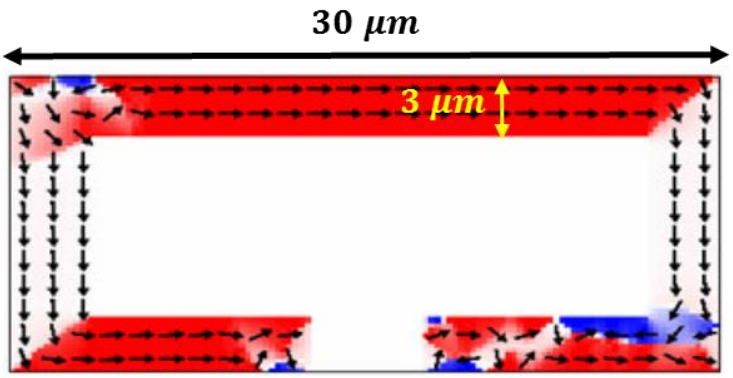

Figure 4.11- Distribution of magnetic moments in free layer with a yoke shape structure.

The GMR has been fabricated by standard UV lithography technics, means ion bean etching, deposition by sputtering of Ta/Cu/Ta contacts and lift off. The full structure is then covered by 200 nm Al2O3 passivation/protective layer. Elodie Paul has performed the process.

We will present below the types of GMR sensors used in 3D probe.

4.5.1 Type 1 GMR sensors

One of the 3D probes developed in the PhD uses four type 1 GMR sensors. It is patterned in a stack of the following composition:

Ru(3)/Ta(3)/PtMn(18)/CoFe(2)/Ru(0.85)/CoFe(2.1)/Cu(2.3))/CoFe(1.5)/Ta(0.1)/NiFe(3.5)/Ta(3). The thicknesses are in nanometers. The role of the Ta layer is to decouple the crystallinity of the CoFe layer and the NiFe layer.

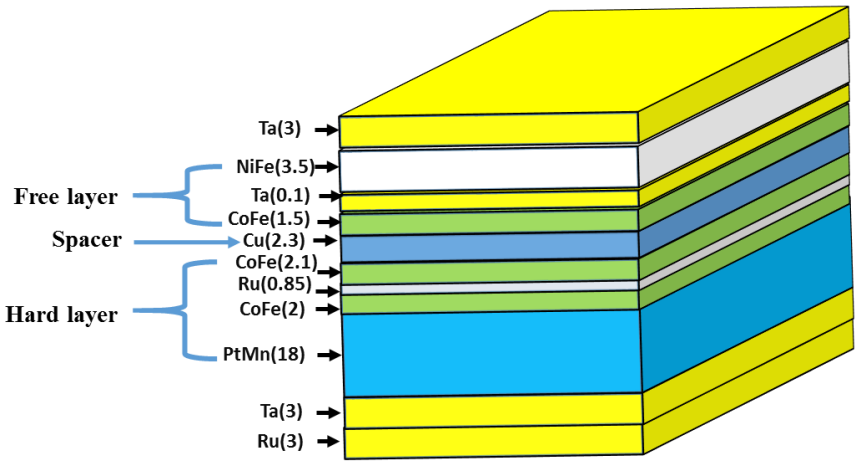

Figure 4.12- Spin valve stack of type1 GMR sensors. The thicknesses (X) are given in nm

GMR's hard layer (reference layer) is composed of PtMn/CoFe/Ru/CoFe, where PtMn is anti-ferromagnetic coupled by exchange bias to the CoFe - ferromagnetic layer [167]. Ruthenium (Ru) is chosen with optimized thickness to create an anti-ferromagnetic coupling between the two CoFe ferromagnetic layers, based on theory of RKKY interaction [168, 169]. This structure is call a synthetic antiferromagnetic. The main advantage of CoFe/Ru/CoFe coupling is the cancelation of static field created by the hard layer on the free layer in microscopic structures. The free layer is an association of CoFe with a soft ferromagnet NiFe having a magnetization which rotates easily with an external applied field. The spacer (Cu) is a nonmagnetic layer of copper. The spacer makes the free and the hard layers magnetically independent. Tantalum constitutes the cap layer and the seed layer when it is respectively on the top and the bottom of the GMR.

Sensitivity

The resistance of type 1 GMR sensors used in 3D probe is about 180 Ohms. We put the GMR sensors in the Helmholtz coils to obtain the sensitivity curve according to the three axis. The applied voltage to each GMR sensor is 0.35 V.

The response of GMR sensors to magnetic field collinear (according to z-axis) with the pinned layer magnetized orthogonally to the reference layer orientation is shown in Figure 4.13.

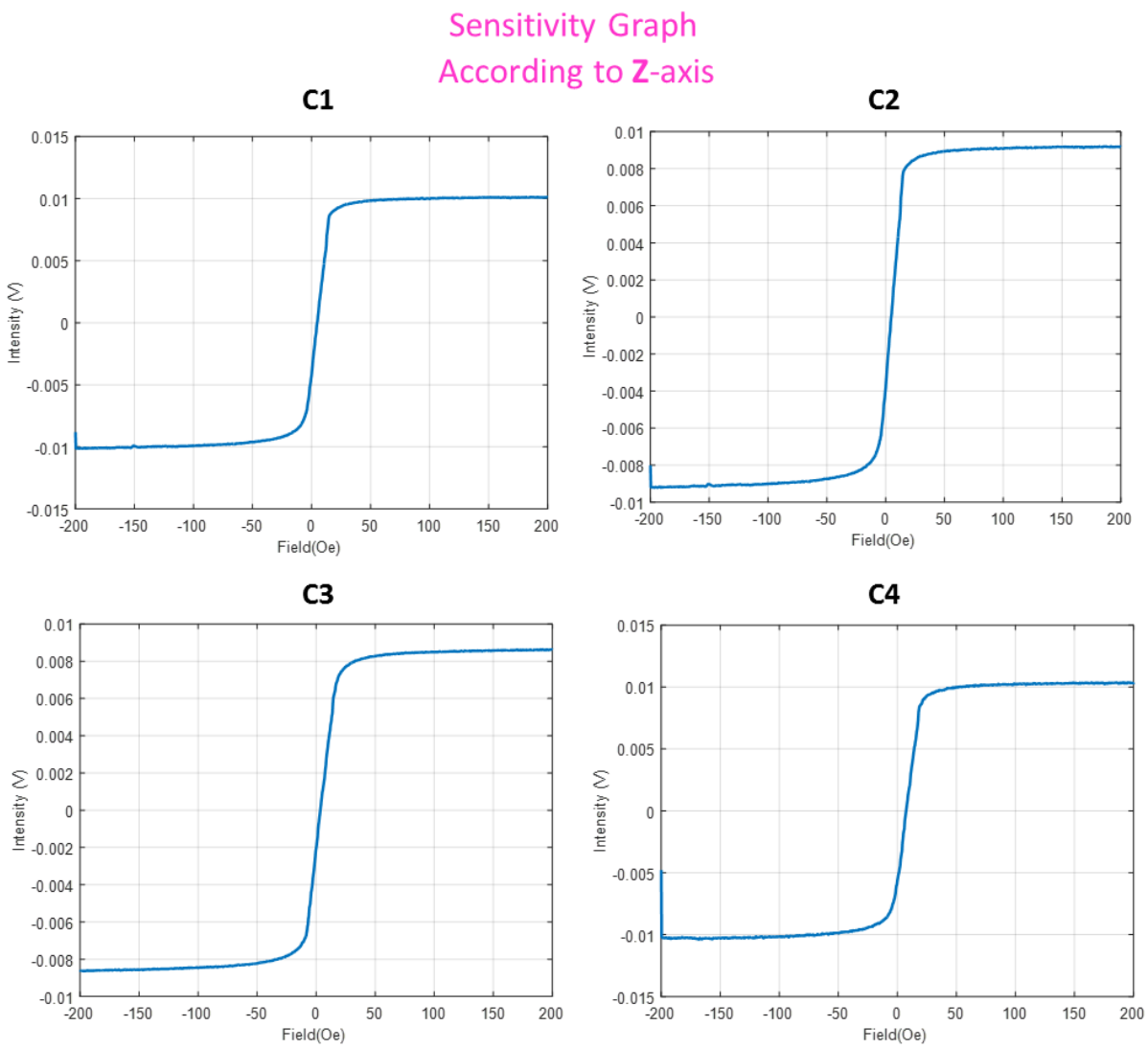

Figure 4.13 – The response of four type 1 GMR sensors as function of magnetic field applied along their z-axis

Figure 4.13 shows that the four GMR sensors are sensitive to magnetic field according to z-axis. Also, we show that the slope (that equal to the sensitivity) of the four GMR responses according to z-axis is positive and has the same sign (in agreement with theoretical results presented in paragraph 4.4).

The response of GMR sensors to magnetic field collinear (according to y-axis) with the pinned layer is shown in Figure 4.14.

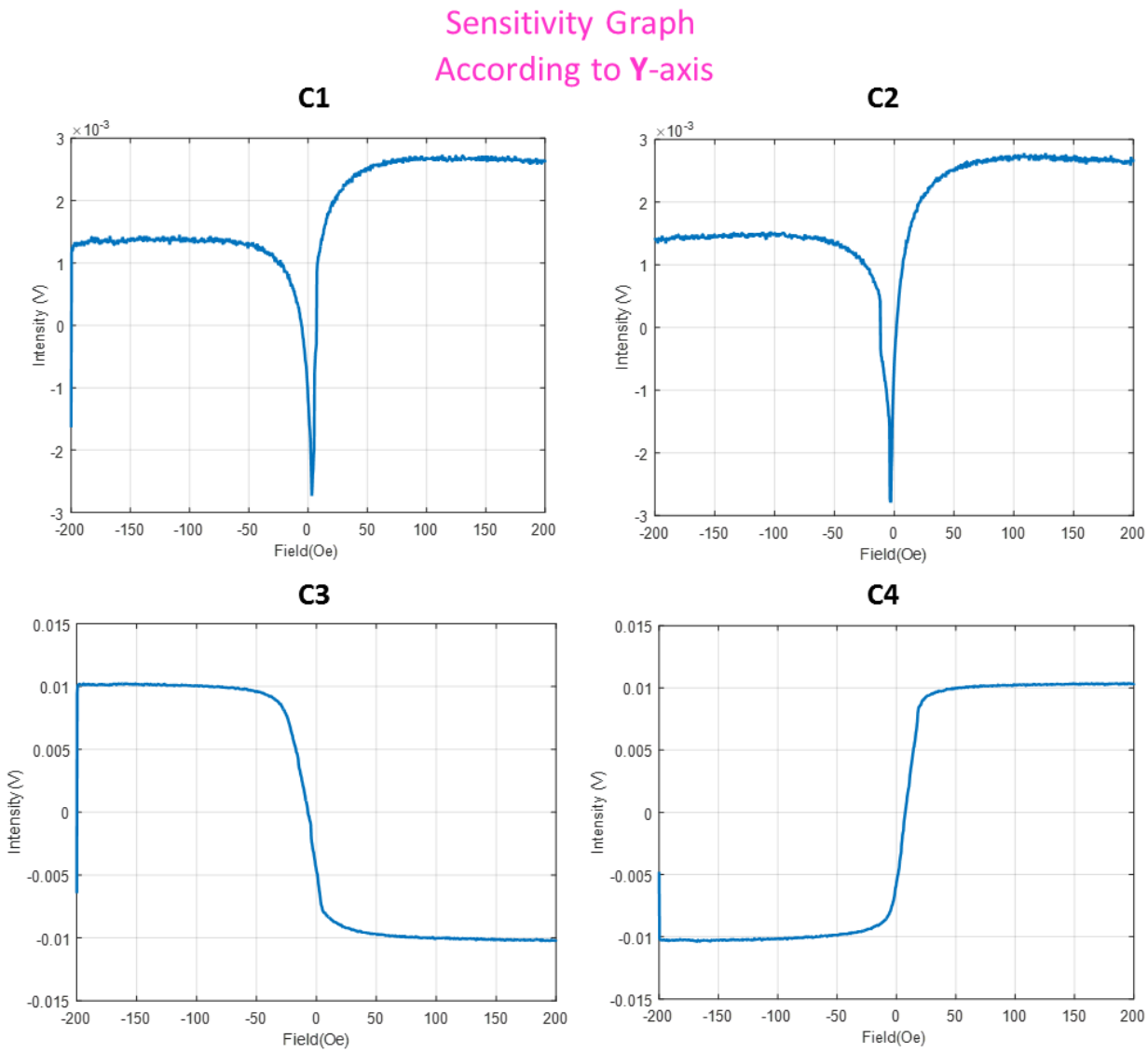

Figure 4.14- The response of four type 1 GMR sensors as function of magnetic field applied along their y-axis.

Figure 4.14 shows that the GMR sensors C3 and C4 are sensitive to magnetic field according to y-axis and that the GMR sensors C1 and C2 are less sensitive to y magnetic field component. However, the response of C1 and C2 is not negligible, typically 1/6 of the response along the normal axis and hence, the sensitivity matrix has to integrate that response. Also, we show that the slope of C3 response according to y-axis is negative, and the slope of C4 response according to y-axis is positive (in agreement with theoretical results presented in paragraph 4.4).

The response of GMR sensors to magnetic field collinear (according to x-axis) with the pinned layer is shown in Figure 4.15.

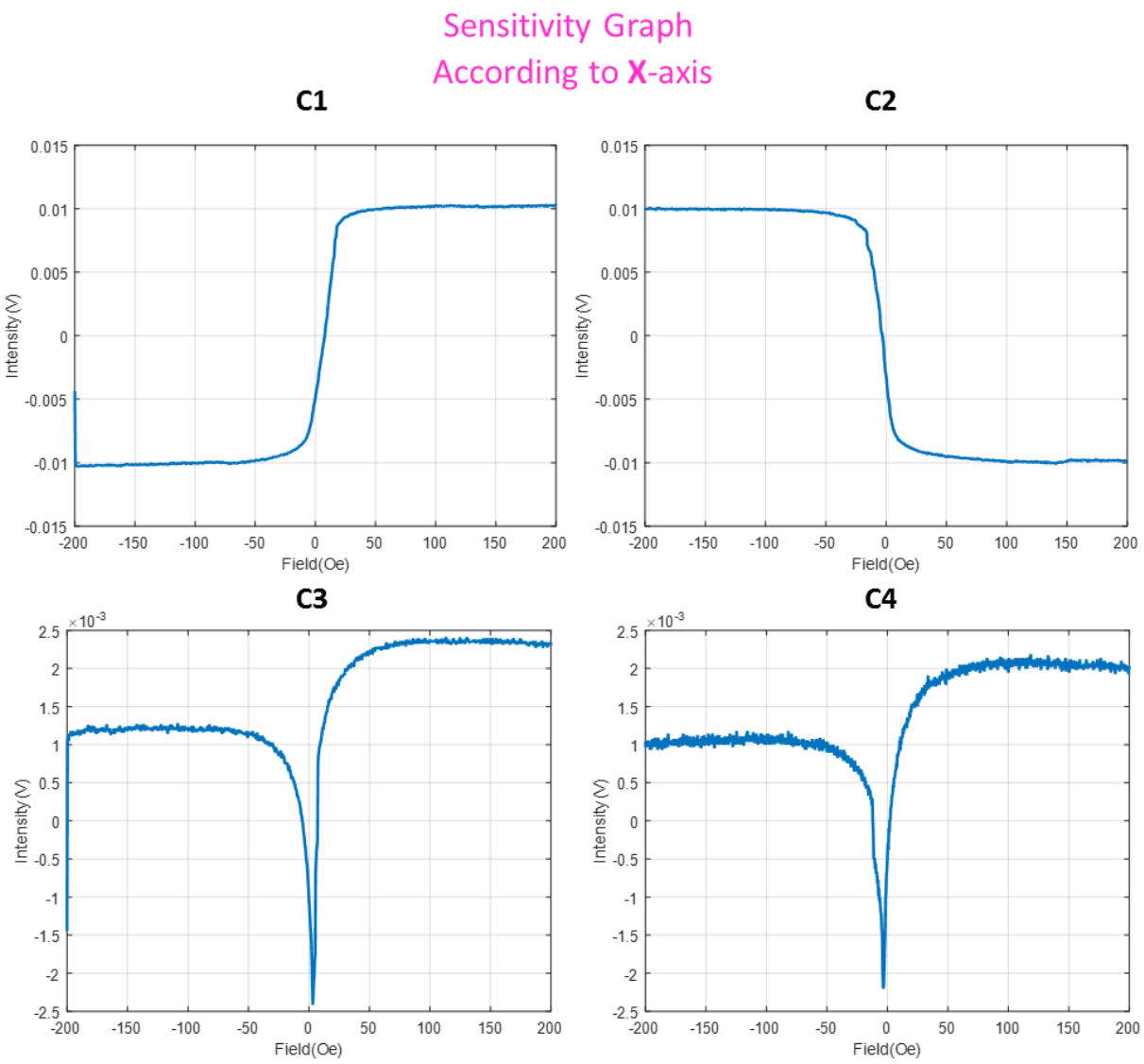

Figure 4.15- The response of four type 1 GMR sensors as function of magnetic field applied along its x-axis.

Figure 4.15 shows that the GMR sensors C1 and C2 are sensitive to magnetic field according to x-axis and that the GMR sensors C3 and C4 are less sensitive to x magnetic field component. Also we show that the slope of C2 response according to x-axis is negative, and the slope of C1 response according to x-axis is positive (in agreement with theoretically results presented in paragraph 4.4).

Figure 4.13, Figure 4.14 and Figure 4.15 show that type 1 GMR sensors can measure field intensities between ± 15 Oe. We should be able to measure a larger range with a well centered response of the curve. The small offset of the field is due to a residual

ferromagnetic coupling between the free layer and the hard layer. Beyond this maximum field, the sensor response becomes nonlinear. These experimental sensitivity results of the 3D probe based on type 1 GMR sensors constitute a validation of theoretical results presented in paragraph 4.4.

Finally, the sensitivity matrix Se (V/V/T) of the 3D probe based on type 1 GMR sensors is:

$$Se = \begin{pmatrix} 17.5 & 2.4 & 18.7 \\ -17.1 & 2.3 & 18.2 \\ 2.1 & -16.8 & 18.1 \\ 1.9 & 17.2 & 18.7 \end{pmatrix}$$

The sensitivity matrix Se in (%/mT) is:

$$Se = \begin{pmatrix} 1.75 & 0.24 & 1.87 \\ -1.71 & 0.23 & 1.82 \\ 0.21 & -1.68 & 1.81 \\ 0.19 & 1.72 & 1.87 \end{pmatrix}$$

Low frequency noise

Despite that the yoke structure stabilizes magnetically the free layer of GMR, there may stay magnetic domains in the free layer, probably caused by the quality of the lithography. Figure 4.16 shows the voltage noise (voltage fluctuations) of four type 1 sensors in a time interval. This figure shows the proportional relation between the level of the noise and the V_{GMR}.

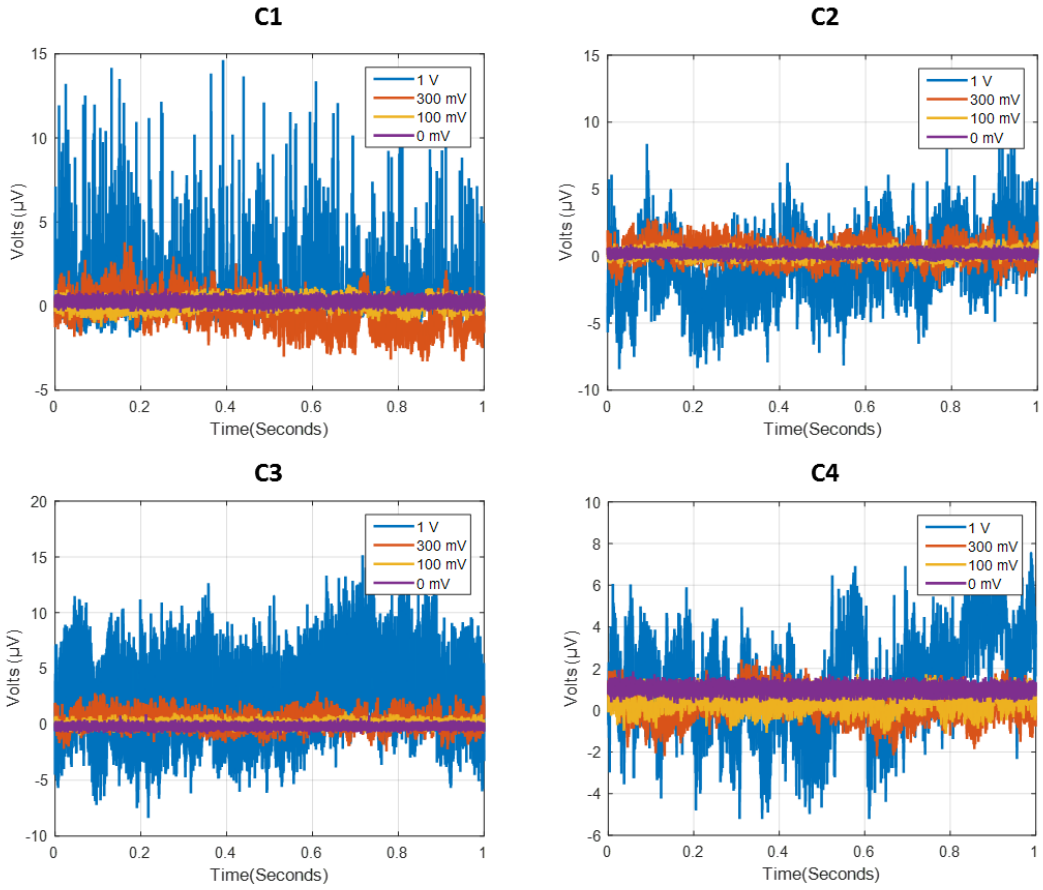

Figure 4.16- Voltage noise of four type 1 sensors with V_{GMR} = 0 mV, 100 mV, 300 mV and 1V

In time domain, we clearly see to states of the sensors. At low voltage typically 300mV, sensors are exhibiting a 1/f noise whereas at large voltage, they exhibit an additional random telegraph noise. This is confirmed by the spectral analysis of the noise of each sensor.

Noise spectral density and detectivity

The detectivity is the magnetic field level detected by the sensor with SNR equal to one and for frequency band of 1 Hz. As C1 and C2 are sensitive in x-z plane, the detectivity of these sensors according to y-axis is approximately equal to zero. It is equal to zero according to x-axis in the case of C3 and C4 sensors. We will show the noise level of four type 1 sensors.

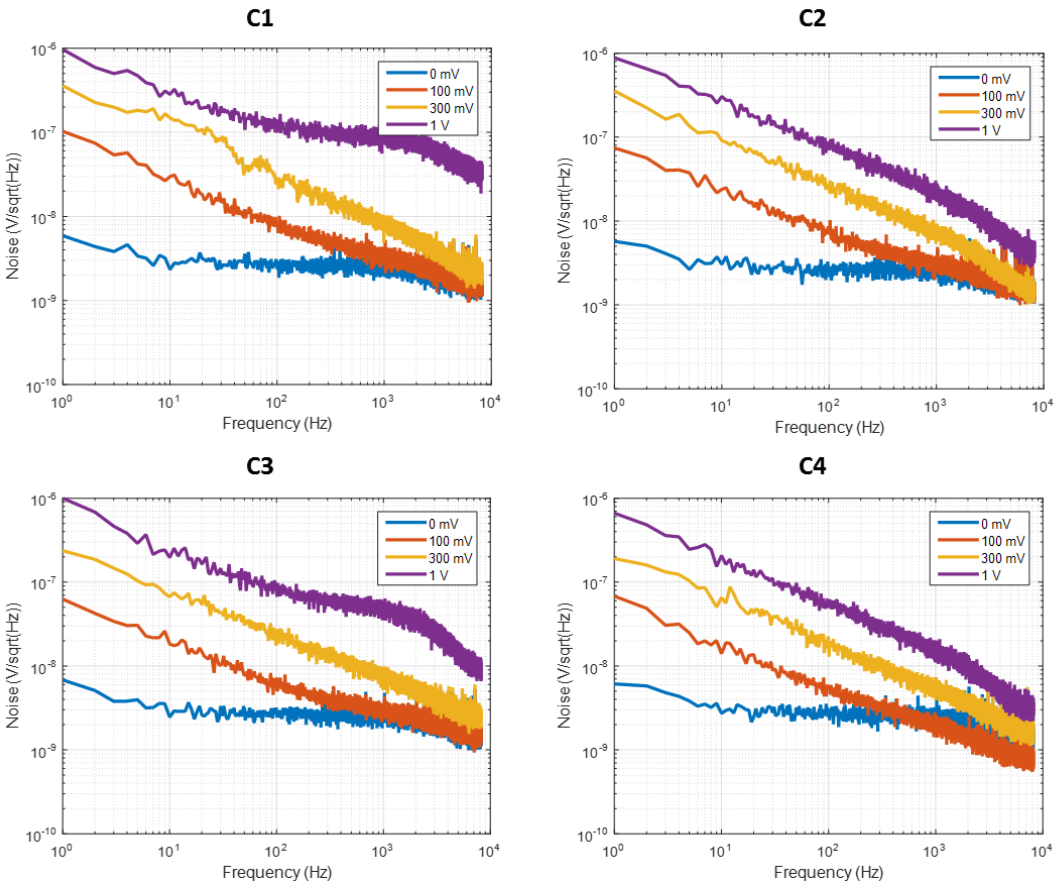

Figure 4.17-Noise spectral density in V/√Hz of four type 1 sensors with V_{GMR}= 0 mV, 100 mV, 300 mV and 1V. Due to the appearance of RTN noise, the maximum voltage to be used for these sensors is below 1V.

Spectral density measurements confirm first analysis. Up to 300 mV, we have a 1/f noise with a cutoff at several kHz, which is usual for the size of GMR. At 1 V, C2 and C4 are exhibiting also a classical 1/f noise up to 10kHz. The drop at 3 kHz is due to the low pass filtering of the noise measurement setup. C1 and C3 are exhibiting a bump followed by a $1/f^2$ decrease which is typical of a RTN noise with a characteristic frequency of few kHz. This RTN has a magnetic origin and it disappears when the GMR is saturated. Figure 4.19 shows the detectivity or field equivalent noise $T/\sqrt{Hz}$ of four type 1 sensors calculate as $Noise\ (\frac{V}{\sqrt{Hz}})/S\ (\frac{V}{T})$.

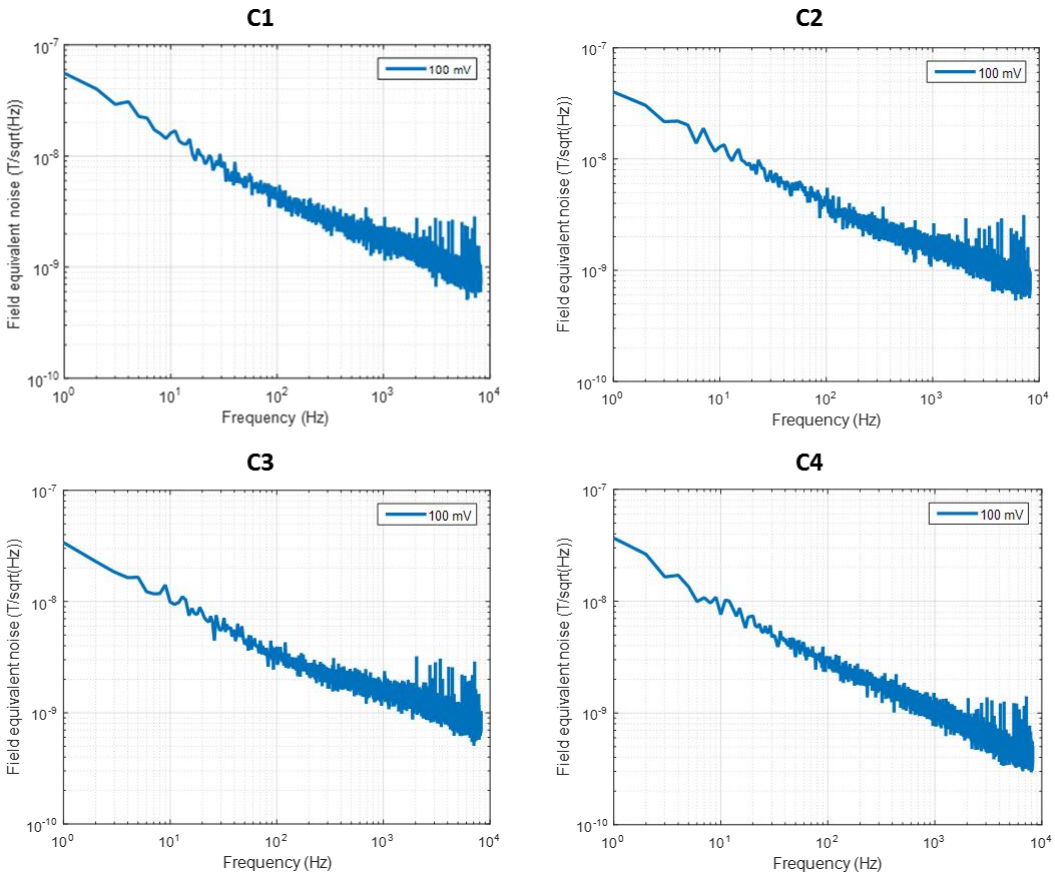

Figure 4.18-Field equivalent noise in T/√Hz of fourtype 1 sensors according to z-axis with V_{GMR}= 100 mV

Table 4 resumes the detectivity ($nT/\sqrt{Hz}$) value of type 1 sensors according to its sensitive axis at different frequencies with D_{ij} - detectivity of 'i' sensor according to direction 'j'.

	f = 10 Hz	f = 100 Hz	f = 1 kHz
D_{1x}	17	4.5	1.6
D_{1z}	16	4	1.5
D_{2x}	13	4.4	1.9
D_{2z}	12	4	1.7
D_{3y}	10	4.3	1.7
D_{3z}	9	3.9	1.5
D_{4y}	8	3.4	1.2
D_{4z}	7.5	3.1	1.1

Table 4- Detectivity given in ($nT/\sqrt{Hz}$) of type 1sensors according their sensitive axis with V_{GMR}= 0.1V

For magnetic imaging, we are working at low frequency. For NDT, we work typically between 1 kHz and several MHz depending on the application and hence it is interesting to increase strongly the voltage on the GMRs.

4.5.2 Type 2 GMR sensors

The other 3D probes developed in the PhD thesis are based on four type 2 GMR sensors. They are patterned in a stack of the following composition:

Si/SiO2(500)/Ru(1)/PtMn(15)/CoFe(2)/Ru(2)/NiFe(4.5)/CoFe(1)/Cu(2.3)/CoFe(2)/Ru (0.85)/CoFe(2.1)/PtMn(18)/CoFe(2)/Ru(0.85)/CoFe(2.1)/Cu(2.3)/CoFe(1)/NiFe(4.5)/ Ru(1.8)/CoFe(2)/PtMn(15)/Ta(5). The thicknesses are in nanometers.

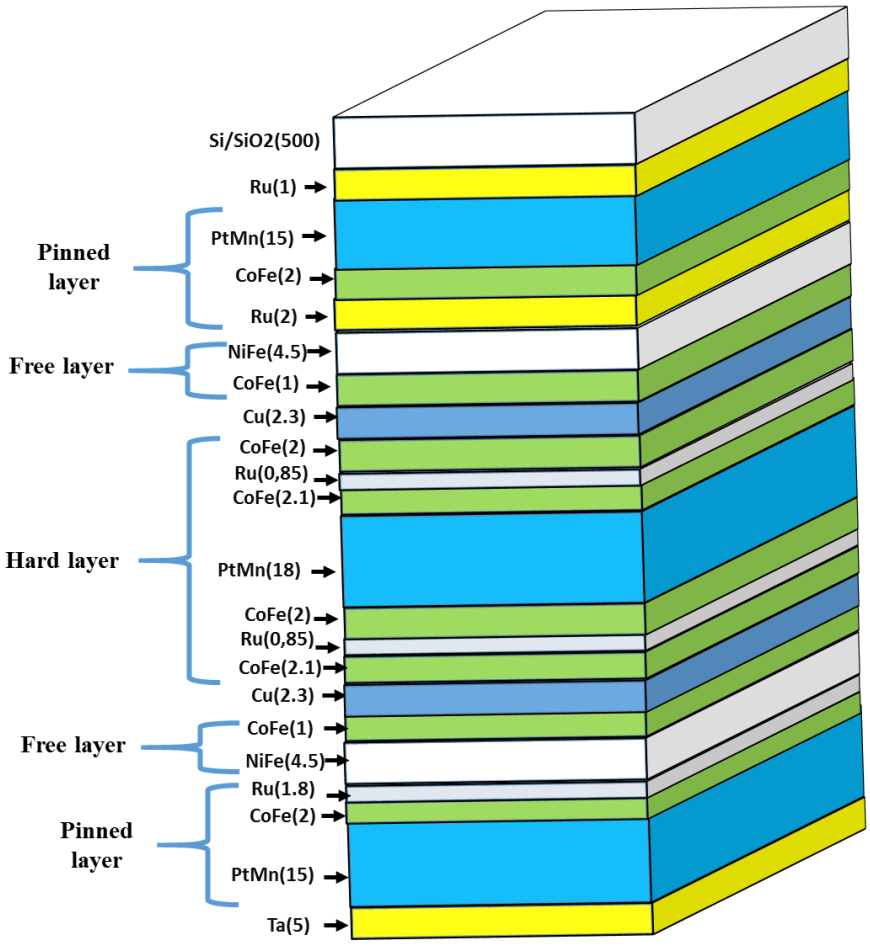

Figure 4.19- Spin valve stack of type 2 GMR sensors. The thicknesses (X) are given in nm

GMR's hard layer (reference layer) is again composed of antiferromagnetic- synthetic antiferromagnetic CoFe/Ru/CoFe/PtMn/CoFe/Ru/CoFe structure. The spacer (Cu) is a

nonmagnetic layer of copper. The free layer is an association of CoFe with a soft ferromagnet NiFe. This stack is more sophisticated. First additional exchange biased CoFe/PtMn orientated at 90° from the reference layer are added. These pinned layers are weakly coupled to the free layer by a RKKY coupling. The effect is to force the free layer to be oriented in a specific direction at zero field to destroy the hysteresis and to insure a linear response on a controlled field region. The second change is to create a dual GMR in parallel with shared reference layer. The first free layer (top) is ferromagnetically coupled to the pinning layer whereas the second free layer (bottom) is antiferromagnetically coupled to its pinned layer. This stack insures a wide linear range and a symmetric response. In order to achieve the proper orientation, the stack is annealed at 300°C with 3 different fields orientation, one at 1T and the second about 50mT.

Sensitivity

The resistance of type 2 sensors used in 3D probe is about 80 Ohms. The applied voltage to each GMR sensor is 0.17 V.

The response of GMR sensors to magnetic field collinear (according to z-axis) with the pinned layer is shown in Figure 4.20.

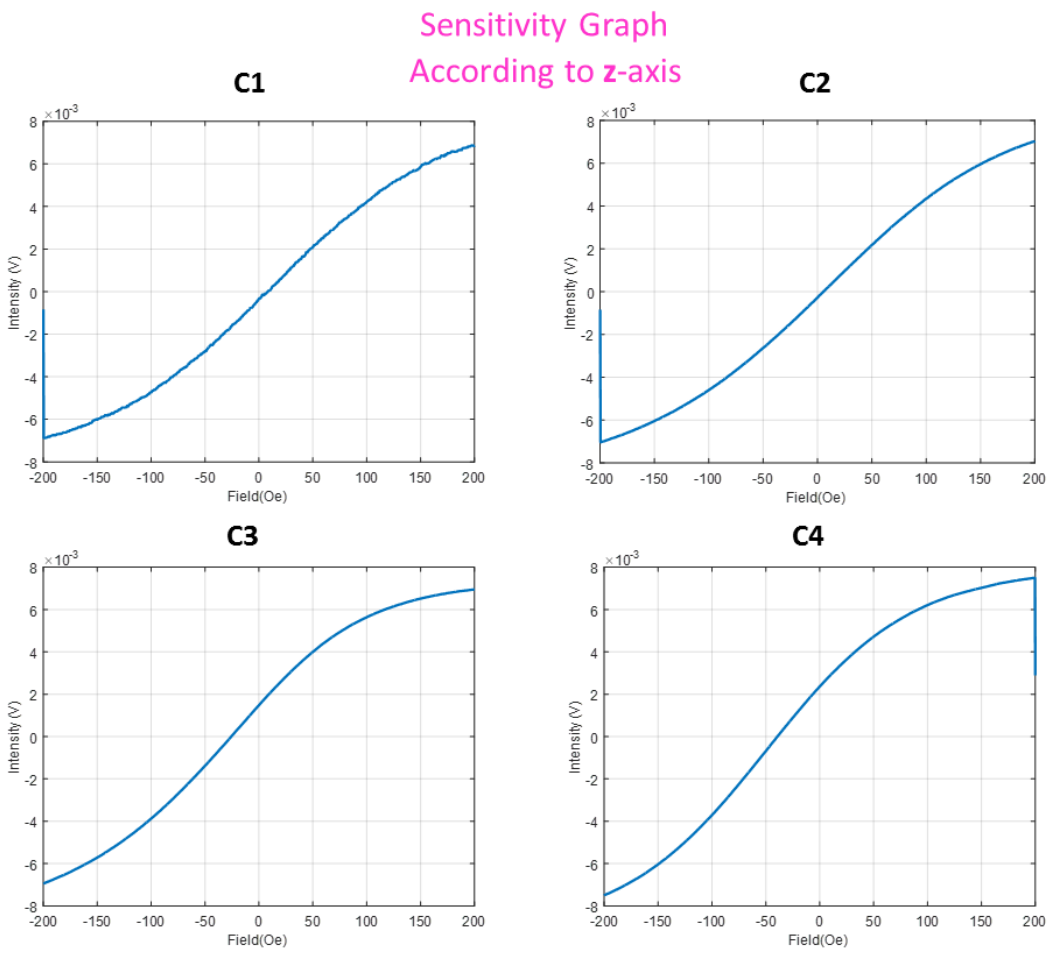

Figure 4.20 – The response of four type 2 GMR sensors as function of magnetic field applied along its z-axis

Figure 4.20 attests that the four GMR sensors are sensitive to magnetic field according to z-axis. Also we show that the slope of the four GMR responses according to z-axis is positive (in agreement with theoretical results presented in paragraph 4.4). For an unexplained reason, C3 and C4 are presenting a magnetic offset, which is not present in the full sheet measurements. It is probably due to lithography process issue.

The response of GMR sensors to magnetic field collinear (according to y-axis) with the pinned layer is shown in Figure 4.21

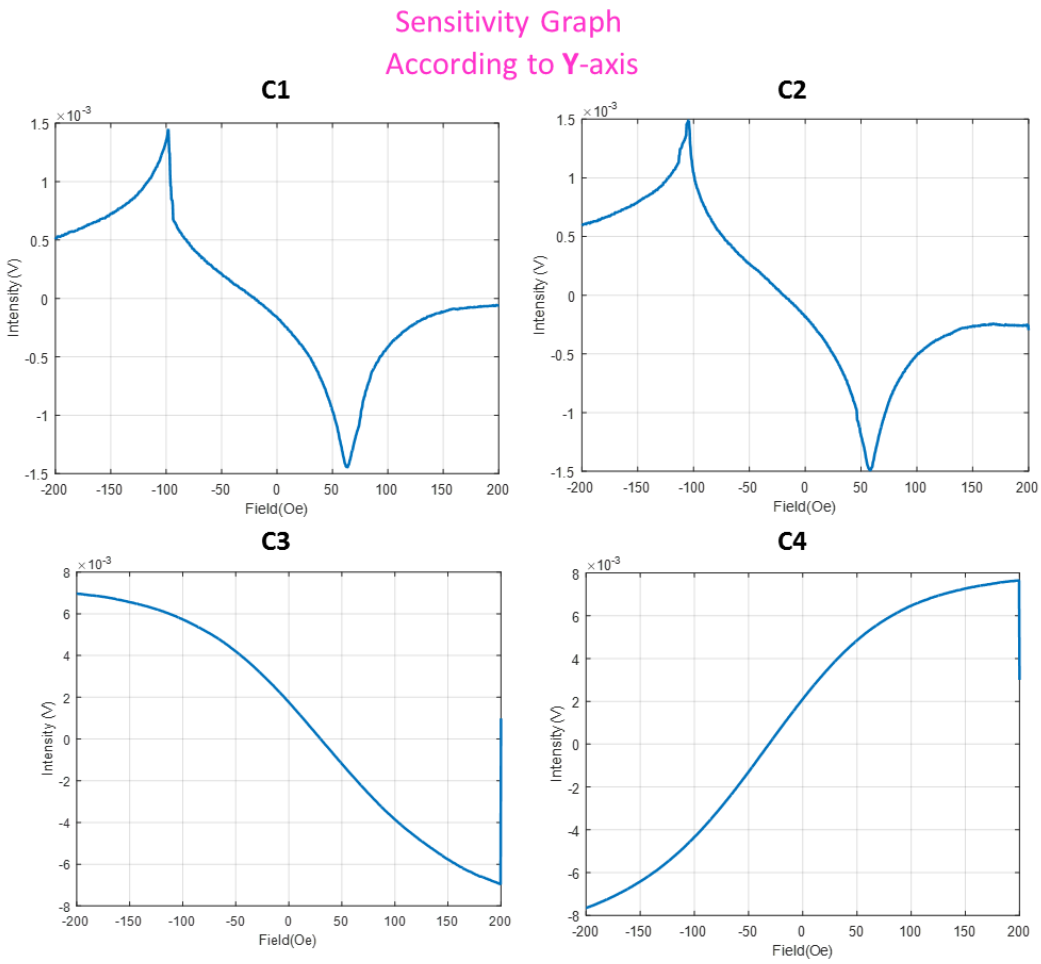

Figure 4.21- The response of four type 2 GMR sensors as function of magnetic field applied along its y-axis

Figure 4.21 shows that the GMR sensors C3 and C4 are sensitive to magnetic field according to y-axis and that the GMR sensors C1 and C2 are not sensitive to y magnetic field component. Also we show that the slope of C3 response according to y-axis is negative, and the slope of C4 response according to y-axis is positive (in agreement with theoretically results presented in paragraph 4.4). In the case of the response of C1 and C2 sensors, the two peaks showed are due to the presence of two pinned layers with opposite couplings. We can see that the response to a field in a direction perpendicular to the normal response is non-negligible and has to be included in the sensitivity matrix. Another information can be obtained from these curves. The coupling between the pinned layer and free layers is 7 mT for the ferromagnetic coupling and 11 mT for the AF coupling. A fine tuning of the Ru layer is hence necessary to obtain a better symmetry.

The response of GMR sensors to magnetic field collinear (according to x-axis) with the pinned layer is shown in Figure 4.22.

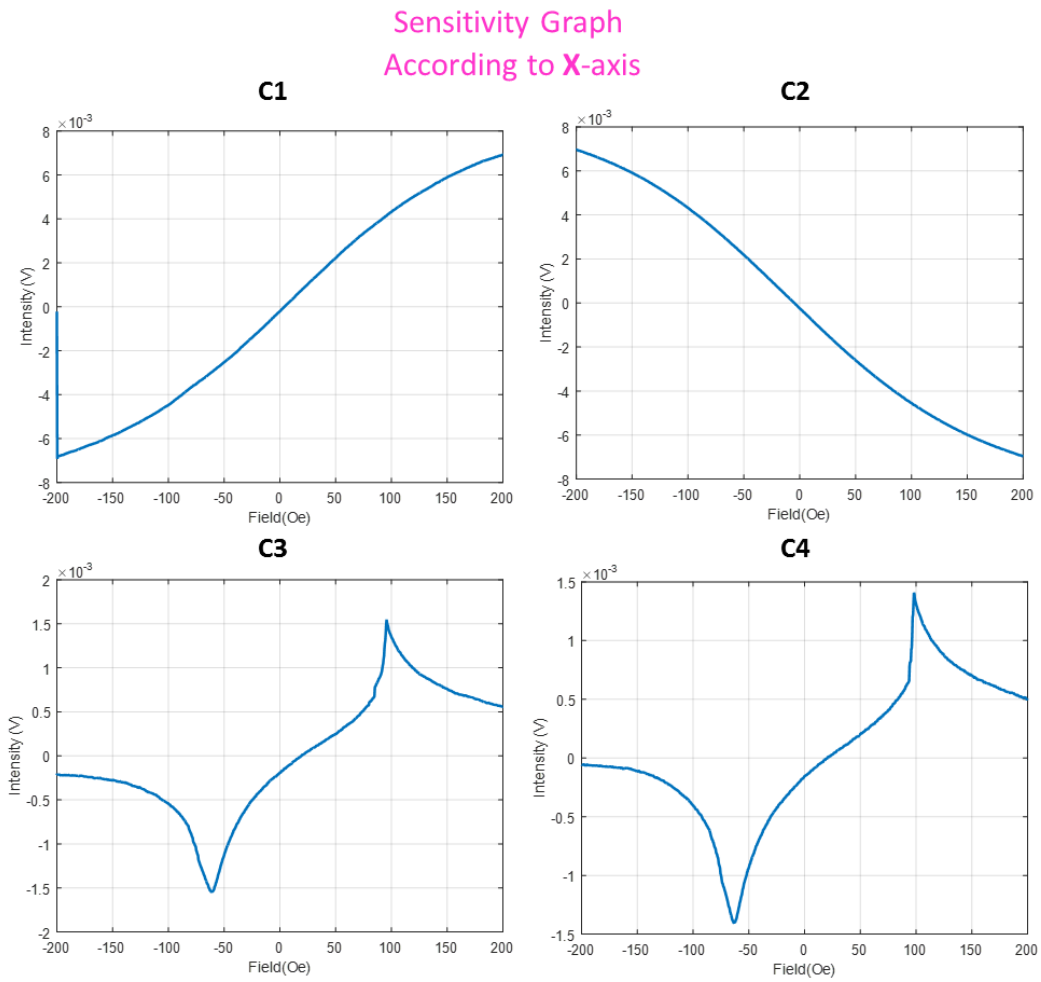

Figure 4.22- The response of four type 2 GMR sensors as function of magnetic field applied along its x-axis

Figure 4.22 shows that the GMR sensors C1 and C2 are sensitive to magnetic field according to x-axis and that the GMR sensors C3 and C4 are not sensitive to x magnetic field component. Also, we show that the slope of C2 response according to x-axis is negative, and the slope of C1 response according to x-axis is positive (in agreement with theoretically results presented in paragraph 4.4). In the case of the response of C3 and C4 sensors, the two peaks are also due to the presence of two pinned layers.

Figure 4.20, Figure 4.21 and Figure 4.22 show that the type 2 GMR sensor can measure field intensities up to ±20 mT. Beyond this maximum field, the sensor response becomes nonlinear.

Finally, the sensitivity matrix Se (V/V/T) of the 3D probe based on type 2 GMR sensors is:

$$Se = \begin{pmatrix} 2.72 & -0.42 & 2.82 \\ -2.72 & -0.38 & 2.80 \\ 0.44 & -3.06 & 3.12 \\ 0.37 & 3.36 & 3.15 \end{pmatrix}$$

The sensitivity matrix Se in (%/mT) at 0 external field is:

$$Se = \begin{pmatrix} 0.27 & -0.042 & 0.28 \\ -0.27 & -0.038 & 0.28 \\ 0.044 & -0.31 & 0.31 \\ 0.037 & 0.34 & 0.32 \end{pmatrix}$$

Low frequency noise

Figure 4.23 shows the low frequency noise (voltage fluctuations) of four type 2 sensors in a time interval of one second. We see that the noise level of the type 2 sensors is lower than the type 1 sensors. In particular, we do not see RTN noise which can be explained by the strength of the pinning layer and thus to magnetic domain fluctuation stabilizations.

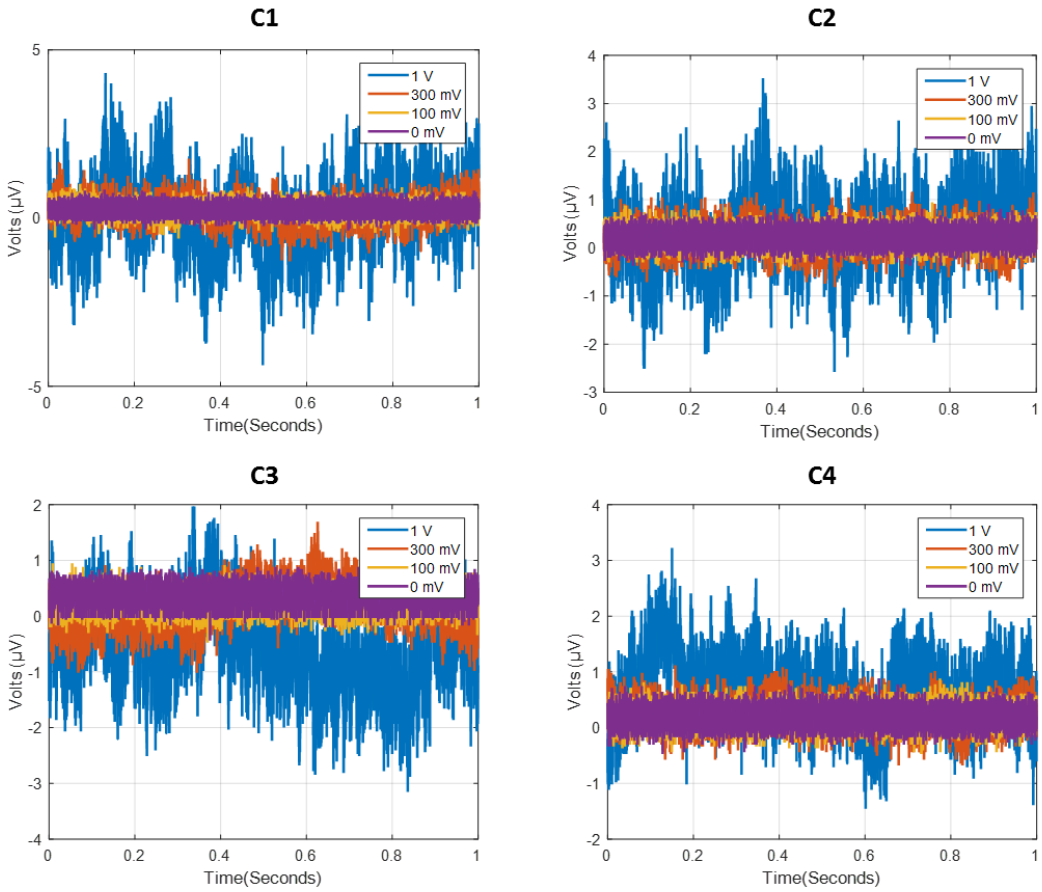

Figure 4.23- Low frequency noise in μV of four type 2 sensors with V_{GMR}= 0 mV, 100 mV, 300 mV and 1V

Detectivity

We will show the noise level of four type 2 sensors.

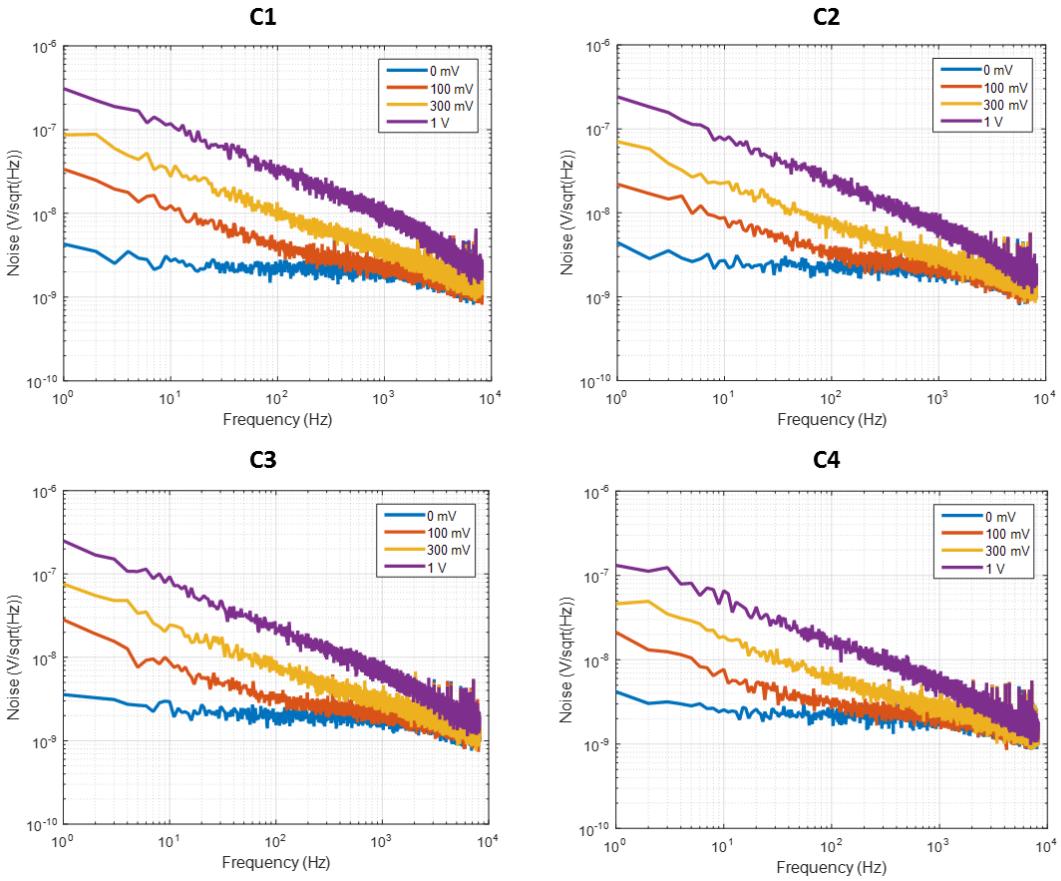

Figure 4.24- Noise spectral density in V/√Hz of four type 2 sensors with V_{GMR}= 0 mV, 100 mV, 300 mV and 1V

Figure 4.25 shows the field equivalent noise in $T/\sqrt{Hz}$ of four type 2 sensors.

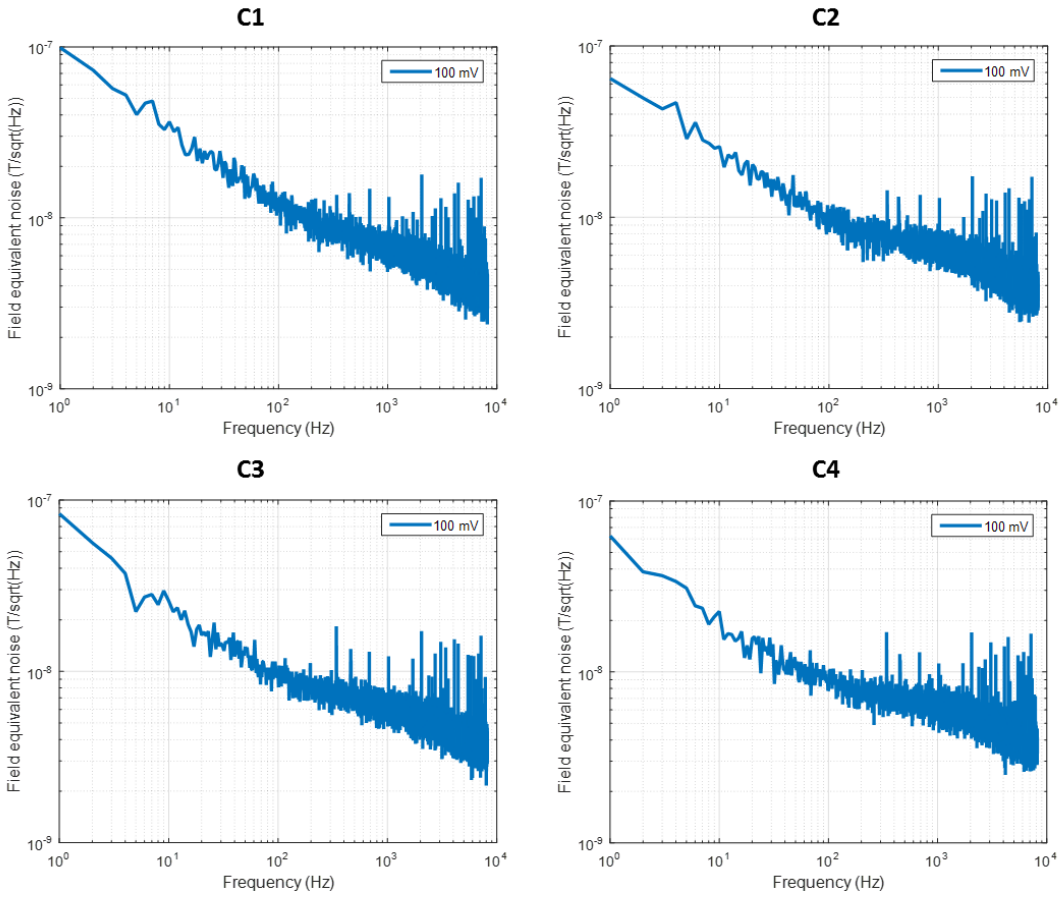

Figure 4.25- Noise spectral density in T/√Hz of four type 2 sensors according to z-axis with V_{GMR} = 100 mV

Table 5 resumes the detectivity ($nT/\sqrt{Hz}$) value of type 2 sensors according to their sensitive axis at different frequency with D_{ij} is the detectivity of 'i' sensor according to direction 'j'.

	f = 10 Hz	f = 100 Hz	f = 1 kHz
D_{1x}	40	14	7
D_{1z}	36	13	6
D_{2x}	29	12	5.5
D_{2z}	25	10	4.7
D_{3y}	29	10	6.7
D_{3z}	25	9	6
D_{4y}	26	7.4	6.4
D_{4z}	22	7.8	5

Table 5- Detectivity given in (nT/$\sqrt{Hz}$) of type 2 sensors according to its sensitive axis with V_{GMR} = 0.1 V

In terms of detectivity type 2 probe is only a factor of 2 worse at low frequency than type 1 probes but allows a factor 10 in terms of field range. At high frequencies, in the thermal noise the type 1 probe becomes better than type 2 and ultimately we find a ratio of detectivity related to the ratio of sensitivity as expected. Hence, we will prefer to use type 1 for NDT of small defects in the MHz range whereas type 2 can be interesting for low frequency measurements.

More generally, we can optimize the coupling of the pinned layers of type 2 configuration to increase the sensitivity and decrease the linear range for each specific application.

4.6 Conclusion

By using a single GMR sensor, if we want to measure all three components of the field, we have to take a measurement three times for three different probe-sample relative orientations. This method increases the error of results to be analyzed. In this chapter we have presented 3D probes allowing to extract the three spatial components of the magnetic field at the same point of measurement and simultaneously. We have exploited the small size and the high sensitivity of GMR sensors in the development of 3D probe. In the following chapters, we will see the advantages of 3D probes based on different types of GMR sensors for magnetic imaging and NDT.

Chapter 5. 3D PROBE IN MAGNETIC IMAGING

5.1 Introduction

This chapter reports on the results obtained by the 3D probe described in Chapter 4. We have demonstrated the viability of using four orientations of GMR sensors allowing the reconstruction of three components of magnetic field for 3D magnetic imaging. In particular, the probe is useful for magnetic imaging of magnetic objects with arbitrary shapes. This is due to the detection of small variations of magnetic fields due to the imperfections in the wires or magnetic materials as well as evaluating magnetic properties with micrometric spatial resolution. We will see in this chapter that the 3D probes allow the reconstruction of three components of DC magnetic field emitted by current line, dollar bin and soft steel objet. Also we will show the performances of 3D probe for susceptibility measurement (AC magnetic signals). For the detection of magnetic footprint of different shape objects in soft steel mock-up, we have used a GMR sensor able to detect strong magnetic fields. For that we will use the 3D probes based on type 2 sensors. Other measurements have been performed with type 1 probes. We will start by the description of measurement set-up.

5.2 Set-ups

Two different setups have been used for magnetic imaging. The first one installed at LIST. This setup has been used in particular for current line imaging (Figure 5.1). This experimental set-up consists of test desk controlled by a motor, where the probe can be moved horizontally along the X and Y directions. The motor has spatial resolution of 0.2 µm in z-plane and 5 µm in x-y plane. The mapping system is controlled by an extremely easy-to-use-software built on MS Windows platform and LabVIEW. The 3D probe associated to a mechanical support is connected to a voltage preamplifier and acquisition system to display the results.

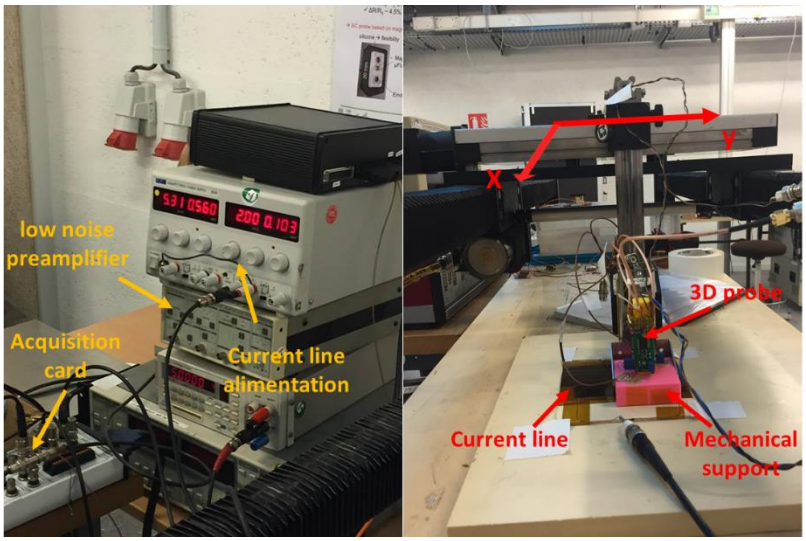

Figure 5.1- Experimental set-up at CEA-LIST

A second setup at SPEC has been used for dollar bin, soft steel material and susceptibility measurements (Figure 5.2). This experimental set-up consists of test desk controlled by a motor, where the sample can be moved horizontally along the X and Y directions. The motor has spatial resolution of 0.2 µm in z-plane and 2 µm in x-y plane. The 3D probe is connected to a voltage preamplifier and acquisition system to display the results. For susceptibility measurement (AC signal), we have adjusted the coil to emit a magnetic field by using a frequency generator to feed this coil, "SR830 DSP Lock-In Amplifier", and a Mux.

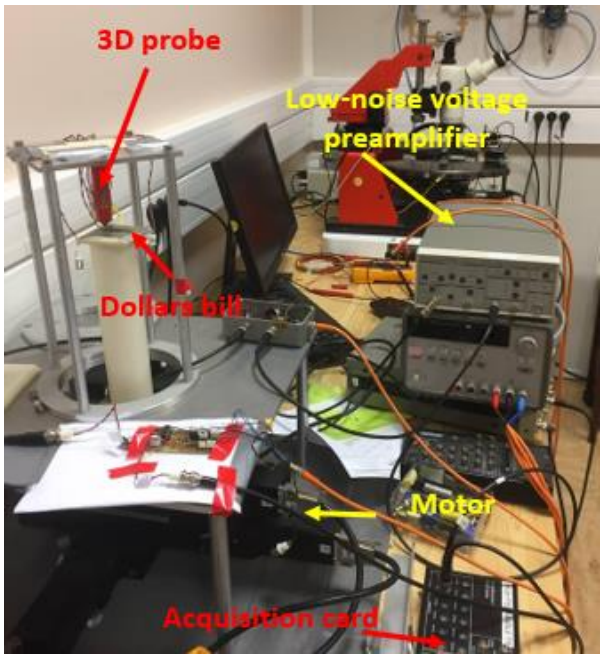

Figure 5.2- Experimental set-up at CEA-SPEC

5.3 Study of current line

The current line has been studied with the probe based on type 2 GMR sensors. The sensor-to-sample distance (lift-off) during scanning operation is 0.7 mm. The scanning step is 0.1 mm for the x-axis and 0.6 mm for the y-axis. Current line is excited by a DC current of 20 mA (Figure 5.3). The straight wire consists of 1 mm thick line with a length of 15 mm. The current flow is parallel to the Y-axis and the scan direction is perpendicular to the current flow (X direction). A constant voltage V= 1V is applied to the GMR sensors.

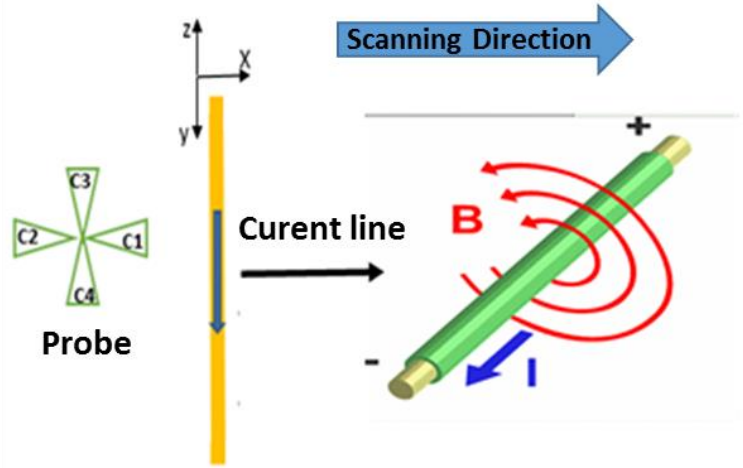

Figure 5.3- Measurement scheme of current line

The estimated magnetic field signal is accomplished by the fundamental physical relation between magnetic field and current, described by Biot-Savart law:

$$\overrightarrow{dB} = \frac{\mu_0}{4\pi} \frac{I\overrightarrow{dl} \times \vec{r}}{r^2} \quad (5\text{-}1)$$

Where B is magnetic induction, Idℓ is an element of the current I, the constant μ_0 is the permeability of free space, and r is the distance between the current and the sensor. Thus, the current can be directly calculated from the magnetic field if we know the distance that separates the current line and magnetic field sensor [170, 171].

Magnetic field emitted by the current line has a two-dimensional distribution in the x-z plane. This magnetic field emitted by the current line has a zero value on the y-axis. Figure 5.4, Figure 5.5, and Figure 5.6 compare the experimental results and the simulation results obtained on current line.

As the probe moves over the wire, the H_x component of the magnetic field will be negative, as seen in Figure 5.4. Blue color corresponds to the negative value of the Hx component. In addition, the measured field amplitude decreases slightly when the probe moves away from the current line.

The maximum amplitude of magnetic signal calculated with the sensor according to the x-axis (H_x) by Biot-Savart law is equal to 1.25 µT. The maximum amplitude of the magnetic signal obtained by the 3D probe in the case of H_x component is equal to 1.2 µT. The H_x component reconstructed by the 3D probe shows a good correlation with simulated results.

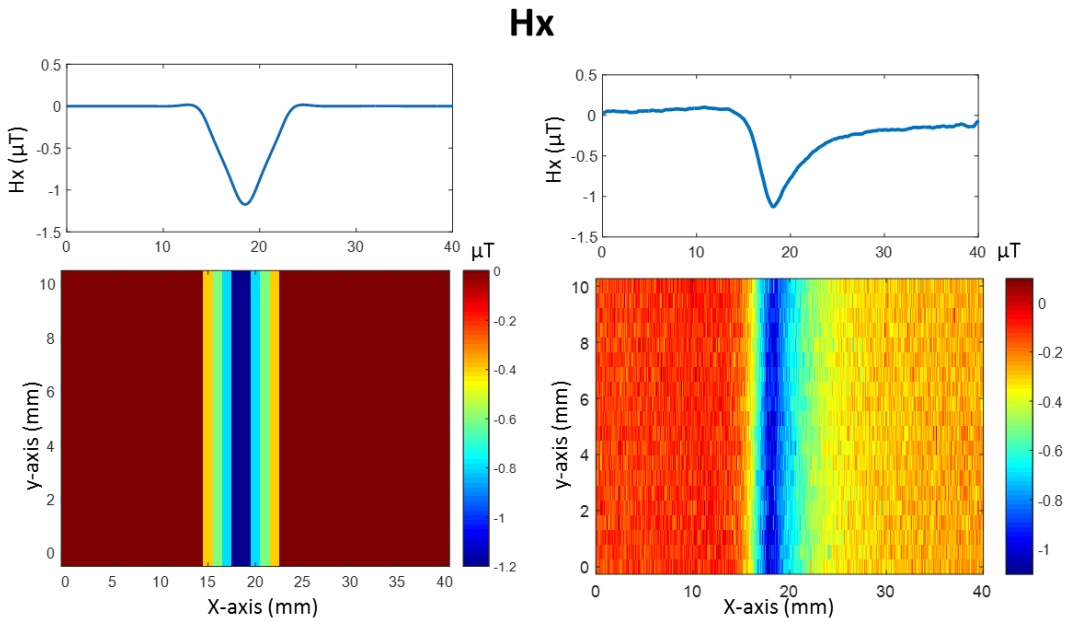

Figure 5.4- One dimensional (top) and two dimensional scans (bottom) of the magnetic field of a line current according to x-axis; simulation results of ***Hx.*** *component* ***(left part)*** *reconstruction of* ***Hx*** *component measured by 3D probe. The maximum amplitude is equal to 1.2 µT with SNR of 8.2 dB* ***(right part)***

The asymmetry in the experimental results may be due to a small gradient of the laboratory static field of about 50 nT/cm.

The value of magnetic field projection to the y-axis is zero, as shown in Figure 5.5. The magnetic signal calculated on y-axis (H_y) by Biot-Savart law is equal to zero. The H_y component is perpendicular to the sensitive axis of the GMR sensor, which confirms that the magnetic field reconstructed in the case of H_y is almost equal to zero. Observed residual component of field is about 30 nT. Thus, the error bar of the accuracy of the reconstruction is about 3%.

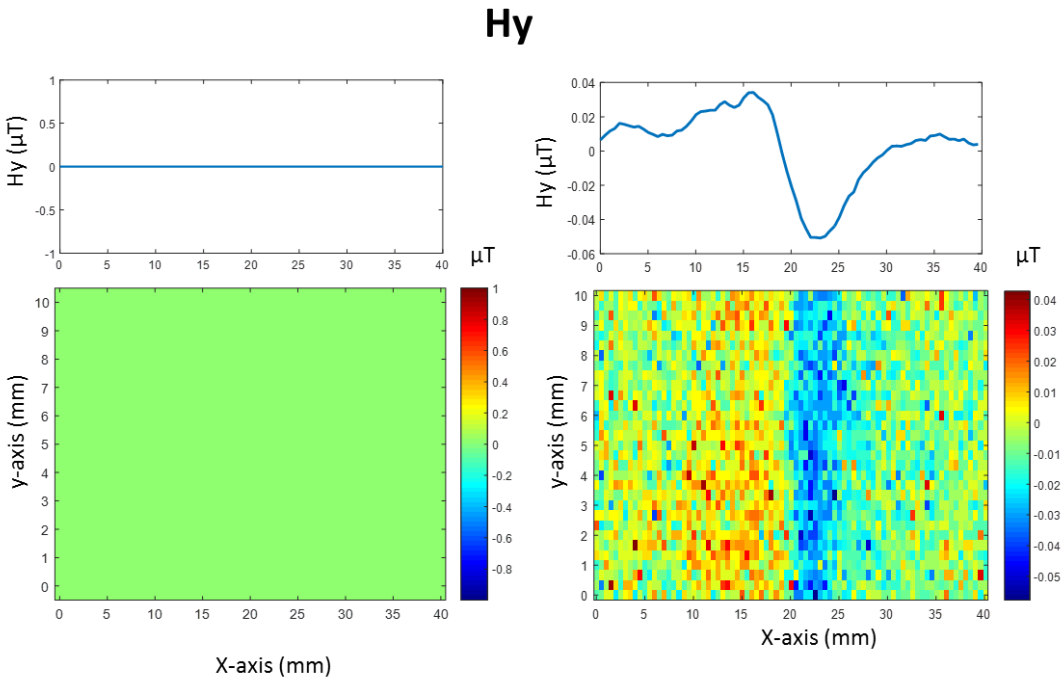

Figure 5.5- One dimensional (top) and two dimensional scans (bottom) of the magnetic field of a line current according to x-axis; simulation results of ***Hy*** *component* ***(left part)*** *reconstruction of* ***Hy*** *component measured by 3D probe.. The amplitude of Hy is almost equal to zero* ***(right part)***

The magnetic field projection to z-axis is in two opposite directions (Figure 5.6). As the probe moves over the wire, the H_z component of magnetic field will be first positive, then zero, then negative, as seen in Figure 5.6. Red and blue colors correspond to the positive and negative values of the H_z component. The maximum amplitude of magnetic signal calculated with on z-axis (H_z) by Biot-Savart law is equal to ±1.35 µT for a sample to sensor distance of 700 µm. The H_z component reconstructed from the measurement with 3D probe is equal to ±1.3 µT, which allows to estimate the experimental lift off. We still observe a small field gradient due to the setup.

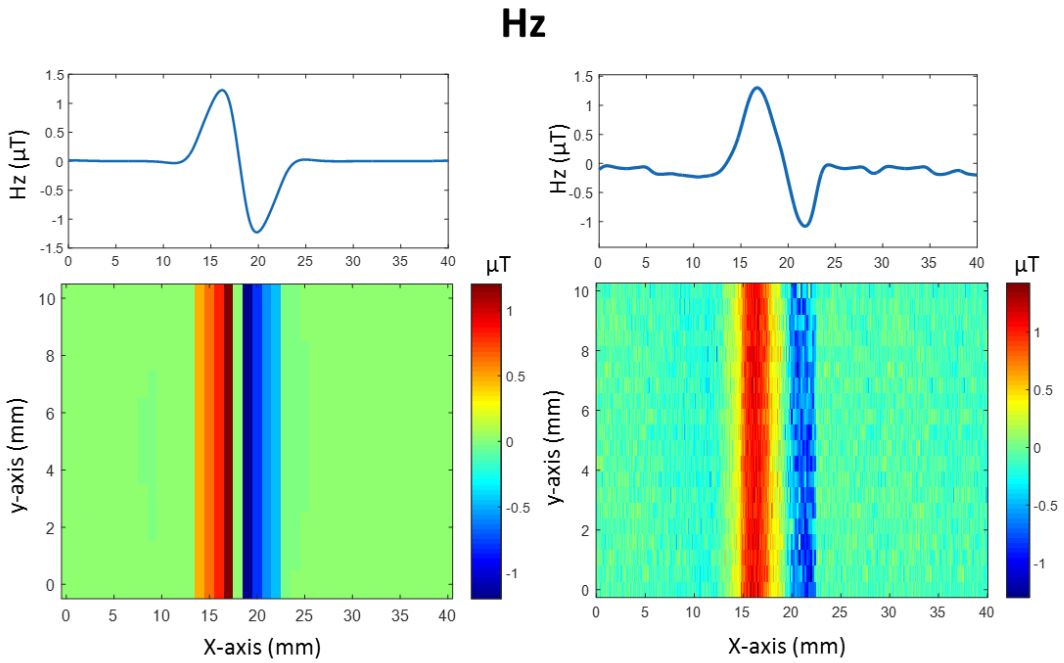

Figure 5.6- One dimensional (top) and two dimensional scans (bottom) of the magnetic field of a line current according to x-axis; simulation results of Hz component ***(left part)*** *reconstruction of Hz component measured by 3D probe.. The maximum amplitude is equal to 1.3 µT with SNR of 8.9 dB* ***(right part)***

5.4 Magnetic imaging of dollar bin

The performance in spatial resolution within a developed probe can be demonstrated with a magnetic image of a one-dollar bill. US Federal Reserve uses ink that contains particles of iron oxide that contains natural remnants of magnetization with a minimum grain size equal to 10 µm. Magnetic ink is used to reduce counterfeiting that gives the user a sense of security by capturing basic "amateur" counterfeit money bills [172].

A one-dollar bill has been placed on the test desk. The test desk is moved relative to the stationary 3D probe using a three-axis (x; y; z) mechanical stage. The distance between the probe and bill is 400 µm±100 µm. The scan step is 100 µm in the x and y axis. The magnetic image of George Washington's face on a dollar bill is saturated at 1 T along the vertical direction (z-axis) before measurements. A constant voltage V= 1 V is applied to the GMR sensors.Figure 5.7-right shows the result of the Hz component reconstructed by our 3D probe, which includes a major part of Washington's face compared with the result obtained by Kletetschka (Figure 5.7-left) [165]. Figure 5.7-center shows a photo of George Washington's face taken with a Nikon D7100 camera equipped with a macro lens with a focal length of 90 mm. In this

image, we reach the limit of resolution of the printing process used on the bill. Kletetschka scanned the dollar bill using a Hall sensor. This sensor is sensitive to the vertical component of the magnetic field. The z distance between the Hall sensor probe and dollar specimen is 0.125 mm.

Figure 5.7- Measurement results of George Washington's face in the case of Hz component detection obtained by Kletetschka [173] ***(left part).*** *Picture of part of Washington's face in one dollar bill* ***(center part)*** *and measurement results obtained by developed 3D probe* ***(right part)***

The obtained image is a mirror of the real dollar bill. It is compared to results obtained in [73, 173]. Our results show a good performance to detect the small quantities of magnetic ferrite material, giving more details of Washington's eye, nose, hair and neck. We can conclude that the distribution of magnetic ink in the dollar bill is not homogenous as expected.

In Figure 5.8, a bigger image of George Washington's face obtained by developed 3D probe is shown. Three magnetic field components are presented.

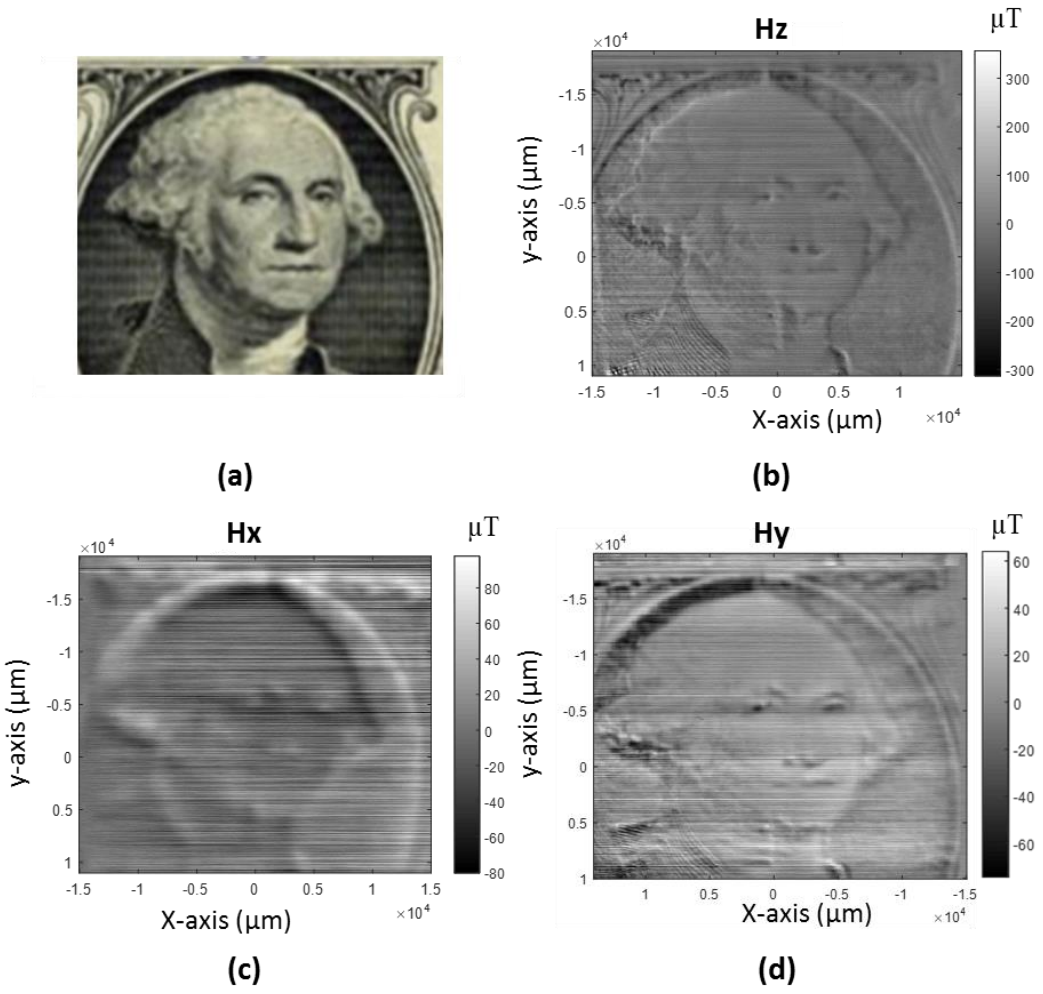

Figure 5.8- Picture of Washington's face in one dollar bill ***(a)*** *Magnetic image of a portion of a $1.00 bill scanned at a working distance of height of 400 μm, Hz component. The gray scale varies from about −300 μT(downward, black) to +310 μT(upward, white)* ***(b)*** *Magnetic image of Hx component. The gray scale varies from about −80 μT to +85 μT* ***(c)*** *Magnetic image of Hy component. The gray scale varies from about −65 μT to +60 μT in the case of Hy* ***(d)***

SNR is 38 dB for a normal component of magnetic field H_z, 13 dB for the H_y component and 11 dB for the H_x. As magnetic field within the dollar bill is oriented to the z-axis, the amplitude of normal component H_z is higher than that of H_x and H_y (Figure 5.8). The amplitudes of H_x and H_y components are different to zero due to the deviation of the induced field in the dollar bill. One interesting aspect is also the large contrast observed for example in H_x component at the edges, which shows that a part of the magnetization in the large dark areas (not so dark in H_z) remains with a planar magnetization.

5.5 Imaging of soft steel objects

The performance of 3D probe in detection of magnetic footprint of different shape objects in soft steel mock-up has been evaluated (Figure 5.9 and Figure 5.10). The aim of that study is to evaluate the performances of the probe for large static permanent fields as the mean field radiated by the object was several milliTesla. The distance between the objects is 0.5 mm and 1.5 mm. Steel is a metal alloy consisting mainly of iron and carbon and is processed to withstand mechanical and chemical stresses. The self-magnetic field in this mockup is very weak. For this reason, two magnets are put under the mock-up to induce a magnetic field. The steel mock-up shown in Figure 5.9 and Figure 5.10 has an electric conductivity of 5.9 $S.m^{-1}$.

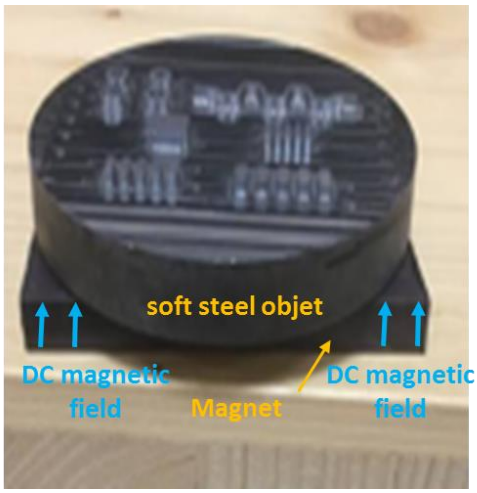

Figure 5.9- Steel mock-up with different shape objects

This specimen contains objects of different shapes: four circles, snake, square, and near bars. (Figure 5.10).

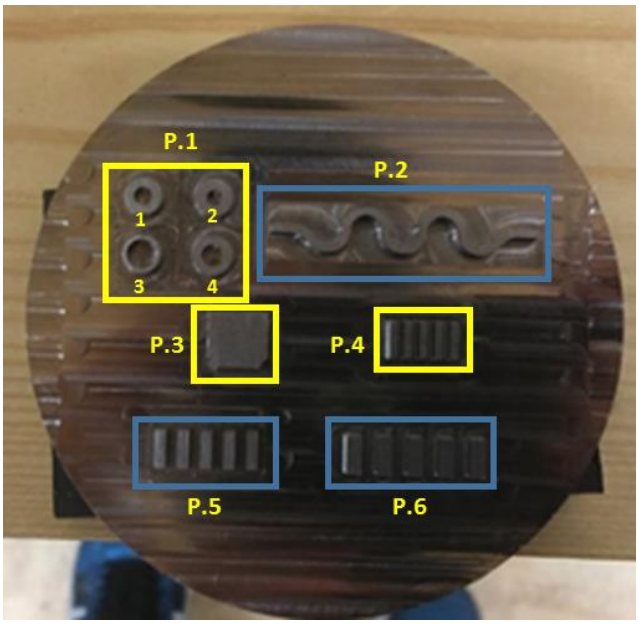

Figure 5.10- Steel objet that contains many shapes

To facilitate the study of these objects and to facilitate the analysis of the obtained results, we have divided the specimen in six parts presented in the table below:

	Shape	Dimensions
P.1	4 circles	1: dex=5 mm dint=2.4 mm 2: dex=5 mm dint=2 mm 3: dex=5 mm dint=4 mm 4: dex=5.2 mm dint=2.9 mm
P.2	Snake	Length L=36mm Thickness w=2mm
P.3	Square	9.2 x x6.8 mm²
P.4	5 bars	1.4 x 3.6 mm², distance between bars 0.5mm
P.5	5 bars	1.6 x 5.8 mm², distance between bars 0.5 mm
P.6	5 bars	2.8 x 5.8 mm², distance between bars 1.5mm

During the acquisition, the only movement is within the x–y plane, and the distance between the 3D probe and the mock-up is fixed at 400 µm. The scan step is 200 µm in the x and y axis. The magnet emits a non-homogenous field in steel mock-up of several milliTesla. Magnetic field in the specimen is oriented according to the z component. The normal component of magnetic field (H_z) obtained with the 3D probe is shown in Figure 5.11.

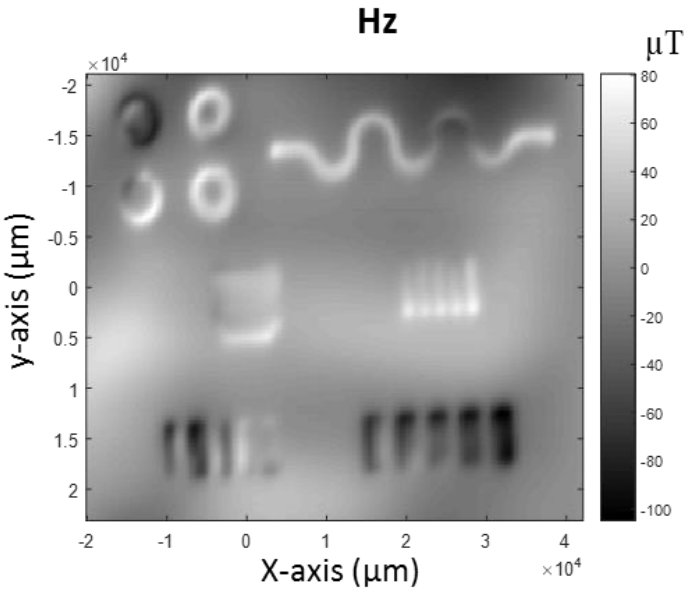

Figure 5.11- H_z component, the grey scale varies from −100 µT (downward, black) to +80 µT (upward, white)

It is observed that the objects are detectable with SNR = 27 dB. The black regions of the image correspond to an antiparallel magnetic field (the magnetic field emitted by the mockup is antiparallel to the easy axis of GMR sensor), whereas white color ones correspond to a parallel magnetic field.

- ✓ P.1: Circular shapes are well detected and their diameter could be estimated. It is observed that a circle number 1 (Figure 5.9) doesn't have the same magnetic signature (downward amplitude value = -86 µT) as other circles (upward value: **1**= +54 µT, **2**= +57 µT and **4**= +80 µT). This difference is due to a non-homogenous magnetic field in the specimen.
- ✓ P.2: Snake shape is well detected. The magnetic signature is upwards (white color) and has a signal amplitude between +40 µT and +60 µT.
- ✓ P.3: Square object is well detected with amplitude value equal to +45 µT.

- ✓ P.4: Five bars separated with distance of 0.5 mm are well detected, confirming good spatial resolution of the 3D probe. The magnetic amplitude values of five bars are between +30 µT and +60 µT.
- ✓ P.5: Five bars separated with distance of 0.5 mm are detected. The magnetic amplitude values of five bars are between -70 µT and 70 µT. The magnetic signature of bars is in the opposite value (upward and downward value) due to a non-homogenous magnetic field in the mock-up.
- ✓ P.6: Five bars separated with distance of 1.5 mm are well detected. The magnetic amplitude values of five bars are between - 80 µT and -100 µT.

Magnetic field emitted by the magnets is in the z-axis direction, however the magnetic field of studied objects undergoes a deviation in the x-y plane of the specimen. Figure 5.12 shows the H_x. and H_y. magnetic field components detected by the 3D probe.

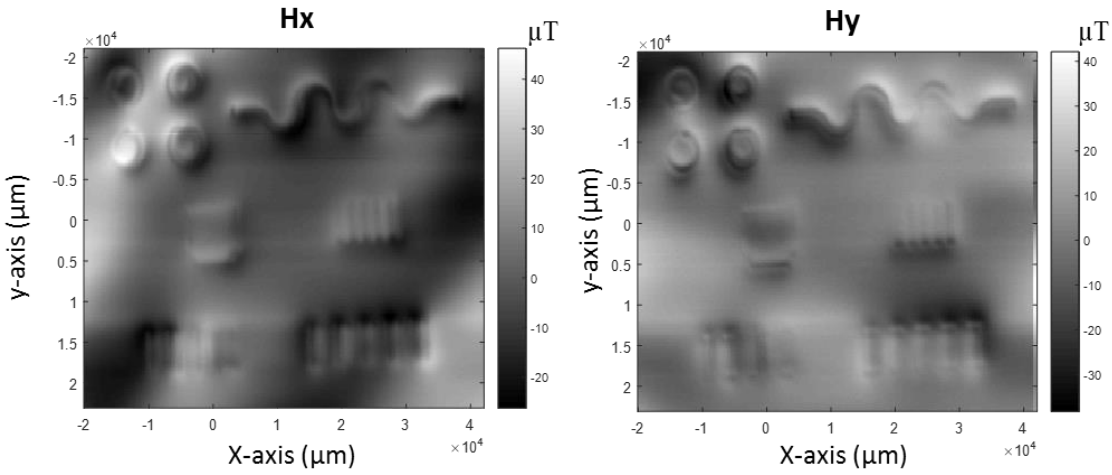

Figure 5.12-Hx and Hy components obtained by 3D probe. The gray scale varies from about −25 µT (downward, black) to +40 µT (upward, white) in the case of Hx ***(left part)*** *the gray scale varies from about −35 µT to +40 µT in the case of Hy* ***(right part)***

We can see that the magnetization of the objects is dominated by internal domains, which can be imaged by the 3D probes. Each domain orientation creates a positive or negative stray field, which is highlighted by the patterns done on the surface. The origin of this large scale inhomogeneity is unclear but may be related to an inhomogeneity of composition.

5.6 Susceptibility measurement

This part has been removed for confidentiality

5.7 Conclusion

In this chapter, we have described the use of 3D GMR probe in magnetic imaging. The developed probe shows a good detection of magnetic objects with different shapes.

The combination of the responses of the four GMR with the sensitivity calibration allows us to achieve accuracy along the three directions of fields better than 5%. The two types of probes have been evaluated. We have demonstrated that by using type 2 probes, we are able to image patterns in strongly magnetized objects.

The main limitation of the present set-up is related to the accurate control of the distance between the sample and the probes. Ultimately, an automatic system measuring the local distance should be incorporated in order to use efficiently the spatial resolution of GMR sensors.

Finally, we have tested the probe to perform susceptibility images of a sample. That technique should be further developed by incorporating the possibility of scanning the frequency on a wide range in parallel to the physical scanning. Interest will be to determine the local susceptibility of materials as function of frequency in order to characterize the local inhomogeneities.

Chapter 6. 3D Probe in Non-Destructive Testing

6.1 Introduction

Eddy current excitation combined with giant magnetoresistive sensor is interesting in defect detection that requires working at low frequencies, i.e. detection of buried flaws, and with high spatial resolution at high frequencies for very small surface cracks (under 100 µm) detection. In this chapter, eddy current excitation combined with 3D probe will be presented. This emitter part has been optimized in CIVA software [174]. We will show theoretical example of 3D probe performances in EC-NDT with reconstruction of three components of magnetic field. We will see in this chapter that the 3D probes enable to detect the defects at both surface and sub-surface levels. We will use the 3D probes based on type 1 sensors to exploit their high sensitivity (about 20 V/V/T) for defect detection. For subsurface defect detection, the experimental results obtained in Aluminum and Inconel mock-ups are analyzed and compared with simulation results. Titanium and Aluminum samples containing small surface defect (under 600 µm) have been used for probe evaluation for surface cracks detection. The performance of 3D probe for small surface defects detection in Aluminum and Titanium mock-ups are compared with simulation results.

6.2 Optimization of EC probe

The design of the probe (the emitter part and the 3D probe) for NDT application has been optimized with CIVA software.

Figure 6.1 shows the details of the three axis probe with GMR sensors as receiver. For NDT application, 3D probe described in Chapter 4 is used as receiver and two current foils are used as emitters (Figure 6.2). 3D probe and the current foils are fixed on mechanical support. Emitters are placed in horizontal. The GMR sensors detect a low magnetic field in the absence of defect.

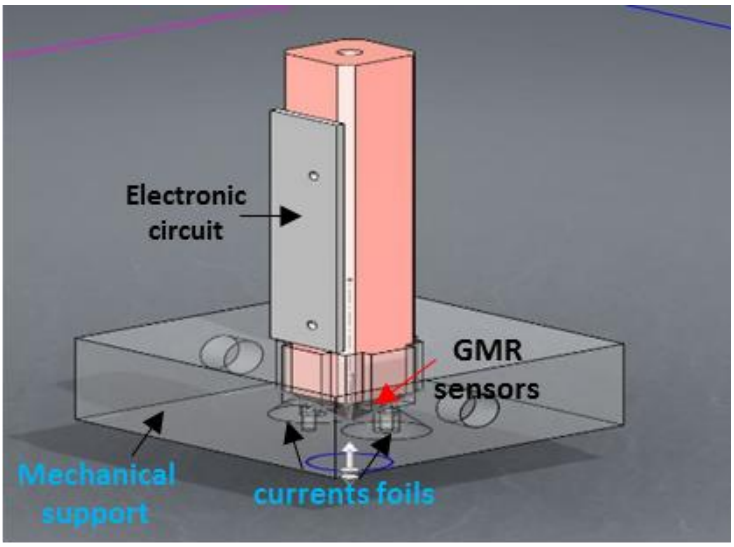

Figure 6.1-*3D Probe based on a GMR array receiver and two current foils emitters*

The two current foils used as emitter have the following dimensions: internal length L = 20 mm, the internal width W = 12 mm and the total width E = 2 mm. A rectangular hole is placed in the center between two current foils in order to place receiver. Each current foil has eight layers and each layer has four turns. The current foils parameters are detailed in Figure 6.2. These parameters have been optimized in CIVA software.

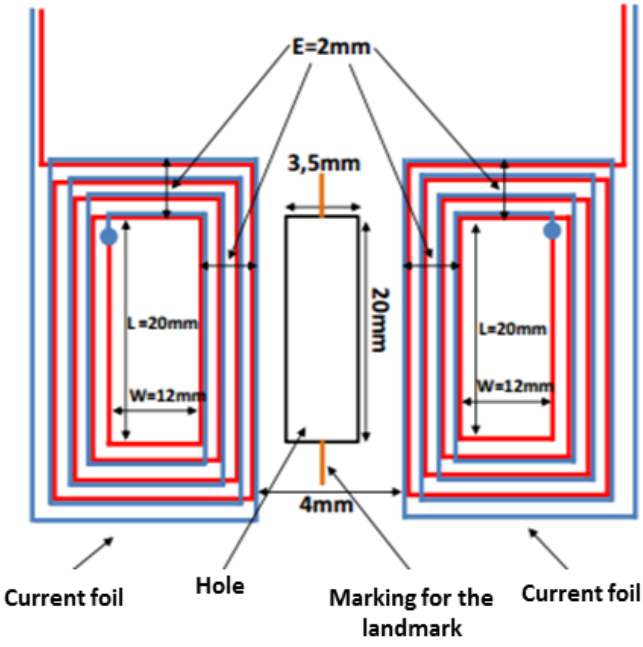

Figure 6.2- The parameters of two current foils

In order to obtain the field almost equal to zero (according to z component) in the absence of defect, the emitters are excited in opposite direction (in opposition phase). Figure 6.3 illustrates the form of current into the two current foils.

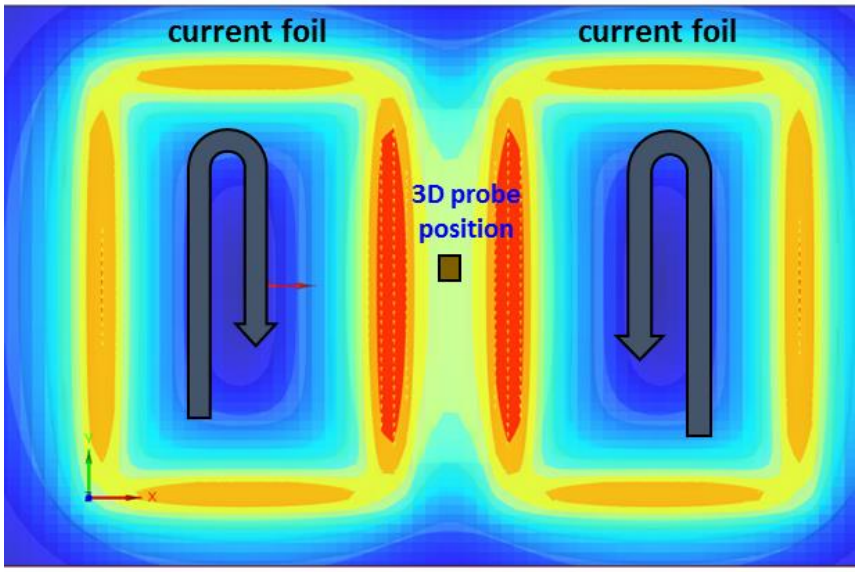

Figure 6.3- Schematic of opposite excitation in two current foils emitters

In the case of working with normal (z) component of magnetic field, this method of excitation avoids the saturation of GMR receiver. This excitation allows to obtain homogenous and parallel current in the mock-up. Also, it allows to use GMR receiver with high sensitivity, operating in weak field.

On the contrary, when the foils emitters are excited at the same direction, the GMR sensors receivers evolve in strong field even in the absence of mock-up, the value of magnetic field measured by receiver in z-plane is very high.

Figure 6.4 illustrates the magnetic induction in aluminum mock-up for the two types of excitation current cited above. These simulation results are made using CIVA software. The applied current is 100 mA. It is shown that the coupling noise is much lower in the case of the two current foils excited in opposition phase than the case of excitation in phase (the same direction).

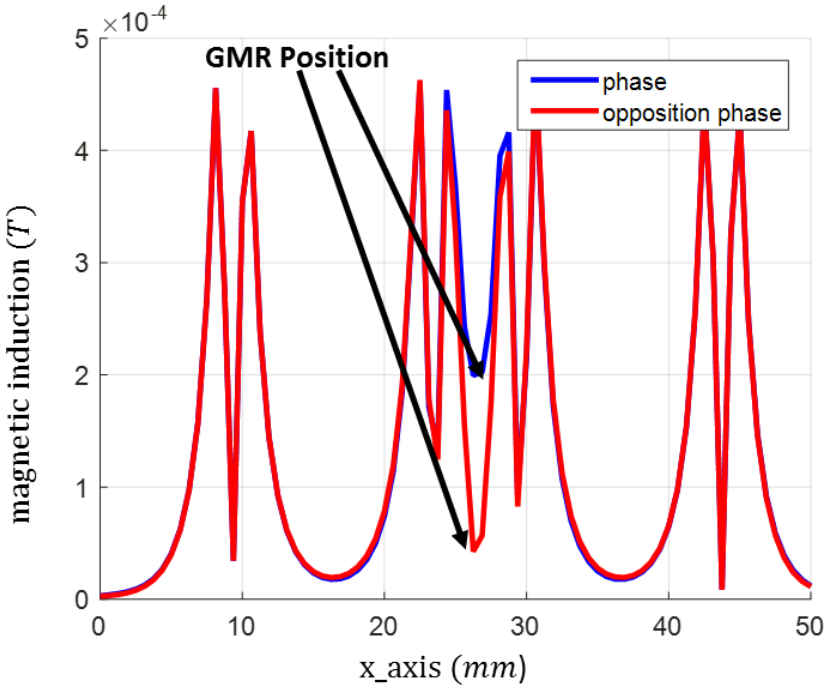

Figure 6.4- Image of 1D z component distribution of magnetic induction reflected by aluminum mock-up for the two forms of excitations: phase and opposition phase

The optimal distance between the coils has been defined by simulations. Figure 6.5 illustrates the magnetic induction reflected by aluminum mock-up for different distances between the two current foils.

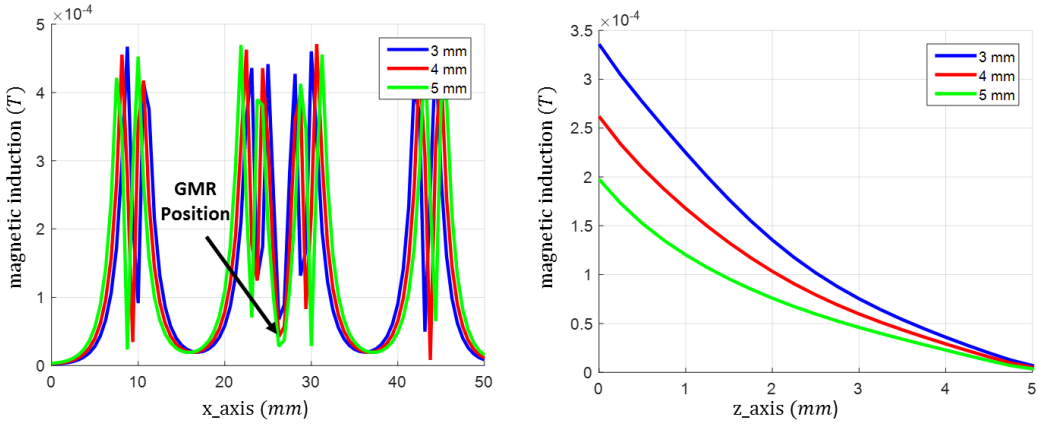

*Figure 6.5- Distribution of z-component of magnetic induction reflected by aluminum mock-up at different distance between the two current foils with the applied current of 100 mA **(left part),** 1D z-zone distribution at fixed x and y positions (GMR position) **(right part)***

We have chosen the distance between the two current foils equal to 4 mm, compromise between the coupling noise value and the magnetic induction intensity.

6.3 3D EC probe

6.3.1 Simulation results with 3D EC probe

To validate the operation of 3D probe in the reconstruction of the three magnetic fields components, we made a configuration in CIVA software similar to 3D EC probe (Figure 6.6).

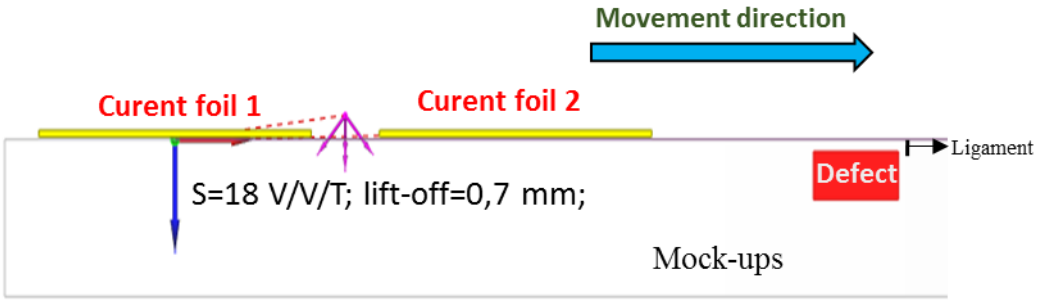

Figure 6.6- Configuration realized in CIVA for 3D probe.

Aluminum mock-up ($\sigma = 19.5\ MS.m^{-1}$) has been used for simulations of 3D probe. The defect with following dimensions has been studied: length × width × depth = 5 mm × 0.15 mm × 2 mm. The ligament (the distance between the flaws and the mock-ups surface) is 0.5 mm. The excitation frequency f = 50 kHz and excitation current of I=20 mA have been chosen. The applied voltage to GMR receivers is 0.2 V.

The results of reconstruction of H_x component (real part of the signal) are compared with results of simulations of the case when receiver is placed along x-axis (Figure 6.7).

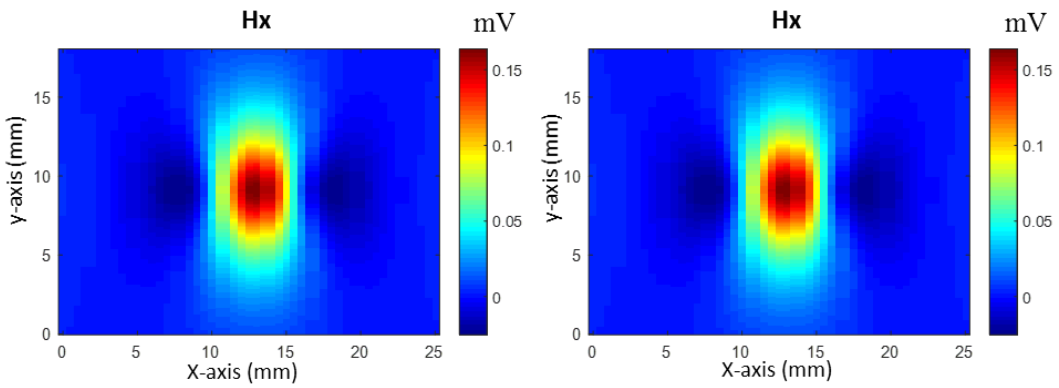

*Figure 6.7- CSCAN of the defect in aluminum mock-up obtained with receiver placed according to x- axis **(left part),** reconstruction of H_x component obtained with 3D EC probe **(right part)**.*

The lobe signature in Figure 6.7 corresponds to the flaw position. H_x component has the advantage of having a monopole signature that is simple to interpret.

The results of reconstruction of H_y component (real part of the signal) are compared with H_y obtained by simulations of the case when receiver is placed according to y-axis (Figure 6.8)

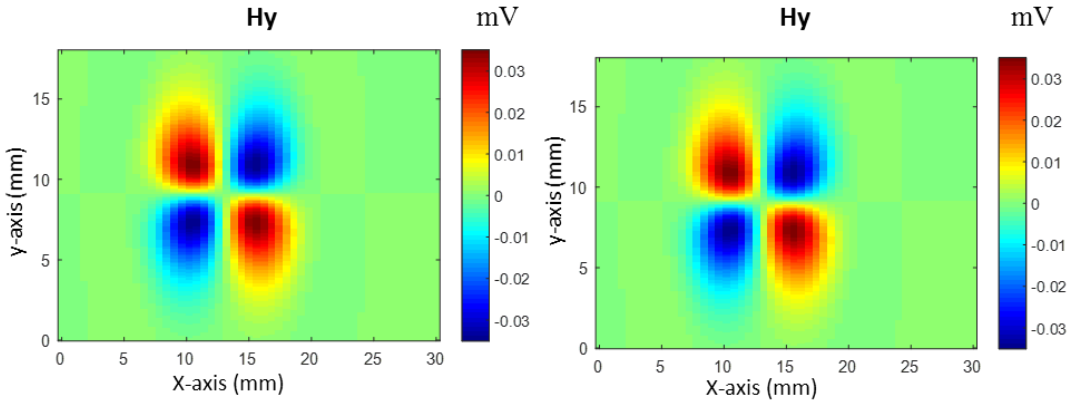

*Figure 6.8- CSCAN of the defect in aluminum mock-up obtained with receiver placed according to y-axis **(left part),** reconstruction of H_y component of magnetic field with 3D EC probe **(right part)**.*

The four lobes signature in Figure 6.8 corresponds to the four edges of the flaw. This configuration has the advantage of having zero direct coupling.

The result of reconstruction of H_z component (real part of the signal) are compared with H_z obtained by simulations of the probe with receiver placed according to z-axis (Figure 6.9)

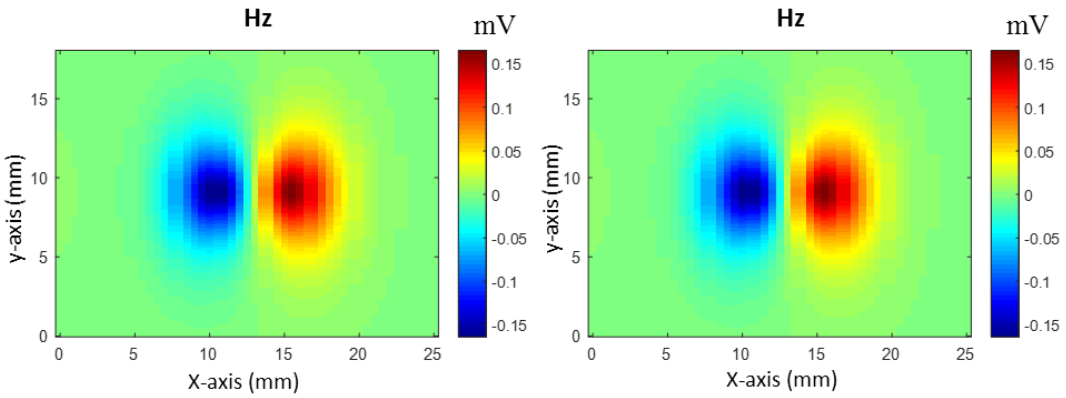

Figure 6.9- CSCAN of the defect in aluminum mock-up obtained with receiver placed according to z-axis ***(left part),*** *reconstruction of H_z component of magnetic field with 3D EC probe* ***(right part)***

The two lobes signature in Figure 6.9 corresponds to two extremities of the flaw. Moreover, this configuration has the advantage of having zero direct coupling in the case of receiver placed along z axis.

The three magnetic field components reconstructed theoretically by the 3D Probe are in good agreement with the results obtained by depositing sensors according to the three axis.

6.3.2 Experimental Results

6.3.2.1 Subsurface defects

Aluminum mock-up

Aluminum mock-up with flaws has been used for probe performance evaluation. Applied current for emitters is 20 mA at frequency at 50 kHz. The applied voltage to the GMR receivers is 1 V. The distance between the 3D probe and the mock-up is fixed at 700 µm. The scan step is 500 µm in the x-axis and 100 µm in the y-axis The CSCAN image highlights detection and reconstruction of the three field components of a defect of size 5×0.2×2 mm^3, located at ligament of 0.5 mm (Figure 6.11, Figure 6.12, Figure 6.13).

Experimental set-up is shown in Figure 6.10. It is based on the acquisition card National Instruments PCI6251, signal generator with 4 channels to generate three synchronized frequencies, and lock-in. Signal generator is used for alimentation of emitters and reference signal to the lock-in. The signal from receiver element is sent to

the lock-in where it is demodulated and is sent to acquisition card. Acquisition is then analyzed using CIVA software.

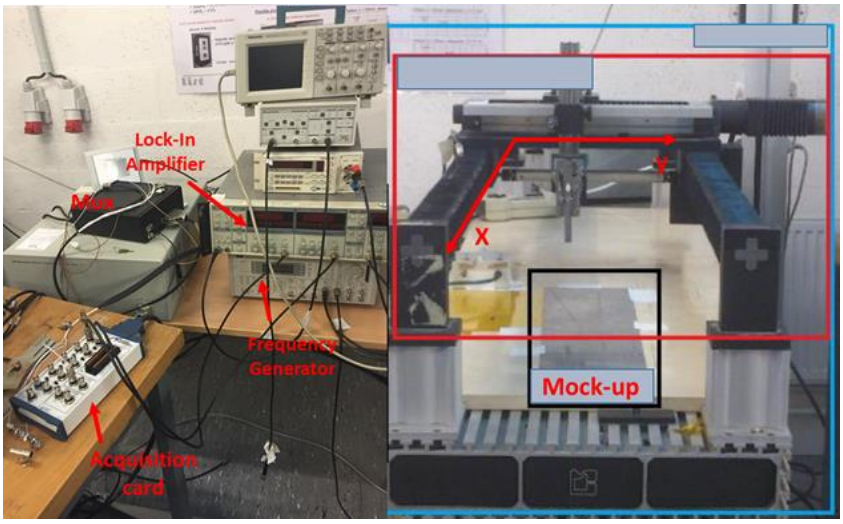

*Figure 6.10- Experimental set-up for EC measurements **(left part)** 3D probe installed **(right part)**.*

Figure 6.11, Figure 6.12, and Figure 6.13 show comparison between simulated results (real part) with receivers position according to x-, y- and z-axis and reconstruction of three components of magnetic field (H_x, H_y, and H_z) from experimental results obtained with 3D probe at the defect of size 5×0.2×2 mm^3, located at ligament of 0.5 mm.

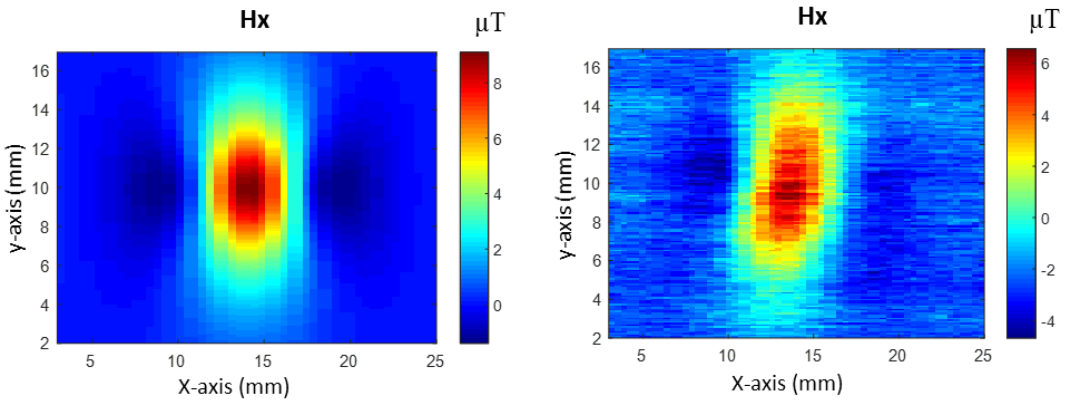

*Figure 6.11- Simulation results **(left part)** and experimental results **(right part)** in the case of Hx component measurement*

The one lobe signature of CSCAN in Figure 6.11 corresponds to the flaw detected with 6 µT as maximal amplitude for experimental results, with a signal to noise ratio (SNR) is equal to 21 dB.

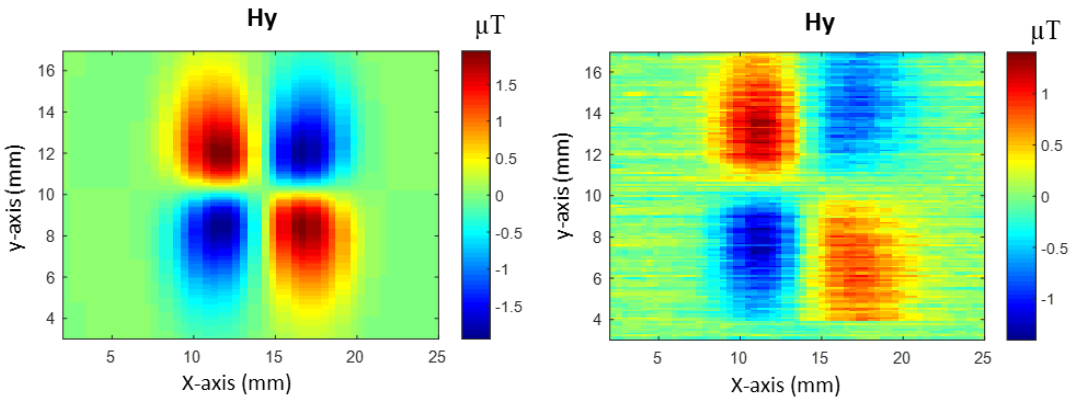

*Figure 6.12- Simulation results **(left part)** and experimental results **(right part)** in the case of Hy component measurement*

The four lobes signature in Figure 6.12 corresponds to the 4 edges of the flaw. The maximal amplitude in EC measurements is 1.5 µT, SNR=19 dB.

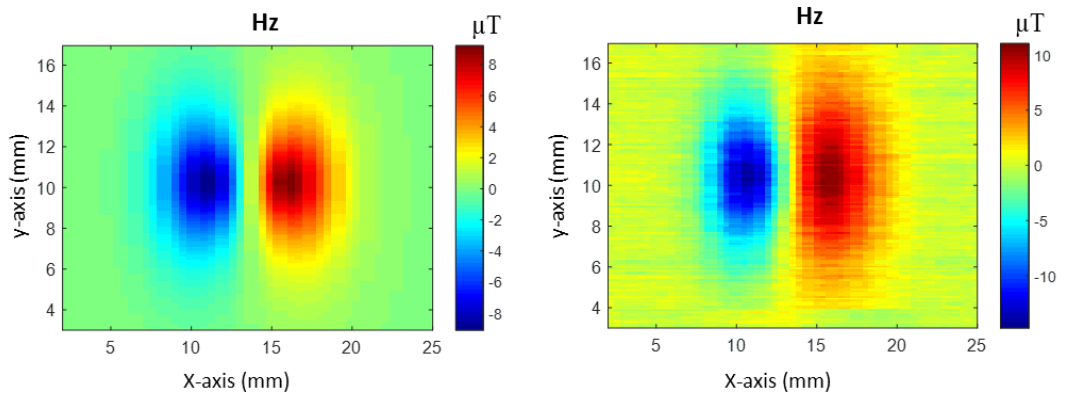

Figure 6.13- Simulation results (left part), and experimental results (right part) in the case of Hz component measurement.

The two lobes signature in Figure 6.13 corresponds to two extremities of the flaw. The maximal detected amplitude is 12 µT. The defect is detected with signal to noise ratio of SNR=27 dB.

The experimental results of magnetic response show a strong correlation with simulation results in the case of three analyzed components of magnetic field.

Inconel mock-up

Inconel mock-up ($\sigma = 0.97\, MS.m^{-1}$) has been also used for 3D EC probe performances evaluation for subsurface defects detection. The excitation frequency of f = 70 kHz and current of I=50 mA applied to emitters have been chosen. The applied

voltage to the GMR receivers is 1 V. The distance between the 3D probe and the mock-up is fixed at 700 µm. The scan step is 500 µm in the x and 100 µm in the y axis. An example of detection of defect with following dimensions: length × width × depth = 4 × 0.1 ×0.93 mm^3 with ligament of 1.3 mm is analyzed below.

Figure 6.14, Figure 6.15 and Figure 6.16 show comparison between the simulated results with receiver position to x-, y- and z-axis and reconstruction of three components of magnetic field (H_x, H_y, and H_z) from experimental results obtained with 3D EC probe. Real part of the signal is studied

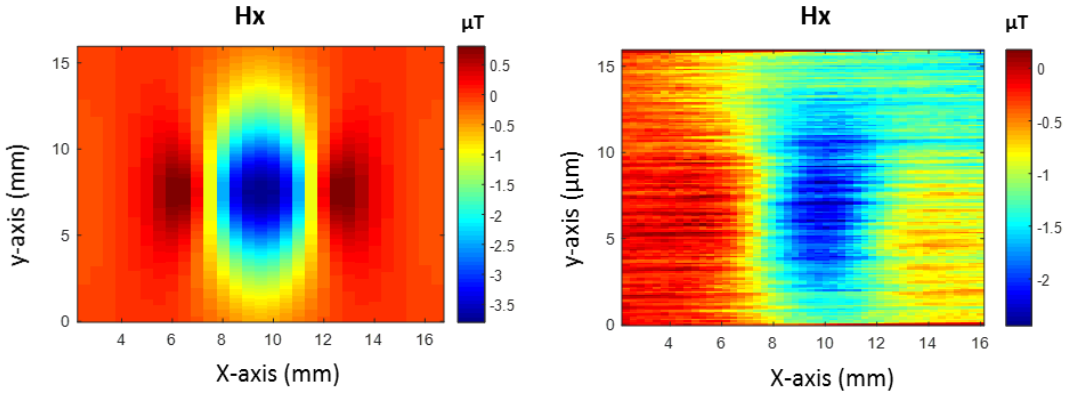

*Figure 6.14- Simulation results **(left part)** and experimental results **(right part)** in the case of Hx component measurement*

The lobe signature in Figure 6.14 corresponds to the flaw position. The maximal amplitude of detected signal is 2.5 µT with SNR=23 dB.

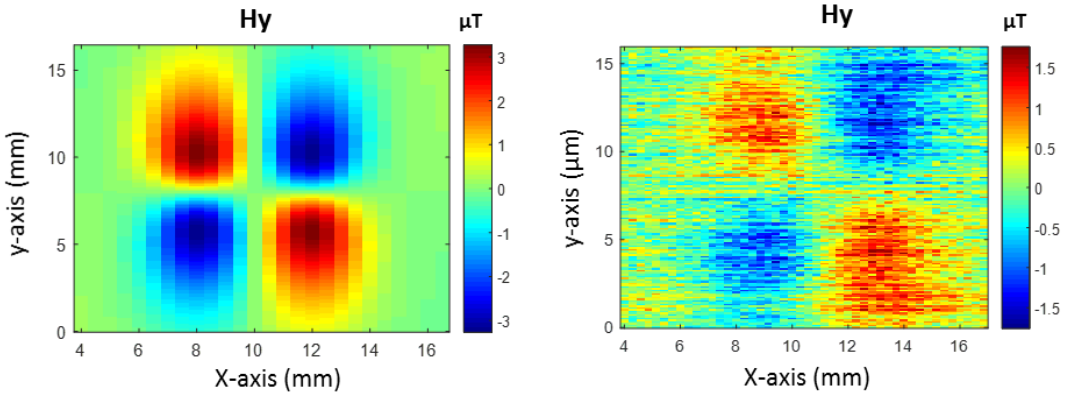

*Figure 6.15- Simulation result's **(left part)**, and experimental results **(right part)** in the case of Hy component measurement*

The four lobes signature in Figure 6.15 correspond to the four edges of the flaw. Maximal detected amplitude is 1.6 µT. The defect is detected with SNR= 17 dB.

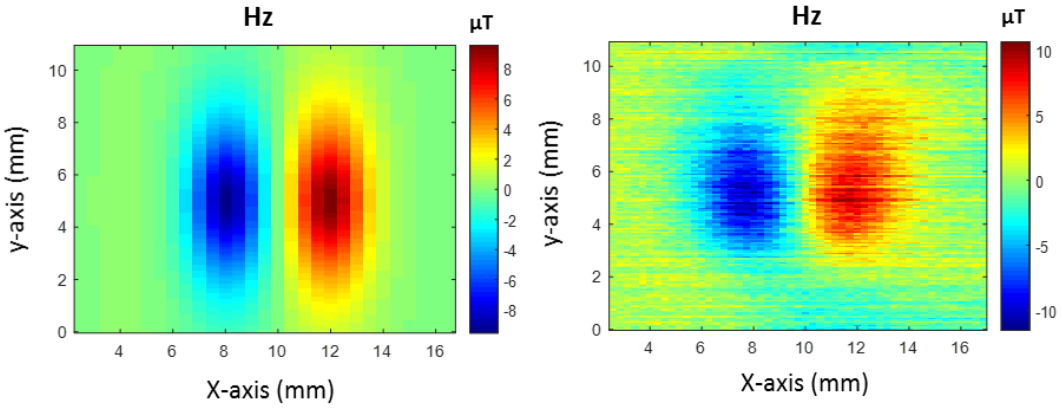

Figure 6.16- Simulation result's (left part), and experimental results (right part) in the case of Hz component measurement.

The two lobes signature in Figure 6.16 correspond to two extremities of the flaw. Maximal detected amplitude is 10 µT. The defect is detected with SNR= 28 dB.

The experimental results of defect magnetic response show a good correlation with simulation results in the case of three components of magnetic field.

6.3.2.2 Surface defects

Aluminum mock-up

Experimental testing in Aluminum mock-ups ($\sigma = 18\, MS.m^{-1}$) containing four defects (Figure 6.17) has been performed for evaluation of 3D probe for small defects detection. The defects have the same width and height: w= 0.04× h=0.05 mm^2 and have the following lengths : 0.7 mm, 0.5 mm, 3 mm and 2 mm. Applied current for emitters is 20 mA. All defects are well detected with excitation frequency f = 100 kHz. The applied voltage to the GMR receivers is 1 V.

Figure 6.17- Aluminum mock-up.

The three following figures show comparison between simulated results with receivers position according to x-, y- and z-axis and reconstruction of three components of magnetic field (H_x, H_y, and H_z) from experimental results obtained with 3D EC probe. Real part of the signal is studied. The scan step is 100 µm in the x-axis and 25 µm in the y-axis. The distance between the 3D probe and the mock-up is 400 µm.

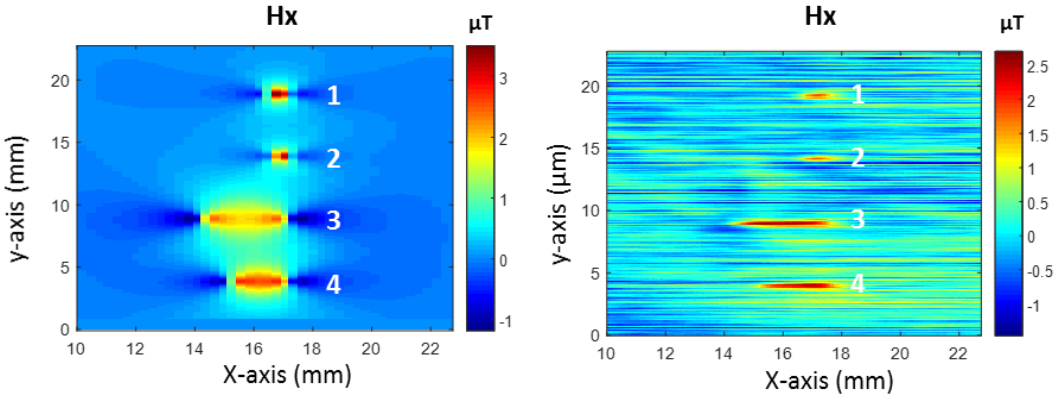

*Figure 6.18- Simulation results **(left part)** and experimental results **(right part)** in the case of Hx component measurement*

Figure 6.18 shows that each defect is detected with one lobe signature. Experimentally the defects are detected with SNR =13.8 dB for defect 1 (l=0.7 mm), SNR=13 dB for defect 2 (l=0.5 mm), SNR=16 dB for defect 3 (l=3 mm) and SNR=15 dB for defect 4 (l=2 mm). Maximal detected amplitude is 1.5 µT, 1.3 µT, 2.5 µT and 2.3 µT respectively.

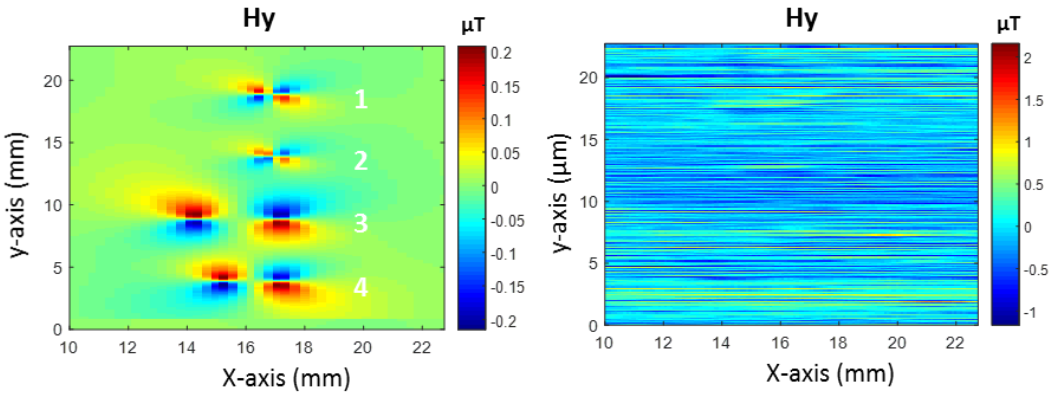

*Figure 6.19- Simulation results **(left part)** and experimental results **(right part)** in the case of Hy component measurement*

We show in Figure 6.19 (right part) that the 3D probe doesn't detect the Hy component of magnetic field. This inability of detection is due to the small width of four defects (40 µm). Estimated weak magnetic amplitude of Hy component of order of 0.2 µT (Figure 6.19-left part) and the noise level is equal 2 µT. Thus, Hy component is hidden into the intrinsic noise.

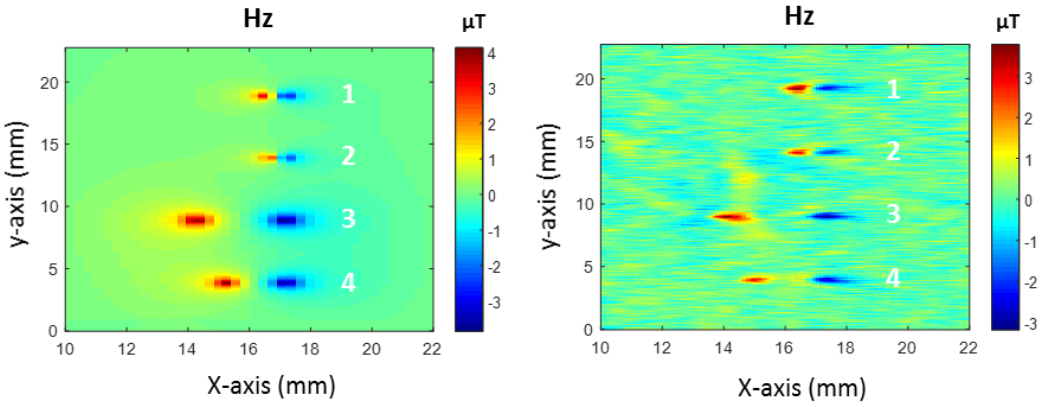

*Figure 6.20- Simulation results **(left part)** and experimental results **(right part)** in the case of Hz component measurement*

Figure 6.20 shows that each defect is detected. The signature of detected defects corresponds to two extremities of the defects. Experimentally, the defects are detected with SNR =16.7 dB for defect 1 (l=0.7 mm), SNR=16 dB for defect 2 (l=0.5 mm), SNR=17.6 dB for defect 3 (l=3 mm) and SNR=17 dB for defect 4 (l=2 mm). Maximal detected amplitude is 2.8 µT, 2.6 µT, 3.5 µT and 3 µT respectively.

Titanium mock-up

Titanium mock-ups ($\sigma = 0.6\, MS.m^{-1}$) have also been used for 3D Ec probe evaluation for surface defects detection. This material is rather difficult due to it low conductivity compared with Aluminum. This makes the detection of small defects harder as EC signals are small. Applied current for emitters is 50 mA. The chosen excitation frequency is 1 MHz. The applied voltage to the GMR is 1 V. The scan step is 100 µm in the x-axis and 25 µm in the y-axis. The distance between the 3D probe and the mock-up is fixed at 400 µm. The measurements have been performed on the mock-up with the defect with following dimensions: length × width × depth = 0.6 × 0.05 ×0.03 mm^3.

The three following figures show comparison between the simulated results with receivers position according to x-, y- and z-axis and reconstruction of three components of magnetic field (H_x, H_y, and H_z) from experimental results obtained with 3D EC probe. Real part of the signal is studied. We show only 1-D results, as detection of defects has been performed in one-line scan.

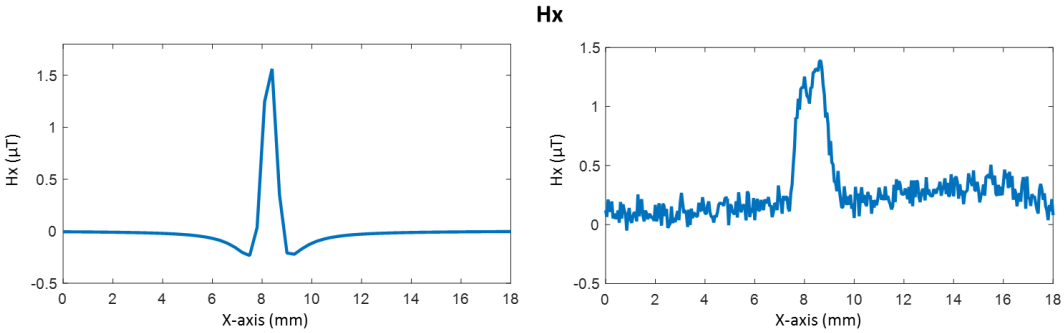

*Figure 6.21- Simulation results **(left part)** and experimental results **(right part)** in the case of Hx component measurement*

The results shown in Figure 6.21 correspond to the defect response in tangential component H_x. The defect is detected with maximal amplitude of 1.5 µT and with SNR = 12.3 dB. Experimental results are in good agreement with the simulation results.

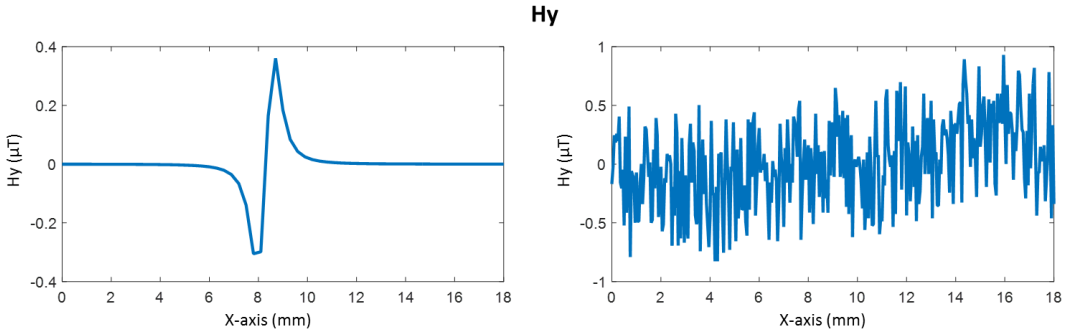

*Figure 6.22- Simulation results **(left part)**, and experimental results **(right part)** in the case of Hy measurement*

We show in Figure 6.22 (right part) that the 3D probe doesn't detect the Hy component of magnetic field. This inability of detection is due to the small width of the defect (50 µm), to the weak magnetic amplitude of Hy component (estimated to 0.4 µT) (Figure 6.22 -left part), and to the noise level in experimental results (Figure 6.22 –left part) that is equal to 0.8 µT

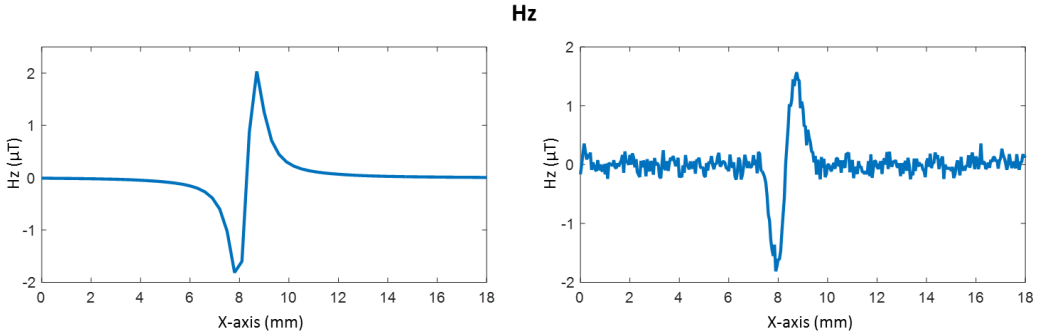

Figure 6.23- Simulation results (left part), and experimental results (right part) in the case of Hz component measurement.

The two lobes signature in Figure 6.23 corresponds the extremities of the defect. It is is detected with maximal amplitude of 1.9 µT and SNR= 13 dB. Experimental results are in good agreement with the simulation results.

6.4 Conclusion

In this chapter, performances of 3D EC probe have been evaluated. The 3D receiver combined with emitter part described in this chapter has achieved a detection of µm-sized defects. For this purpose, we measured the magnetic field response caused by defects in Aluminum, Inconel and Titanium mock-ups. For subsurface and surface

defects detection, the developed 3D EC probe has demonstrated the capability of detection of subsurface defect at ligament of 0.5 mm in Aluminum mock-up and at ligament of 1.3 mm in Inconel mock-up. Small surface defect of 500 μm in Aluminum mock-up has been detected with magnetic field detection limit of 2 μT. Also small surface defect of 600 μm in Titanium mock-up has been detected with magnetic field detection limit of 0.8 μT.

Conclusion and Future works

The main goal of this thesis work was to investigate probe allowing simultaneously reconstruction of three components of magnetic field at the same measurement point of measurement. 3D probes have been used for non-destructive testing and magnetic imaging applications. We have succeeded to overcome the limits of detection of three components of magnetic field simultaneously at the same point of measurement by using four orientations of GMR sensors.

The design of probe which comprises of various aspects including mechanical, electronic and software elements has been developed. Different types of micron-sized GMR sensors have been developed for different applications with a compromise between detectivity and magnetic field range. Probe layouts and coil dimensions have been optimized with CIVA software for ECT application. In micro-magnetic imaging, the 3D probe has detected the three components of magnetic field emitted by current line in good agreement with simulations. Magnetic imaging of one-dollar bill, and structured metallic object has been realized. Also, susceptibility measurements have been realized with the 3D probe.

Performances of these probes have been evaluated in cases of sub-surface flaws and surface cracks detection for EC-NDT. For sub-surface flaws detection, the 3D probe has demonstrated their capacity of defect detection at size of 600 µm in titanium and of 500 µm in aluminum mock-ups. Results in terms of signal to noise is comparable to single component probe detection.

Future work

- The next-stage work will be the development of GMR–array based 3D probes to reduce testing time with the possibility of greater area inspection at one time. This work has begun with the fabrication of 2D lines of sensors, which can be mounted at 45°. But during the time of my PhD I did not have enough time to test these new probes.
- For 3D detection in NDT applications, it would be interesting to combine different technologies. For example, micro-coils can be used to detect the perpendicular field whereas GMR sensors are used for detection of planar components of the field. This would permit the fabrication of 2D arrays of sensors.
- Investigate a correlation relationship between the defect shape and output signals of the 3D probe by developing a hierarchical structure for defect classification and quantification: The relationship between the magnetic field signal reflected by the defects and defects dimensions can be used to characterize defects. For this reason, develop a statistical approach for the influence of each defect parameters on the three components of field (frequency, ligament, lift-

off, length, width and depth) is very interesting. Indeed, further investigation will be undertaken by using wide range of defect samples to create a big database.

- We have tried to use the frequency information to have a more accurate determination of a defect in NDT. This is particularly suitable with GMR sensors as they are wideband detectors. I have made a number of simulations but this work would require more in depth work.
- Optimization of the sensing elements and the downstream electronics, i.e. integrated the ASIC (application-specified integrated circuit) system to the 3D probe for processing the sensor signals [175].: The ASIC is a specific CMOS circuit that should provide the biasing for the sensor array and do the reading of the sensors output for further processing. More specifically the ASIC drives the magnetic sensors; multiplexes/sample the signals; amplify/filter the signals.
- One key point of this work is an accurate control of sensor-surface distance. We can have a calibration with a current line like we have done but a continuous measurement of the distance by, for example, laser interferometry will be particularly important for magnetic imaging and would allow a better image acquisition.
- Replace the GMR sensors by TMR sensors in application that need to work at high frequencies. For example, for surface cracks detection, TMR are very promising in terms of the possibility of detection and spatial resolution.
- Insert the GMR sensors in half bridge configuration with two active resistances and two GMR sensors or full bridge configuration with four GMR sensors to eliminate the thermal effects. With this configuration the noise level decreases, so the detection limit of magnetic field reduces. We have not developed such probes in my PhD but it is possible to locally reverse the magnetization of GMR sensors and then suppress thermal drifts. This is important for DC magnetic imaging where thermal fluctuations are the main cause of image deformation.

References

[1] P. Ripka, «Induction sensors Magnetic,» *Sensors and Magnetometers,* p. 47–74, 2001.

[2] G. Musmann and Y. Afanassiev, "Fluxgate Magnetometers for Space Research," *Norderstedt: Books on Demand,* no. 12, 2010.

[3] P. Fendley, A. Ludwig et H. Saleur, «Exact nonequilibrium transport through point contacts in quantum wires and fractional quantum Hall devices,» *Physical Review B,* vol. 52, 1995.

[4] Machado and al, "A theoretical model for the giant magnetoimpedance in ribbons of amorphous soft-ferromagnetic alloys," *Journal of Applied Physics,* vol. 79, no. 8, p. 6558–6560, 1996.

[5] J. Wegrowe, S. Gilbert, D. Kelly et B. Doud, «Anisotropic magnetoresistance as a probe of magnetization reversal in individual nono-sized nickel wires,» *IEEE Magnetics Society,* vol. 34, pp. 903 - 905, 1998.

[6] C. Fermon, M. Pannetier-Lecoeur, N. Biziere and B. Cousin, "Optimised GMR sensors for low and high frequencies applications," *Sensors and Actuators A: Physical,* vol. 129, no. 1-2, pp. 203-206, 2006.

[7] M. Pannetier, C. Fermon, G. Le Goff, J. Simola and E. Kerr, "Femtotesla Magnetic Field Measurement with Magnetoresistive Sensors," *Science,* vol. 304, no. 5677, pp. 1648-1650, 2004.

[8] J. Clarke et A. Braginski, «Fundamentals and Technology of SQUIDs and SQUID Systems,» *The SQUID Handbook ,* vol. 1, 2004.

[9] A. Mahdi, L. Panina and D. Mapps, "Some new horizons in magnetic sensing: high-Tc SQUIDs, GMR and GMI materials.," *Sensors and Actuators A: Physical,* vol. 105, no. 3, pp. 271-285., 2003.

[10] H. Nyquist, "Thermal agitation of electric charge in conductors," *Phys.Rev.*, vol. 32, no. 1, pp. 110-113, 1928.

[11] F. Hooge, «1/f noise is no surface effect,» *Phys. Lett. A,* vol. 21, pp. 139-140, 1969.

[12] S. Kogan, «Electronic noise and fluctuations in solids,» *Cambridge University Press, Cambridge England, New York, NY,* 1996.

[13] M. Pannetier, C. Fermon, J. Simola, E. Kerr et J. Coey, «Noise in small magnetic systems{applications to very sensitive magnetoresistive,» *Journal of Magnetism and Magnetic Materials,* pp. 290-291 (Part 2) :1158-1160, 2005.

[14] V. Trauchessec, «Local magnetic detection and stimulation of neuronal activity,» Thèse de doctorat de l'Université Paris-Saclay préparée au Service de Physique de l'Etat Condensé, CEA, 2017.

[15] S. Tumanski, «Induction coil sensors,» *Measurment Science And Technology,* vol. 18, pp. 31-46, 2007.

[16] H. Ueda et T. Watanabe, «Several problems about sensitivity and frequency response of an induction magnetometer,» *Sci. Rep. Tohoku Univ., Ser. 5. Geophysics,* vol. 22, pp. 107-127, 1975.

[17] T. Chady, M. Enokizono, T. Todaka, Y. Tsuchida and R. Sikora, "A family of matrix type sensors for detection of slight flaws in conducting plates on Magnetics," *IEEE Transactions,* vol. 35, no. 5, p. 3655–3657, 1999.

[18] V. Korepanov, R. Berkman, L. Rakhlin and al, "Advanced field magnetometers comparative study," *Measurement,* vol. 29, no. 2, pp. 137-146, 2001.

[19] G. Mook, O. Hesse et H. Uchann, «Deep Penetrating Eddy Currents and Probes,» *Conférence: European Conference for Non destructive Testing.,* 2006.

[20] J.-M. Decitre, «Optimization of Flexible Eddy Current Patterns with Low Sensitivity to Lift-Off,» *Electromagnetic Non-Destructive Evaluation, IOS Press,* vol. 42, pp. 275-282, 2017.

[21] M. Couty et al., «Fabrication and Packaging of Flexible Polymeric Microantennae for in Vivo Magnetic Resonance Imaging,» *Polymers,* vol. 4, pp. 656-673, 2012.

[22] M. Woytasik et al., «Characterization of flexible RF microcoils dedicated to local MRI,» *Microsyst Technol,* vol. 13, pp. 1575-1580, 2007.

[23] M. Khelifa et al., «Design and fabrication of rectangular NMR microcoil on flexible substrate,» *https://hal.archives-ouvertes.fr/hal-01280186,* 2016.

[24] O. Nielsen and al., "Development, construction and analysis of the 'Oersted' fluxgatemagnetometer," *Meas. Sci. Technol,* no. 6, pp. 1099-1115, 1995.

[25] C. Morón and al., "Magnetic Sensors Based on Amorphous Ferromagnetic Materials: A Review," *Sensors,* vol. 15, no. 11, pp. 28340-28366, 2015.

[26] P. Ripka and M. Janosek, "Advances in Magnetic Field Sensors," *IEEE SENSORS JOURNAL,* vol. 10, no. 6, pp. 1108-1116, 2010.

[27] P. Kejik and al., "A new compact 2D planar fluxgate sensor with amorphous metal core," *Sens. Actuators A Phys,* vol. 81, pp. 180-183, 2000.

[28] E. E. Heim, F. Ludwig and M. Schilling, "Binding assays with streptavidin-functionalized superparamagnetic nanoparticles and biotinylated analytes using fluxgate magnetorelaxometry," *J. Magn. Magn. Mater,* vol. 321, no. 10, pp. 1628-1631, 2009.

[29] S. Wöhl-Bruhn and al., "Fluxgate magnetorelaxometry: a new approach to study the release properties of hydrogel cylinders and microspheres,"

Inter. J. Pharma, vol. 436, no. 1-2, pp. 677-684, 2012.

[30] H. Joisten, B. Guilhamat, M. Audoin, J. Léger, R. Cuchet, G. Barrois, J. Albertini, P. Gaud, P. Renaux, D. Bloch et B. Viala, «Microfluxgate Performance Improvement inMicrotechnology,» *IEEE Trans.Mag*, vol. 41, p. 4356–4358, 2005.

[31] A. Msaed, «Micro capteur magnétique de mesure de courant et traitement intégré,» *Thèse de doctorat de l'Institut polytechnique de Grenoble préparée au laboratoire de Génie Electrique de Grenoble (G2Elab),* 2009.

[32] E. Harrison, D. Turney, H. Rowe and H. Gollop, "The Electrical Properties of High Permeability Wires Carrying Alternating Current," *Proc. R. Soc. Math. Phys. Eng. Sci.*, vol. 157, no. 891, pp. 451-479, 1936.

[33] L. Panina and K. Mohri, "Magneto-impedance effect in amorphous wires," *Appl. Phys. Lett.*, vol. 65, no. 9, pp. 1189-1191, 1994.

[34] F. Vacher, «Développement d'un imageur magnétique pour le contrôle non destructif par courants de Foucault,» Thèse de doctorat de l'école normale supérieure de cachan, 2007.

[35] C. Ravat, «Conception de multicapteurs à courants de Foucault et inversion des signaux associées pour le controle non destructif,» Thèse de doctorat de l'université paris-sud 11, 2008.

[36] M. Phan, H. Peng, S. Yu and al, "Optimized giant magnetoimpedance effect in amorphous and nanocrystalline materials," *Journal of Applied Physics,* vol. 99, no. 8, p. 08C505, 2006.

[37] *http://www.aichi-mi.com.*

[38] C. Tannous et J. Gieraltowski, «Giant Magneto-Impedance and its Applications,» *arXiv:physics/0208035,* Aug. 2002.

[39] A. Boukhenoufa, C. Dolabdjian and D. Robbes, "High-sensitivity giant magnetoinductive magnetometer characterization implemented with a low-frequency magneticnoise-reduction technique," *IEEE Sens. J.*, vol. 5, no. 5, pp. 916-923, 2005.

[40] P. Traore, «Introduction des techniques numériques pour les capteurs magnétiques GMI (Giant Magneto-Impedance) à haute sensibilité : mise en œuvre et performances,» Thèse de doctorat de l'Universite de grenoble, 2016.

[41] F. Vacher, F. Alves and C. Gilles-Pascaud, "Eddy current nondestructive testing with giant magneto-impedance sensor," *NDT & E International*, vol. 40, no. 6, pp. 439-442, 2007.

[42] T. Peng, J. Moulin, F. Alves et Y. Le bihan, «Conception et réalisation de micro-capteurs à magnéto-impédance pour le contrôle non destructif,» Thèse de doctorat de l'Université Paris- Sud, 2014.

[43] F. Alves and A. Bensalah, "New 1D-2D magnetic sensors for applied electromagnetic engineering," *Journal of Materials Processing Technology*, Vols. 1-3, no. 181, pp. 194-198, 2007.

[44] A. Asfour, M. Zidi et J. Yonnet, «High Frequency Amplitude Detector for GMI Magnetic Sensors,» *Sensors*, vol. 14, p. 24502–24522, 2014.

[45] L. Chen et al., «Chen, L.; Bao, C.C.A prototype of giant magnetoimpedance-based biosensing system for targeted detection of gastric cancer cells,» *Biosens. Bioelectron.*, vol. 58, pp. 338-344, 2014.

[46] P. LEROY et al., «Use of Magnetic Concentrators to Highly Improve the Sensitivity of Hall Effect Sensors,» *Sensor Letters*, vol. 5, p. 162–166, 2007.

[47] P. Leroy, C. Coillot, V. Mosser, A. Roux and G. Chanteur, "Use of Magnetic Concentrators to Highly Improve the Sensitivity of Hall effect Sensors," *Sensor Letters*, vol. 5, no. 1, pp. 162-166, 2007.

[48] P. Kejik and al., "An integrated micro-Hall probe for scanning magnetic microscopy,," *Sens. Act. A*, vol. 129, pp. 212-215, 2006.

[49] L. Ejsing, M. Hansen et A. Menon, «Magnetic microbead detection using the planar Hall effect,» *Magn.. Magn. Mater*, vol. 293, p. 677–684, 2005.

[50] A. Oota and al., "Non-Destructive Testing of Structural Materials Using a Scanning Hall-Sensor Microscope," *IEEJ Transactions on Fundamentals and Materials*, vol. 123, no. 7, pp. 611-617, 2003.

[51] J. Lee et al., «Nondestructive testing and crack evaluation of ferromagnetic material by using the linearly integrated hall sensor array,» *Mechanical Science and Technology*, vol. 22, pp. 2310-2317, 2008.

[52] W. Thomson, «On the Electro-Dynamic Qualities of Metals: Effects of Magnetization on the Electric Conductivity of Nickel and of Iron,» *Proc. R. Soc. Lond.*, vol. 8, p. 546–550, 1856.

[53] P. Ripka, "Electric current sensors: a review," *Meas. Sci. Technol.*, vol. 21, no. 11, p. 112001, 2010.

[54] H. Polovy - du Souich, «Capteurs mixtes supraconducteur-GMR pour des applications médicales,» Thèse de doctorat de l'Université Pierre et Marie Curie préparée au Service de Physique de l'Etat Condensé CEA, 2010.

[55] A. Manzin and al., "Modeling of Anisotropic Magnetoresistance Properties of Permalloy Nanostructures," *IEEE Transactions on Magnetics*, vol. 50, no. 4, 2014.

[56] *https://www.sensitec.com/products-solutions/angle-and-length-measurement/al700-sensor-family.*

[57] E. Zimmermann, E. Verweerd, W. Glaas et A. Tillmann, «An AMR sensor-based measurement system for magnetoelectrical resistivity tomography,» *IEEE Sensors J.*, vol. 5, p. 233–241, 2005.

[58] Z. Jiang et al., «An integrated microfluidic cell for detection, manipulation, and sorting of single micron-sized magnetic beads,» *Conférence: 50th Annual Conference on Magnetism and Magnetic Materials, Baltimore, MD,* 2006.

[59] K. Allweins, M. Kreutzbruck et G. Gierelt, «Defect detection in aluminum laser welds using an anisotropic magnetoresistive sensor array,» *Conférence: 49th Annual Conference on Magnetism and Magnetic Materials, San Jose, CA*, 2005.

[60] W. Cheng, "Pulsed eddy current testing of carbon steel pipes' wall-thinning through insulation and cladding. 2012," *J.Nondestruct. Eval.*, vol. 31, no. 3, pp. 215-224, 2012.

[61] A. Suksmono et al., «Magnetic imaging system in smartphones based on built-in magnetometer,» *IEEE International Magnetics Conference (INTERMAG), Dublin, Ireland,* 2017.

[62] V. Markevicius and al., "Vehicle Speed and Length Estimation Using Data from Two Anisotropic Magneto-Resistive (AMR) Sensors," *Sensors*, vol. 17, no. 8, 2017.

[63] «http://www.nobelprize.org/nobel_prizes/physics/laureates/2007/».

[64] M. Baibich, J. Broto, A. Fert, F. N. V. Dau, F. Petroff, P. Eitenne, G. Creuzet, A. Friederich et j. Chazelas, «Giant Magnetoresistance of (001)Fe/(001)Cr Magnetic Superlattices,» *Phys. Rev. Lett,* vol. 61, pp. 2472-2475, 1988.

[65] L. Chang, M. Wang, L. Liu, S. Luo et P. Xiao, «A brief introduction to giant magnetoresistance,» *arXiv.org > cond-mat > arXiv:1412.7691,* 2014.

[66] M. Pannetier-Lecoeur, «Superconducting-magnetoresistive sensor: Reaching the femtotesla at 77 K,» Thèse d'habilitation à Diriger des Recherches préparée Service de Physique de l'Etat Condensé – CEA Saclay, 2010.

[67] S. Hui-Min, H. Liang et F. Xin, «Integrated Giant Magnetoresistance Technology for Approachable Weak Biomagnetic Signal Detections,» *Sensors,* 2018.

[68] D. Venkatramana and al., "Giant Magnetoresistance-based Biosensor for Detection of Influenza A Virus," *Front Microbiol.,* vol. 7, no. 400, 2016.

[69] H. Shirzadfar and al., "Needle-type GMR Sensor to Estimate the Magnetic Properties of Diluted Ferrofluid for Biomedicine Application," *IRBM,* vol. 3, no. 36, pp. 178-184, 2016.

[70] T. Chen et al., «Integration of GMR-based pin torque oscillators and CMOS circuitry,» *Solid-State Electron,* vol. 111, pp. 91-99, 2015.

[71] Y. Li, B. Yan et al., «Gradient-field pulsed eddy current probes for imaging of hidden corrosion in conductive structures.,» *Sensors Actuators A Phys,* vol. 238, p. 251–265, 2016.

[72] B. Dieny et al., «Magnetotransport properties of magnetically soft spin-valve structures,» *J. Appl. Phys,* vol. 69, pp. 4774-4779, 1991.

[73] F. Hankard, J. Gattacceca, C. Fermon, M. Pannetier-Lecoeur, B. Langlais, Y. Quesnel, P. Rochette and S. A. McEnroe, "Magnetic field microscopy of rock samples using a giant magnetoresistance–based scanning magnetometer," *An Electronic Journal Of The Earth Sciences,* vol. 10, no. 10, 2009.

[74] M. Julliere, "Tunneling between ferromagnetic layers," *Physics Letters A,* vol. 54, no. 3, pp. 225-226, 1975.

[75] T. Miyazaki and N. Tezuka, "Giant magnetic tunneling fe/al2o3/fe junction," *Journal of Magnetism and Magnetic Materials,* vol. 139, no. 3, pp. 231-235, 1995.

[76] J. Moodera, L. Kinder, T. Wong and R. Meservey, "Large magnetoresistance at room temperature in ferromagnetic thin junctions," *Phys. Rev. Lett.,* vol. 74, no. 16, pp. 3273-3276, 1995.

[77] L. Yuan, J. Shen, G. Anderson et N. Christopher, «Method of fabricating a tunneling magnetoresistive (TMR) reader,» *Western Digital (Fremont) LLC* , 2012.

[78] S. Lee, Y. Takemura et J. Park, «Effect of double MgO tunneling barrier on thermal stability and TMR ratio for perpendicular MTJ spin-valve with tungsten layers,» *Appl. Phys. Lett.*, vol. 109, p. 182405, 2016.

[79] S.-E. Lee, J.-U. Baek, et J.-G. Park, «Highly Enhanced TMR Ratio and Δ for Double MgO-based p-MTJ Spin-Valves with Top Co2Fe6B2 Free Layer by Nanoscale-thick Iron Diffusion-barrier,» *Sci Rep.*, 2017.

[80] A. Silva, D. Leitao et al., «Linearization strategies for high sensitivity magnetoresistive sensors,» *Eur. Phys. J. Appl. Phys.*, vol. 72, 2015.

[81] J. Hayakawa, S. Ikeda, Y. Lee, F. Matsukura and H. Ohno, "Efect of high annealing temperature on giant tunnel magnetoresistance ratio of cofeb/mgo/cofeb magnetic tunnel junctions," *Applied Physics Letters*, vol. 89, no. 23, p. 232510, 2006.

[82] R. Janeiro and al., "Linearization and Field Detectivity in Magnetic Tunnel Junction Sensors Connected in Series Incorporating 16 nm-Thick NiFe Free Layers," *IEEE Transactions On Magnetics*, vol. 48, no. 11, pp. 4111-4114, 2012.

[83] M. Pelkner, R. Stegemann, N. Sonntag, R. Pohl et M. Kreutzbruck, «Benefits of GMR Sensors for High Spatial Resolution,» *AIP Conference Proceedings: American Institute of Physics*, vol. 1949, 2018.

[84] H. Lei and al., "Contactless Measurement of Magnetic Nanoparticles on Lateral Flow Strips Using Tunneling Magnetoresistance (TMR) Sensors in Differential Configuration," *Sensors*, vol. 16, no. 12, 2016.

[85] X. Li, J. Hu, W. Chen, L. Yin and X. Liu, "A Novel High-Precision Digital Tunneling Magnetic Resistance-Type Sensor for the Nanosatellites' Space Application," *micromachines*, vol. 9, no. 121, 2015.

[86] A. Jander et al., «Chopping techniques for low-frequency nanotesla spin-dependent tunneling field sensors,» *J. Appl. Phys.*, vol. 93, p. 8382–8384, 2003.

[87] C. Fermon et M. Pannetier-Lecoeur, «Electronique de spin et capteurs magnétiques,» *Reflets phys.*, vol. 18, pp. 8-11, 2010.

[88] A. Persson et al., «Low-frequency noise in planar Hall effect bridge sensors,» *Sensors and Actuators A: Physical*, vol. 171, pp. 212-218, 2011.

[89] C. Fermon et M. Van de Voorde, «Nanomagnetism: Apllications and Perspectives,» ISBN: 978-3-527-33985-3, Book, 2017.

[90] F. Förster, "Sensitive eddy-current testing of tubes for defects on the inner and outer surfaces," *Nondestruct. Testing*, no. 7, pp. 28-36, 1974.

[91] M. Morozov, G. Rubinacci, A. Tamburrino and S. Ventre, "Numerical models of volumetric insulating cracks in eddy-current testing with experimental validation," *IEEE Trans. Magn.*, no. 42, pp. 1568-1576, 2006.

[92] http://www.ndt.net/article/ecndt98/aero/043/043.htm.

[93] K. E. Rober, «Holographic non destructive testing,» *New York: Academic Press Inc*, 1974.

[94] *https://www.ndt.net/ndtaz/content.php?id=621*.

[95] Kohan et A. Lawrence, «Boiler operator's guide (4th ed.),» *McGraw-Hill Professional*, p. 240, 1997.

[96] ASTM, E2700, «Contact Ultrasonic Testing of Welds using Phased Arrays,» *Conshohocken, PA: American Society for Testing of Materials*, vol. 3, p. 1536–44, 2012.

[97] M. Silk, «Ultrasonic transducers for nondestructive testing,» *Adam Hilger Ltd., Accord, MA*, 1984.

[98] H. Banjak, «X-ray computed tomography reconstruction on non-standard trajectories for robotized inspection,» Thèse de doctorat de l'université de lyon préparée au CEA-LIST, 2016.

[99] S. Kolkoori, N. Wrobel, U. Zscherpel et U. Ewert, «A new X-ray backscatter imaging technique for non-destructive testing,» *NDT&E International,* vol. 70, pp. 41-52, 2015.

[100] J. Dumont-Fillon, «Contrôle non destructif (CND),» *Techniques de l'ingénieur,* 1996.

[101] L. Janousek, K. Capova, N. Yusa and K. Miya, "Multiprobe inspection for enhancing sizing ability in eddy current nondestructive testing," *IEEE Trans. Magn,* no. 44, p. 1618–1621, 2008.

[102] Z. Mottl, "The quantitative relations between true and standard depth of penetration for air-cored probe coils in eddy-current testing," *NDT International,* vol. 1, no. 23, pp. 11-18, 1990.

[103] J. PEREZ, «Electromagnétisme, Fondements et applications,» *Dunod, 740p,* 2018.

[104] B. Delabre, «Développement de capteurs flexibles à courants de Foucault : applications à la caractérisation des propriétés électromagnétiques des matériaux et à la détection de défauts par imagerie statique,» p. 16, 2016.

[105] M. Perdrix, «Contrôle non destructif par courants de Foucault,» *La théorie des courants de Foucault, CAST,* 1990.

[106] *http://www.imagic-project.eu/credit.html.*

[107] N. Sergeeva-Chollet et al., «Eddy Current Probes Based on Magnetoresistive Array Sensors as Receivers,» *19th World Conference on Non-Destructive Testing,* Munich, Germany, 2016.

[108] P. Chemin, "Enseignements pratiques tirésde l'utilisation rationnelle d'un pénétrantdiluable à l'eau," *Revue Pratique de Contrôle Industriel,*

no. 189, pp. 23-26, 1994.

[109] M. Oka and M. Enokizono, "Non-destructive testing on stainless steel plate by rotational magnetic flux sensor," *IEEE Transactions on Magnetics*, vol. 5, no. 33, pp. 3373-3375, 1997.

[110] D. Rugar and al., "Magnetic force microscopy: General principles and application to longitudinal recording media," *Appl. Phys.*, vol. 68, no. 3, p. 1169, 1990.

[111] A. M. Chang and al., "Scanning Hall probe microscopy," *Appl. Phys.Lett.*, vol. 61, no. 16, p. 1974, 1992.

[112] A. Oral, S. J. Bending, and M. Henini, "Real-time scanning Hall probe microscopy," *Appl. Phys. Lett*, vol. 69, no. 6, p. 1324, 1996.

[113] J. R. Kirtley and al., "High-resolution scanning SQUID microscope," *Appl. Phys. Lett.*, vol. 66, no. 9, p. 1138, 1994.

[114] J. N. Chapman, A. Johnston and L. Heyderman, "Coherent Foucault imaging: A method for imaging magnetic domain structures," *J. Appl. Phys*, vol. 76, no. 9, p. 5349, 1994.

[115] B. Argyle, B. Petek, D. Herman, and Jr., "Optical imaging of magnetic domains in motion (invited)," *J. Appl. Phys.*, vol. 61, no. 8, p. 4303, 1987.

[116] T. Takezaki and K. Sueoka, "Quantitative current measurements using scanning magnetoresistance microscopy," *Ultramicroscopy*, vol. 108, p. 970– 974, 2008.

[117] H. Hopster et H. Oepen (Eds.), «Magnetic Microscopy of Nanostructures,,» *Springer*, 2005.

[118] Y. Shibata, S. Nomura et al., «Imaging of current density distributions with a Nb weak-link scanning nano-SQUID microscope,» *Scientific Reports*, vol. 5, 2015.

[119] P. Reith, X.-J. Wang and H. Hilgenkamp, "Analysing Magnetism Using Scanning SQUID Microscopy," *Review of Scientific Instruments*, vol. 88, no. 12, 2017.

[120] A. Chang, "Sample-detector coupling in atomic resolution magnetic resonance diffraction," *Appl. Phys. Lett.*, vol. 61, no. 16, pp. 1974-1976, 1992.

[121] A. Guendouz, "Etude des propriétés structurales et magnétiques des couches ferromagnétiques par microscopie à champs proche et effet Kerr magnéto-optique," These préparée au LPCMME, 2011.

[122] F. Richheimer, M. Costa, and al., "3D Magnetic Field Reconstruction Methodology Based on a Scanning Magnetoresistive Probe," *Sensors*, vol. 18, no. 7, 2018.

[123] H. Lodish, A. Berk, S. Zipursky, P. Matsudaira, D. Baltimore et J. Darnell, «Microscopy and Cell Architecture,» *Molecular Cell Biology. 4th edition*, 2000.

[124] B. Alberts et al., «Looking at the Structure of Cells in the Microscope,» *Molecular Biology of the Cell. 4th edition. Garland Science*, 2002.

[125] D. Ngo et L. Kuhn, «In situ transmission electron microscopy for magnetic nanostructures,» *Adv. Nat. Sci: Nanosci. Nanotechnol.*, vol. 7, 2016.

[126] D.-T. Ngo and al., "Nanoscale physical microstructure and micromagnetic behaviour of CoIr film with negative anisotropy," *J. Phys. D: Appl. Phys*, vol. 44, no. 9, 2011.

[127] *http://www.phy.ohiou.edu/~asmith/p894w07/Lecture14.pdf.*

[128] R. Young, J. Ward et F. Scire, «Observation of Metal-Vacuum-Metal Tunneling, Field Emission, and the Transition Region,» *Physical Review Letters*, vol. 27, pp. 922-924, 1971.

[129] W. Hofer , A. Foster and A. Shluger, "Theories of scanning probe microscopes at the atomic scale," *REVIEWS OF MODERN PHYSICS,* vol. 75, no. 4, 2003.

[130] A. McQuarrie et J. Simon, «A Molecular Approach,» *Physical Chemistry*, 1997.

[131] I. Serre, «L'apport de l'étude des surfaces à la compréhension du comportement des matériaux à l'échelle macroscopique,» Mémoire présenté pour l'obtention de L'Habilitation à Diriger des Recherches De l'Université de Lille 1, 2010.

[132] G. Binnig, C. Quate and C. Gerber , "Atomic Force Microscope," *Physical Review Letters 56, 930 (1986).,* vol. 56, no. 930, 1986.

[133] *http://www.nanoscience.de/HTML/methods/afm.html.*

[134] A. Thiaville, J. Miltat and J. Garcia, "Magnetic Force Microscopy: Images of Nanostructures and Contrast Modeling," *Springer, NanoScience and Technology book series (NANO),* vol. 200, pp. 225-252.

[135] L. Abelmann, A. van den Bos and C. Lodder, "Magnetic Force Microscopy – Towards Higher," *Magnetic Microscopy of Nanostructures,* pp. 253-284, 2005.

[136] M. Kustov, «Caracterisation et conception de micro-aimants pour la levitation diamagnetique de micro- et nano-particules,» *https://tel.archives-ouvertes.fr/tel-00578044,* 2011.

[137] A. Dias and M. Andrade, "Atomic force and magnetic force microscopies applied to duplex stainless steels," *Applied Surface Science,* vol. 161, pp. 109-114, 2000.

[138] J. Zhang, S. Siddiqui et al., «360° domain walls: stability, magnetic field and electric current effects,» *New J. Phys.,* vol. 18, 2016.

[139] T. Takezaki and K. Sueoka, "Quantitative current measurements using scanning magnetoresistance microscopy," *Ultramicroscopy*, no. 108, p. 970– 974, 2008.

[140] Z. Li, X. Li, D. Dong, D. Liu, H. Saito and S. Ishio, "AC driven magnetic domain quantification with 5 nm resolution," *Sci Rep.*, vol. 4, 2014.

[141] J. Kirtley, "Fundamental studies of superconductors using scanning magnetic imaging," *Rep. Prog. Phys.*, vol. 73, no. 126501, 2010.

[142] D. Meyners, T. Von Hofe, M. Vieth, M. Ruhrig, S. Schmitt and E. Quandt, "Pressure Sensor Based on Magnetic Tunnel junctions," *Journal of Applied Physics,* no. 105, 2009.

[143] T. Meier, "Magnetoresistive and Thermoresistive Scanning Probe Microscopy with Applications in Micro and Nanotechnology," *Scientific Publishing*, 2014.

[144] T. Takezaki, D. Yagiswa and K. Sueoka, "Magnetic Field Measurement using Scanning Magnetoresistance Microscope with Spin-Valve Sensor," *IOP SCIENCE,* vol. 45, no. 3B, p. 2251–2254, 2014.

[145] M. Costa, J. Gaspar, R. Ferreira, E. Paz, H. Fonseca, M. Martins, S. Cardoso and P. Freistas, "Integration of Magnetoresistive Sensors With Atomic Force Microscopy Cantilevers for Scanning Magnetoresistance Microscopy Applications," *IEEE TRANSACTIONS ON MAGNETICS,* vol. 51, no. 11, 2015.

[146] C. Christides, S. Stavroyiannis, G. Kallias, A. Nassiopoulou and D. Niarchos, "Giant magnetoresistance Co/Cu multilayer sensors for use in magnetic field mapping," *Sensors and Actuators*, vol. 77, p. 167–171, 1999.

[147] D. Mitin, M. Grobis and M. Albrecht, "canning magnetoresistive microscopy: An advanced characterization tool for magnetic nanosystems," *Rev. Sci. Instrum.*, vol. 87, 2016.

[148] *http://www.senis.ch/products/mappers/high-end-all-in-one-magnetic-field-mapping-system-mms-1a-rs.*

[149] G. Balasubramanian et al., «Nanoscale imaging magnetometry with diamond spins under ambient conditions,» *Nature,* 2008.

[150] C. Degen, «Scanning magnetic field microscope with a diamond single-spin sensor,» *Appl. Phys. Lett.,* vol. 92, 2008.

[151] L. Rondin et al., «Stray-field imaging of magnetic vortices with a single diamond spin,» *Nature Commun,* vol. 4, 2013.

[152] lpa.ens, «Optique cohérente et non linéaire: Electrodynamique quantique avec les centres NV du diamant,» *http://www.lpa.ens.fr/spip.php?article1135.*

[153] M. Nur-E-Alam, M. Vasiliev, V. Kotov and K. Alameh, "Recent Developments in Magneto-optic Garnet-type Thin-film Materials Synthesis," *ScienceDirect,* vol. 76, pp. 61-73, 2014.

[154] M. Koblischkat et R. Wijngaarden, «Magneto-optical investigations of superconductors,» *Supercond. Sci. Technol.,* vol. 8, pp. 199-213, 1995.

[155] P. Kasiraj, R. Shelby, J. Best et D. Horne , «Magnetic domain imaging with a scanning Kerr effect microscope,» *IEEE Trans Magnetics,* vol. 22, pp. 837-839, 1986.

[156] R. Schafer, A. Hubert et G. Herzer, «Domain observation on nanocrystalline material,» *J Appl Phys,* vol. 69, p. 5325–5327, 1991.

[157] W. Clegg, N. Heyes, E. Hill et C. Wright, «Development of a scanning laser microscope for magneto-optic studies of thin magnetic films,» *J Magnet Magnet,* vol. 95, pp. 49-57, 1991.

[158] C. Jooss, J. Albrecht, H. Kuhn, S. Leonhardt et Kronmueller, «Magneto-optical studies of current distributions in high-Tc superconductors,» *Rep. Prog. Phys.,* vol. 65, pp. 651-788, 2002.

[159] A. Polyanskii, X. Cai, D. Feldmann et D. Larbalestier, «Vizualisation of magnetic flux in magnetic material and high temperature superconductors using farady effect in ferrimagnetic garnet films,» *Kluwer Academic Publishers: Netherlands,* pp. 353-370.

[160] M. Nur-E-Alam, M. Vasiliev, K. Alameh et C. Valli, «Magneto-optical visualisation for high-resolution forensic data recovery using advanced thin film nano-materials,» *International Cyber Resilience conference,* 2010.

[161] C. Jooss, K. Guth, V. Born et J. Albrecht, «Electric field distribution at low-angle grain boundaries in high-temperature superconductors,» *Phys. Rev. B,* vol. 65, 2001.

[162] T. Schuster, M. Koblishka, B. Ludescher et N. Moser, «EuSe as magneto-optical active coating for use with the high resolution faraday effect,» *Cryogenics,* vol. 31, pp. 811-816, 1991.

[163] S. Salapaka and M. Salapaka, "Scanning Probe Microscopy," *IEEE Control Systems Magazine,* vol. 2, no. 28, p. 65–83, 2008.

[164] L. Knauss, S. Woods et A. Orozco, «Current Imaging using Magnetic Field Sensors,» *Desk Reference,* 2004.

[165] G. Kletetschka et T. Adachi, «Magnetic detection of large magnetic fields that occurred during the Vredefort impact, implications for Mars magnetic anomalies,» *Large Meteorite Impacts and Planetary Evolution IV, Lunar and Planet. Inst., Vredefort Dome, South Africa,* 2008.

[166] J. Bourgeat, C. Entringer, P. Galy, P. Fonteneau et M. Bafleur, «Local ESD protection structure based on Silicon Controlled Rectifier achieving very low overshoot voltage,» *EOS/ESD Symposium,* 2009.

[167] J. Nogués et K. Schuller, «Exchange bias,» *Journal of Magnetism and Magnetic Materials,* vol. 192, pp. 203-232, 1999.

[168] S. Parkin and D. Mauri, "Spin engineering: Direct determination of the

Ruderman-Kittel-Kasuya-Yosida far-field range function in ruthenium," *Physical Review B,* vol. 13, no. 44, 1991.

[169] Y. Yafet, "Ruderman-Kittel-Kasuya-Yosida range function of a one-dimensional free-electron gas," *Physical Review B,* vol. 7, no. 36, 1987.

[170] J. J. P. Wikswo, «The Magnetic Inverse Problem for NDE,» *Sensors: Fundamentals, Fabrication, and Applications,* pp. 629-695, 1996.

[171] S. Chatraphorn, E. Fleet, F. Wellstood, L. Knauss and T. Eiles, "Scanning SQUID Microscopy of Integrated Circuits," *Applied Physics Letters*, vol. 76, no. 16, pp. 2304-2306, 2000.

[172] *https://blog.fraudfighter.com/bid/54746/Detecting-Counterfeit-Money-Magnetic-Ink-Watermark-Lamps.*

[173] G. Kletetschka et T. Adachi, «Magnetic detection of large magnetic fields that occurred during the Vredefort impactimplications for Mars magnetic anomalies,» *Large Meteorite Impacts and Planetary Evolution IV, Lunar and Planet. Inst,* 2008.

[174] *http://www-civa.cea.fr.*

[175] D. Caetano et al., «A CMOS ASIC for Precise Reading of a Magnetoresistive Sensor Array for NDT,» *11th European Conference on Non-Destructive Testing (ECNDT 2014),* Prague, Czech republic, 2014.

université PARIS-SACLAY | ÉCOLE DOCTORALE Physique en Île-de-France (EDPIF)

Titre : Sonde 3D à base des capteurs magnétoresistives pour l'imagerie magnétique et le contrôle non-destructive.

Mots clés : Imagerie magnétique, Capteur magnétorésistif géante (GMR), Microscopie magnétique à balayage, Détection des trois composantes des champs, Contrôle non-destructif

Résumé : La thèse est dédiée au développement des sondes à base de capteurs magnétorésistifs capable de détecter les trois composantes du champ simultanément pour le contrôle non destructif par courants de Foucault et pour l'imagerie magnétique. Une première partie donne un aperçu de l'état de l'art des capteurs et des méthodes d'imagerie et du contrôle. Dans une seconde partie, la réalisation des sondes trois axes est donnée. Cela a inclus la micro fabrication, la réalisation de l'électronique de lecture, la conception et la réalisation de la partie mécanique et d'émission. Pour cela un travail important de simulation a été nécessaire. L'application de ces sondes sur des cas modèle pour l'imagerie magnétique avec une résolution submillimétrique est ensuite décrite. La sonde proposée dans cette thèse a été aussi utilisée avec succès pour détecter des défauts dans des échantillons d'aluminium et de titane avec un bon rapport signal sur bruit.

Title : 3D Probes based on magnetoresistive Sensors for magnetic micro-imaging and NDT

Keywords : Magnetic imaging, spin valve Giant magnetoresistive sensor (GMR), scanning magnetoresistance microscopy, 3D magnetic field, Non-destructive testing

Abstract : The thesis is dedicated to the development of probes based on magnetoresistive sensors capable of detecting the three components of the field simultaneously for eddy current non-destructive testing and for magnetic imaging. A first part provides an overview of the state of the art of sensors, imaging and control methods. In a second part, the realization of the three-axis probes is given. This included the micro-fabrication, the realization of the reading electronics, the design and realization of the mechanical part and emission. For this, an important simulation work was necessary. The application of these probes to model cases for magnetic imaging with submillimeter resolution is then described. The probe proposed in this thesis has also been used successfully to detect defects in aluminum and titanium samples with a good signal-to-noise ratio.

Université Paris-Saclay
Espace Technologique / Immeuble Discovery
Route de l'Orme aux Merisiers RD 128 / 91190 Saint-Aubin, France